Fractional Order Control of Active Magnetic Bearing Systems

A Dissertation

Presented to

the Faculty of the School of Engineering and Applied Science

University of Virginia

In Partial Fulfillment

of the requirements for the Degree of

Doctor of Philosophy

(Electrical and Computer Engineering)

by

Parinya Anantachaisilp

May 2015

Approval Sheet

This Dissertation is submitted in partial fulfillment of the requirements for the degree

of

Doctor of Philosophy

(Electrical and Computer Engineering)

Parinya Anantachaisilp

This Dissertation has been read and approved by the Examining Committee:

Zongli Lin, Advisor

Gang Tao, Committee Chair

Roger Fittro

Haibo Dong

Se Young Yoon

Accepted for the School of Engineering and Applied Science:

James Aylor, Dean, School of Engineering and Applied Science

May 2015

Abstract

Active magnetic bearings (AMBs) employ electromagnets to support machine components without mechanical contact. The magnetic forces are adjusted by feedback controllers to suspend the machine components within the magnetic field and to control the system dynamics during machine operation. Magnetic bearings offer many advantages for various applications. High-speed machines can operate smoothly because there is no friction during rotation. The maintenance cost and mechanical wear are low due to non-contact operation. A real time control in the AMB system helps to keep the rotor close to the center and to reduce vibrations during operation.

However, controller design for AMB systems is a challenging task because of the nonlinear nature of the plant dynamics, the very small natural damping in the process, the strict positioning specifications often required by the application, and the unstable open loop system dynamics. In most cases, a Proportional-Integral-Derivative (PID) controller is the chosen controller due to its simplicity and intuitiveness in the tuning of the controller parameters. However, sometimes a conventional PID controller cannot fulfill the industry performance standards for AMB systems, such as those specified by the American Petroleum Institute (API) and the International Organization for Standardization (ISO). In these cases, more complex controllers, such as LQG, H_∞, and μ-synthesis, are used to meet the desired specifications. The tradeoff between the simplicity of the controller structure and the achievement of good performance is a relationship that control engineers seek to balance and optimize.

Recently, fractional order calculus theory, which is the generalized version of integer order calculus, has been adopted for many applications due to its accuracy for modeling the dynamics of systems and its simplicity in model structure to represent high order processes. Fractional order control is one of the fields that many researchers and engineers are interested in because the response of a system with a fractional order controller is not restricted to a sum of exponential functions, and, as a result, a wide range of responses neglected by integer order calculus could be approached. One of the most popular fractional order controllers is the generalized PID controller, which is also called a fractional order PID (FOPID) controller. FOPID has two extra parameters, the non-integer order of integral and derivative terms, in comparison with the integer order PID controller. FOPID control can improve performance and robustness compared to conventional PID control in many applications while keeping the control structure simple. This suggests that an FOPID controller has good potential to reduce the gap between the simplicity of the controller structure and high closed-loop performance aspects as mentioned above.

In this dissertation, a fractional order PID control for AMB systems is proposed. The feasibility of FOPID for AMB systems is investigated in two aspects. The first aspect is the control of rotor suspension by magnetic bearings both in radial and axial directions. The second aspect is the surge control in a centrifugal compressor which uses the thrust AMB to modulate the impeller tip clearance for surge stabilization. Tuning methods are developed based on the evolutionary algorithms for searching the optimal values of the controller parameters. The resulting FOPID controllers are then tested and compared with an integer order PID controller, as well as with advanced controllers such as LQG and H_∞ controllers. The comparison is based on various stability performance and robustness specifications, as well as the controller dimension as implemented. Lastly, to validate the proposed method, experimental testing is carried out on a single-stage centrifugal compressor test rig equipped with magnetic bearings.

To my beloved family

Acknowledgments

This long journey in the doctoral study at the University of Virginia would not have been possible without the support of many individuals.

First of all, the author would like to thank all of his committee members. The author wishes to express his gratitude to his advisor, Professor Zongli Lin, who was abundantly helpful and offered invaluable assistance and support throughout the graduate program. His guidance in the academic career was very useful. Deepest gratitude is also due to Professor Pablo Yoon, who offered not only the theoretical and experimental knowledge in control but also his experiences in many different things. The appreciations also go to Professor Roger Fittro for sharing his expertise in magnetic bearing as well as his valuable experiences from industry. Many thanks go to Professor Gang Tao for his assistance in control theory as well as the valuable comments during the proposal, and Professor Haibo Dong who was always trying to find time for discussions and meetings during his busy schedule.

The author would like to use this opportunity to thank the Rotating Machinery and Control Laboratory (ROMAC) community for a warm and fun environment to work. The author wishes to express his appreciation to Long (Dee) Di for his friendship and for sharing his views on literature and knowledge in controls. The author would like to thank Dr. Zackary Whitlow for introducing many cool technologies and the fun run on weekends. Many thanks go to Dr. Wei Jiang for his endless help in fixing stuff for the experiment as well as the wide variety of knowledge. Special thank also owed to Dr. Simon Mushi for his incredible expertise in control and electronics during the early stage of graduate program, and thanks to Lori Pedersen for every event arrangement, and all the paper work that makes things flow smoothly.

Special thanks also go to two of his all time UVa best friends Nattawut Anuniwat and Kiadtisak Saenboonruang who have always been there. Without the two of you, this journey would not be this fun and meaningful. Thanks is also owed to Chris Brown who never refused to read my work as well as to give me meaningful feedback.

Finally, but most importantly, the author wishes to express his love and gratitude to his family for their understanding and endless love through the duration of his studies. Finally, words cannot express his appreciation owed to his fiancé, Sandra Khananusit, for her encouragement, assistance, and of course love. “Thanks for waiting this long.”

Contents

List of Tables

List of Figures

Nomenclature

Acronyms

AMB	Active Magnetic Bearing
API	American Petroleum Institute
CRONE	Commande Robuste dOrdre Non Entier
DE	Differential Evolution
FOPID	Fractional Order Proportional-Integral-Derivative
GA	Genetic Algorithm
IOPID	Integer Order Proportional-Integral-Derivative
ISO	International Organization of Standardization
LQG	Linear Quadratic Gaussian
LQR	Linear Quadratic Regulator
MIMO	Multiple-Input Multiple-Output
MS	Motor Side
PID	Proportional-Integral-Derivative
PSO	Particle Swarm Optimization

RL Riemann-Liouville

TID Tilt-Integral-Derivative

Symbols

$\delta_{\mathrm{cl,ref}}$ Impeller tip clearance reference

δ_{cl} Impeller tip clearance

$\hat{\Phi}_{\mathrm{c}}$ Estimated mass flow rate in the compressor

$\hat{\Psi}_{\mathrm{c,ss}}$ Steady-state pressure rise in the compressor

λ Order of integral term

μ Order of derivative term

ω_{H} Helmholtz frequency

ω_{n} Center frequency of the notch filter

Φ_{c} Mass flow rate in the compressor

Φ_{p} Mass flow rate in the plenum

Φ_{th} Mass flow rate in the throttle valve

Ψ_{c} Pressure rise in the compressor

Ψ_{p} Pressure rise in the plenum

Ψ_{th} Pressure in the throttle valve

ρ_{o1} Inlet gas density

ξ State of compression system

ζ Notch filter sharpness factor

A_{c}	Compressor duct cross-sectional area
B	Greitzer stability parameter
C_{min}	Minimum clearance relative to the center of auxiliary bearing
c_{th}	Throttle valve constant
f_{eff}	Effective magnetic force
I_{b}	Bias current
K_{D}	Derivative gain
K_{I}	Integral gain
K_{i}	Open loop current-to-force gain
K_{P}	Proportional gain
K_{x}	Open loop stiffness of the AMB
L_{c}	Compressor duct length
M_S	Sensitivity function magnitude peak
M_T	Complimentary sensitivity function magnitude peak
p_{o1}	Inlet pressure
R^0	Static value of effective reluctance
U	Impeller tip speed
u_{th}	Throttle valve opening percentage
V_{p}	Plenum volume

Chapter 1

Introduction

1.1 Scope of the dissertation

This dissertation demonstrates the design, analysis, and implementation of a fractional order PID controller (FOPID) for suppressing vibration and surge in a centrifugal compressor by active magnetic bearings (AMBs). This is the first time that an FOPID controller has been designed for and implemented on an AMB system. Furthermore, a comparison of the performance and efficiency of the FOPID, integer order PID (IOPID), and advanced controller based on simulation and experimental results is discussed.

1.2 Problem statement

PID is the most widely used type of controllers in industrial applications (more than 90 percent [7]). A PID control takes the form of

$$C_{\mathrm{PID}}(s) = K_{\mathrm{P}} + \frac{K_{\mathrm{I}}}{s} + K_{\mathrm{D}}s. \tag{1.1}$$

This high adoption rate of PID controller for industrial application is likely due to their components having an intuitive physical meaning, i.e., damping and stiffness, which makes them easy to tune. However, the desired performance of a system is sometimes not satisfied by using PID controllers, especially in a complex system such as AMBs. Thus, advanced controllers, which are typically of higher orders, are used instead. However, the design process for advanced controllers is quite complicated and it requires substantial experience to achieve good performance.

The challenge, then, is how to maintain the simplicity of the design process and of the structure of a controller (similar to that of a PID controller), while at the same time achieving performance at a level similar to advanced controllers.

One approach is to maintain the structure of the PID controller as shown in Eq. (1.1) and let the order of the integral and derivative terms be any non-integer number ($1/s \to 1/s^{\lambda}$ and $s \to s^{\mu}$, where λ and μ can be any non-integer numbers), so that the physical meaning of the controller remains the same but the parameter search range is extended [22]. To visualize the benefits of fractional order calculus, the analogy in Figure 1.1 illustrates the flexibility of the fractional order over the integer order in a similar way that the adjustable wrench can fit to more objects than the fixed size wrenches.

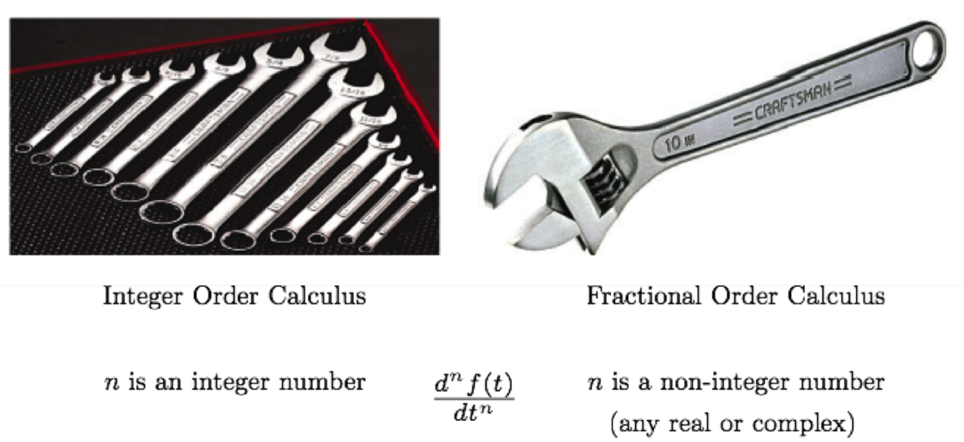

Figure 1.1: Analogy of integer and fractional order calculus

With the aforementioned benefits of fractional order control, this study applies the fractional order control concept to an AMB system. There are two previous studies in [19] and [42] on the related topic, but the experimental results of the proposed designs are not available, and the designs have not been validated in industrial applications. To advance beyond these works, this study will include the implementation of the fractional order control on the centrifugal compressor test rig equipped with AMBs at the Rotating Machinery and Control Laboratory (ROMAC), the University of Virginia.

1.3 Research objectives

The objective of this research is to develop a fractional order PID controller that achieves satisfactory performance of AMB systems. By considering two additional parameters, the fractional order derivative and integral terms, there is a high possibility that the desired specifications of the AMB control system can be satisfied. The proposed controller design method will be applied to a single-stage centrifugal compressor test rig equipped with AMBs. On this test rig, two advanced control methods, H_∞ and LQG, were previously studied by Sanadgol and Yoon in [61] and [73], respectively.

Here, the FOPID control method for AMB systems will be investigated in two aspects. The first aspect is the control of rotor suspension by magnetic bearings both in the radial and the axial directions. The second aspect is the control of surge, by using the thrust AMB to modulate the impeller tip clearance.

For both aspects, the FOPID tuning method will be developed based on the evolutionary algorithms for searching the optimal values of the controller parameters. Then, to verify the improvement over the conventional PID control, the resulting FOPID controllers will be tested and compared to integer order PID controllers that use the same tuning method as in the FOPID control design. Moreover, the results will be compared to the advanced controllers reported in [73] in terms of performance and robustness specifications, and the controller dimensions as implemented.

1.4 Research contributions

The contributions of this study can be summarized as follows:

1. The application of fractional order control for AMB systems is largely unexplored. This study can be used as a reference and a benchmark for the design and implementation of fractional order control for AMB systems.

2. This study also includes rotor dynamics in the fractional order control design which has not been done before. The design takes into account the unbalanced forces at different rotational speeds that cause vibration in the system.

3. This study is the first to use a fractional order controller for surge control in a centrifugal compressor.

4. The validation of the proposed fractional order control design method for both rotor suspension/rotation and surge control is demonstrated by conducting experiments on the industrial size single-stage centrifugal compressor at the ROMAC Laboratory, University of Virginia.

5. The efficiency of different tuning methods for FOPID controller design for AMB systems is studied and compared.

6. This study demonstrates that FOPID control has better performance and robustness than conventional PID control for AMB systems. FOPID control achieves performance and robustness similar to advanced control such as LQG and H_∞ control, but its structure and design process are simpler and it results in a lower controller dimension compared to advanced control.

1.5 Dissertation outline

The remainder of this dissertation is organized as follows:

- Chapter 2 provides a background on the principle of AMBs and their applications, with a focus on compressor applications. The control methods that have been implemented on AMB systems are reviewed.

- Chapter 3 explains the fundamentals and theory of fractional calculus. Definitions, characteristics, and tuning methods of FOPID control are overviewed. The approximation and discretization of FOPID controllers for implementation purposes is also described.

- Chapter 4 illustrates the AMB supported single-stage compressor test rig used in this study. In addition, the models of rotor dynamics in radial and axial directions as well as the compression system are derived.

- Chapter 5 explains the design process of the FOPID controller for rotor suspension. This includes selection of control objectives, tuning methods, and approximation for implementation. The simulation results of the designed FOPID controller are discussed in comparison with the IOPID and advanced controllers. Lastly, the predicted effectiveness of the designed controllers from the simulation is validated by experimental results.

- Chapter 6 describes the design process of the FOPID controller for surge control in the centrifugal compressor supported by AMBs. Again, the control objectives, tuning methods, and approximation are presented. The simulation results of the designed FOPID controller are discussed in comparison with the IOPID and advanced controllers. The chapter concludes with validation of the design by experimental results.

- Chapter 7 summarizes the work completed during this study and proposes possible future work.

Chapter 2

Background and Literature Review

2.1 Overview of active magnetic bearing systems

The use of magnetic forces to overcome the forces exerted on a moving mechanical body is the fundamental idea behind how magnetic bearings work. There are several benefits of magnetic bearings over conventional bearings, such as low losses due to non-contact operation and active control capability which can enhance the stability of the system. Furthermore, as a result of low mechanical wear and losses, system maintenance costs are significantly lower. Commercial applications that employ magnetic bearings include compressors, centrifuges, high-speed turbines, energy-storage flywheels, and high-precision machine tools. Magnetic bearings can be either passive or active. *Passive Magnetic Bearings* use repulsive forces from the interaction of two similar poles of two permanent magnets to keep the rotor away from the surfaces of bearings. *Active Magnetic Bearings* (AMB) use actively controlled electromagnetic forces to control the motion of a rotor or another ferromagnetic body in the air. An AMB system normally consists of sensors, electromagnets, power amplifiers, power supplies, and controllers [38]. Figure 2.1 shows the basic principle of an AMB system in one degree of freedom. The position sensor detects how far away the rotor is from the

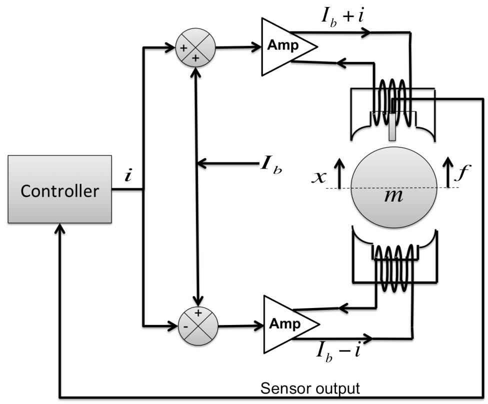

Figure 2.1: AMB system in one degree of freedom

magnet. This information is sent to the controller to output the proper voltage to the power amplifiers, which in turn apply currents to the electromagnets. The electromagnets then generate magnetic force to pull the rotor to the desired position (i.e., the center of the clearance space). Magnetic bearings for the radial directions are called *Radial Bearings* and those in the axial direction are called *Thrust Bearings*. A complete assembly of AMB components is illustrated in Figure 2.2.

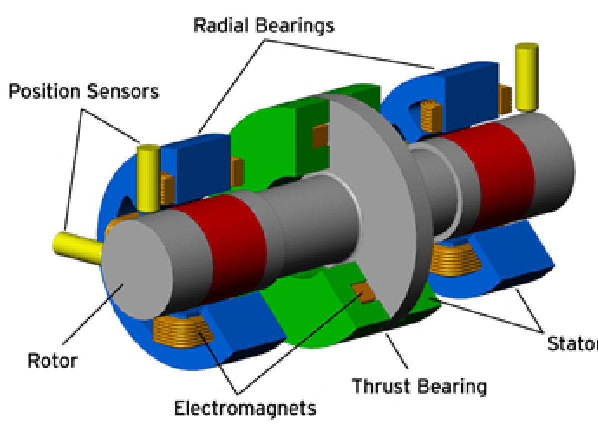

Figure 2.2: Assembly of an AMB system

2.2 Active magnetic bearings in compressors

Active magnetic bearings have increasingly been used in compressor applications because they provide higher performance and reliability. An example of a compressor equipped with magnetic bearings is shown in Figure 2.3. So far, AMBs have been applied to compressor applications mainly to improve performance of the system, using two approaches. The first approach is to use AMBs to support the rotor instead of the traditional bearings. This technology has been applied to compressors in industrial applications for more than a decade [43]. The second approach, which is in the research stage but shows the effectiveness of AMB usage in compressors, is to control the instability in the compression system, referred to as *surge* phenomenon.

Figure 2.3: A compressor equipped with magnetic bearings [1]

2.2.1 Rotor suspension

The rotor of the compressor is levitated by magnetic forces and is allowed to rotate with no mechanical contact and friction losses. Consequently, the maintenance cost is low because there are almost no consumable components and no lubrication is required. Moreover, AMBs have an active control capability which keeps the rotor near the clearance center during operation. This capability of AMBs helps compressors to operate efficiently at high rotational speeds.

2.2.2 Compressor surge control

The performance of a compressor is affected not only by the rotor suspension mechanism, but also the stability of the compression system. The information of compressor characteristics and efficiency is elucidated in the compressor characteristic curve as shown in Figure 2.4. This map provides all possible operating points of a compressor

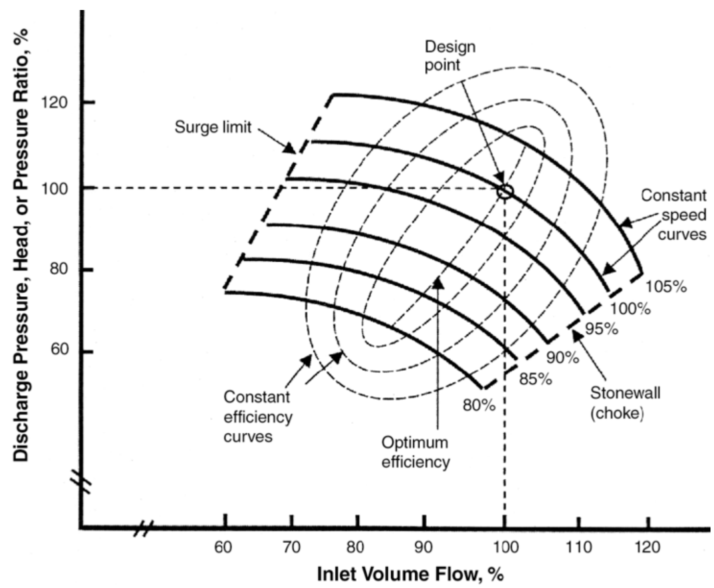

Figure 2.4: Compressor characteristic curve [2]

in terms of mass flow rate, pressure ratio, and rotational speed. Moreover, it also indicates the border between stable and unstable regions of compressor operation, referred to as the surge line. When the flow is reduced below the surge limit, the pressure at the discharge of the compressor exceeds the pressure generation capability of the compressor, causing a momentary reversal of flow. When this flow reversal occurs, the pressure of the discharge system is reduced, allowing the compressor to resume delivering flow until the discharge pressure again increases, and this surge cycle repeats. Surging usually creates a clearly audible noise. Prolonged operation in this unstable mode can cause serious mechanical damage to the compressor as illustrated in Figures 2.5 and 2.6 . When operating in a surge condition, the compressor discharge temperature increases significantly and the compressor experiences erratic and severe vibration levels that can cause mechanical damage to compressor components [2].

Figure 2.5: Compressor damage caused by surge [61]

Figure 2.6: Impeller damage caused by surge in a compressor [25]

There are two main techniques used to address the surge phenomenon. The first technique is surge avoidance, which is the prevention of operation at or near the surge limit. The surge avoidance line is placed in parallel to and on the right hand side of the surge limit line. The separation between the surge limit line and the surge avoidance line is called surge margin. This margin varies between 10% and 25%, depending on how critical operation safety is. Whenever the compressor's flow reduces and reaches the surge avoidance line, an anti-surge mechanism will try to increase the flow and bring the operating point of the compressor back to the right hand side of the surge avoidance line. The anti-surge mechanisms commonly used are blow-off valves and bleed valves. When these valves are opened, the pressure buildup in the compressor is released and the mass flow rate increases. The surge avoidance technique is easy and practical to implement, but this avoidance prevents the compressor from operating in the high-pressure region, which limits the performance of the compressor. More details on the surge avoidance technique can be found in [48].

The second technique is surge suppression and control. The objective of this technique is to increase the efficiency of compressors by allowing for operation closer to and beyond the surge limit line and to increase the range of mass flow where a compressor can operate stably. This technique can be achieved in both passive and active ways. The most common approach for a passive method is to vary the plenum volume by a spring-mass-damper system. This mechanism will induce a pressure variation in the compression system in order to extend the stable flow region. An example of a passive surge controller can be found in [6]. On the other hand, active surge controllers use actuators along with feedback flow and pressure measurements by sensors. One of the challenges of the active surge control method is choosing the proper actuator. The most widely used actuator for active surge control is a throttle valve at the system exhaust. In [12], a throttle valve was used as an actuator to stabilize the flow in the compressor with the measurement of the plenum pressure.

The results from the study show that a throttle valve stabilizes the system effectively in the low speed range, but the performance is degraded in the high speed range due to the bandwidth and mechanical limitations of the actuator.

Recently, AMBs have been demonstrated as a servo actuator for surge control. The motivation to use AMBs came from a study by Senoo and Ishida in [64], which shows that the clearance between an impeller tip and a shroud has a strong impact on the flow characteristics of a compressor. The use of AMBs to control the impeller tip clearance in a high speed centrifugal compressor was proposed by Sanadgol in [61]. The variation of the impeller tip clearance induces a pressure variation that is used to control the surge. The work by Sanadgol was limited to simulation study. Later, Yoon et al. [73] further developed and successfully implemented the method proposed by Sanadgol and the results showed that the surge controller can stabilize the compression system with the compressor running at up to 16,000 rpm.

2.3 Control of an AMB system

An AMB system is inherently open loop unstable. Therefore it is required to have a controller in the feedback loop to stabilize the system during the operation. Normally, the controller design for an AMB system starts with the PID controller because of its simplicity in structure. Recall here for an easy reference that the transfer function of a PID controller is given as

$$C_{\mathrm{PID}}(s) = K_{\mathrm{P}} + \frac{K_{\mathrm{I}}}{s} + K_{\mathrm{D}}s. \tag{2.1}$$

The controller parameters can be tuned intuitively, where the proportional gain K_{P} has a similar effect as adding stiffness, and the derivative gain K_{D} acts as the added damping to the system. In addition, the integral gain K_{I} helps in reducing the rotor position offset due to a static disturbance. Note that the form of a PID controller in

Eq. 2.1 is not a proper form for implementation. It is required additional term such as a lowpass filter. There are two popular methods in applying PID controller to an AMB system. The first method is called decentralized PID where an actuator pair of each control axis works independently from other pairs. The advantage of using the decentralized method is the simplicity in tuning the controller parameters for one control axis at a time. However, the lateral dynamics of the rotor at different bearing locations are coupled together. Thus, there may be some limitation in achieving the desired performance by using a decentralized method. The second method is called centralized or tilt-and-translate method. This method decouples the two rigid body modes, the tilt mode and the translate mode, and uses two separate PID controllers to stabilize each mode independently. More detail on the tilt-and-translate method can be found in [63]. Nevertheless, these two types of PID controllers have limitations when dealing with non-collocation of sensors and the flexible modes of the rotor. As such, additional filters are required in order to stabilize the closed-loop system.

Given the shortcomings of the PID controller mentioned above, some advanced controllers have been developed to stabilize an AMB system for better performance. These controllers are multiple-input multiple-output (MIMO) and centralized. Examples of advanced controllers used in AMB systems are Linear Quadratic Regulator (LQR), H_∞, and μ-synthesis controllers. The objective of the LQR controller design is to find the optimal state feedback gain K that minimizes the quadratic objective function J which represents a tradeoff between the energy of the states x and that of the control input u,

$$J = \int_0^\infty (x^T Q x + u^T R u) dt, \quad u = Kx. \tag{2.2}$$

For implementation, the LQR controller is extended to a Linear Quadratic Gaussian (LQG), where the Kalman filter is adopted as a state observer. An example of LQG control design for AMB systems can be found in [34]. The complication of this type of controllers is that it requires skill and experience to select the appropriate weighting matrices Q and R to obtain a controller that provides good performance. Therefore, because of practical applicability as mentioned in [63], LQR and LQG controllers are not widely used for AMB systems.

One of the most popular modern control methods for AMB systems is H_∞ control. It provides a powerful frequency domain framework for capturing design requirements such as control energy, reference tracking, bandwidth, disturbance rejection, and robust stability. Weighting functions are specified as an upper or lower bound (unstructured) of the uncertainties for each requirement, and the objective of H_∞ control is to find the controller that minimizes the infinity norm of the closed-loop system that takes into account all the weighting functions. An example of H_∞ control design for AMB systems can be found in [41].

Another popular modern control method for AMB systems is μ-synthesis. The μ-synthesis design takes an approach that is very similar to H_∞ control design but includes structured (parametric) model uncertainties instead of unstructured uncertainties. Parametric uncertainties in AMB systems include rotor speed, rotor mode damping, sensor and amplifier model, and AMB gains [41]. This allows the controller design to deal with uncertainties at the component level. The objective of μ-synthesis is to find the controller that maximizes the smallest uncertainty that causes instability. This implies that a μ controller will improve the performance of the closed-loop system even more than an H_∞ controller, but at the cost of a more complex uncertainty characterization. An example of μ controller design and derivation of each component uncertainty for AMB systems can be found in [30].

These advanced controllers result in better performance and stronger robustness to AMB systems compared to a PID controller, but the design process is more complicated and typically results in a higher order controller. For these reasons, they are still rarely used in industrial applications. Clearly, there is a tradeoff between simplicity when using a PID controller and high performance when using more advanced controllers, which require more complicated controller structure and design processes. Thus, there is motivation to investigate another control method that achieves this tradeoff.

Recently, fractional order calculus theory, which is the generalized version of integer order calculus, has been adopted for many applications due to its accuracy in modeling the dynamics of systems and its simplicity in model structure to represent high order processes. This approach shows a strong potential to satisfy the need of a more powerful controller with a simple structure.

Chapter 3

Fractional Order Calculus and Control

In this chapter, the background relevant to the fractional order PID control design and implementation is discussed. First, a brief history and definition of fractional order calculus is introduced. After that the fractional order system, model representation, and stability analysis is described. Then the definition, characteristics, and advantages of FOPID control are explained. Moreover, the existing tuning methods for FOPID controllers are reviewed. Lastly, the approximation method for the FOPID controller is described.

3.1 Fractional order calculus

Even though fractional calculus does not sound familiar to many people, this concept was developed about 300 years ago, around the same time when integer order calculus was invented. It began with a letter of Leibniz, a German mathematician, to L'Hôpital, a French mathematician, in 1965 with his curiosity posing the question "Can the meaning of derivatives with integer order be generalized to derivatives with non-integer orders?" L'Hôpital replied with another question "What if the order will be 1/2?"

Leibniz simply answered that "It will lead to a paradox, from which one day useful consequences will be drawn" [51]. From those conversations, several mathematicians have attempted to find an answer and make use of the concept in many different fields.

Before introducing the definition of fractional calculus, it is important to note that the term "fractional order" is not properly used. The suitable word should be "non-integer order" because the order can be irrational number as well. However, the "fractional order" term has been widely used in the literature until nowadays.

3.1.1 Definition

Fractional calculus is a generalization of integer order differentiation and integration to non-integer orders. To visualize the meaning of fractional calculus, let us consider the infinite sequence of n-fold integration and n-fold differentiation,

$$\int_a^t, .. \int_a^{\tau_n} f(\tau_1) d\tau_1 .. d\tau_n, ..., \int_a^t \int_a^{\tau_2} f(\tau_1) d\tau_1 d\tau_2, \int_a^t f(\tau) d\tau, f(t), \frac{df(t)}{dt}, \frac{d^2 f(t)}{dt^2}, ..., \frac{d^n f(t)}{dt^n}$$

Then, fractional calculus can be considered as the interpolation of the above sequence. The fundamental operator representing non-integer order differentiation and integration is denoted by

$${}_a\mathcal{D}_t^\alpha f(t),$$

where α is the order of the differentiation or integration, and typically $\alpha \in \Re$ but could also be complex [53], while a and t are the bounds of the operation. This operator is defined as

$${}_a\mathcal{D}_t^\alpha = \begin{cases} \frac{d^\alpha}{dt^\alpha}, & \alpha > 0, \\ 1, & \alpha = 0, \\ \int_a^t (d\tau)^\alpha, & \alpha < 0. \end{cases} \tag{3.1}$$

There are two main definitions of fractional calculus that have been widely used, namely Riemann-Liouville (RL), and Caputo definitions [23]. These two definitions are derived from the concept of the Cauchy n^{th} integration of function $f(t)$ [32]. When n is the positive integer number, n^{th} integration of function $f(t)$ is given by

$$f^{(-n)}(t) = \frac{1}{(n-1)!} \int_0^t (t-\tau)^{n-1} f(\tau) d\tau, \tag{3.2}$$

and if n is any positive real number, the formula is generalized to

$$f^{(-n)}(t) = \frac{1}{\Gamma(n)} \int_0^t (t-\tau)^{n-1} f(\tau) d\tau, \tag{3.3}$$

where the gamma function $\Gamma(n) = \int_0^\infty e^{-t} t^{n-1} dt$ is the generalization of the factorial function [51]. By combining the concept of integer order derivative and the Cauchy n^{th} integration, the α^{th} order derivative of a function $f(t)$ with respect to t defined by Riemann-Liouville (RL), also called the Left Hand Definition (LHD), is given as

$${}_a\mathcal{D}_t^\alpha f(t) = \frac{d^m}{dt^m} \left[\frac{1}{\Gamma(m-\alpha)} \int_a^t \frac{f(\tau)}{(t-\tau)^{\alpha+1-m}} d\tau \right], \quad (m-1) \leq \alpha \leq m, \tag{3.4}$$

where m is an integer. The reason that this definition is also called LHD can be seen from the example of differentiation of order 2.3 in Figure 3.1. On the other hand, the α^{th} order derivative of a function $f(t)$ defined by Caputo, also called the Right Hand Definition (RHD), is given as follows where m is an integer [23]:

$${}_a\mathcal{D}_t^\alpha f(t) = \frac{1}{\Gamma(m-\alpha)} \int_a^t \frac{f^{(m)}(\tau)}{(t-\tau)^{\alpha+1-m}} d\tau, \quad (m-1) \leq \alpha \leq m, \tag{3.5}$$

Again, the reason that Caputo definition is also called RHD can be visualized from Figure 3.1. Here, we will focus on Caputo's definition, which many engineering applications refer to, since it allows the formulation of initial conditions in a form involving only the values of integer order derivatives such as $f^{'}(0)$ and $f^{''}(0)$.

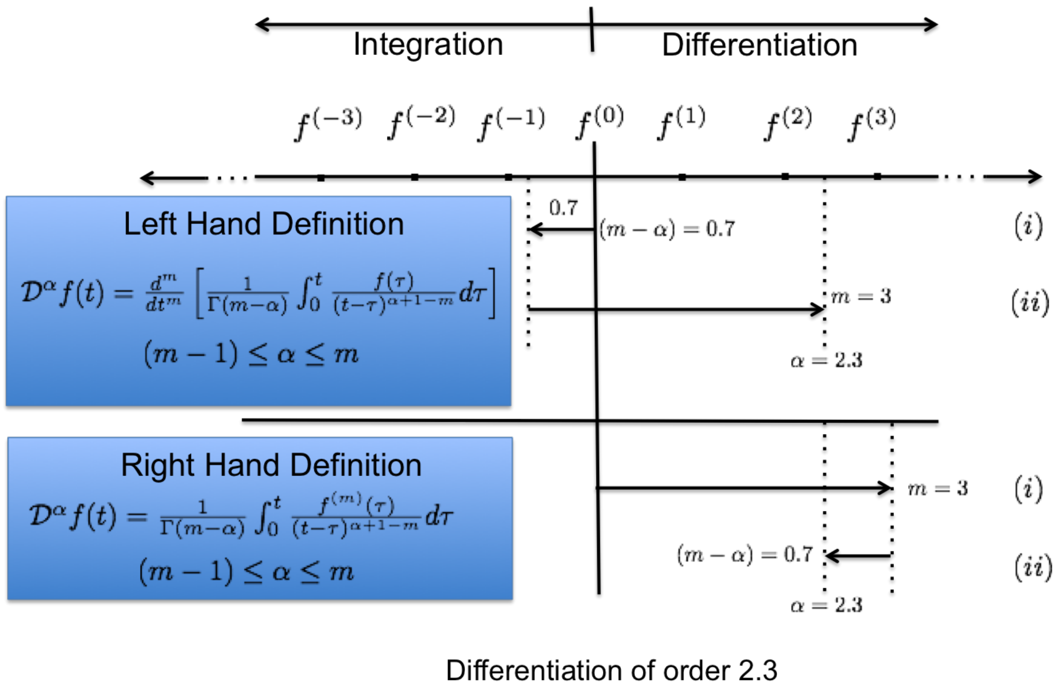

Figure 3.1: Fractional order calculus definitions

From the definition of fractional calculus, most natural phenomena can be modeled and explained more accurately by a fractional order differential equation. Consequently, many researchers, scientists, and engineers have been attempting to incorporate fractional calculus into their applications. For more fractional calculus definitions such as those by Abel, Fourier, and Cauchy, see references [51, 57, 60].

3.1.2 Fractional order systems

After establishing the definitions of fractional order calculus in the previous subsection, this subsection deals with the system that contains the fractional derivatives. First, consider the fractional order differential equation as follows

$$a_n D^{\gamma_n} y(t) + ... + a_0 D^{\gamma_0} y(t) = b_m D^{\beta_m} u(t) + ... + b_0 D^{\beta_0} u(t), \tag{3.6}$$

where γ_k $(k = 0, ..., n)$ and β_j $(j = 0, ..., m)$ are the differential orders. For the purpose of frequency domain design and analysis, Caputo's definition is usually used to derive the fractional order transfer function from the fractional order differential equation with zero initial conditions. The Laplace transform of this definition can be represented as

$$\mathcal{L}[{}_0\mathcal{D}_t^\alpha] = s^\alpha F(s) - \sum_{k=0}^{m-1} s^{\alpha-k-1} f^k(0), \quad (m-1) \leq \alpha \leq m, \tag{3.7}$$

where $F(s) = \int_0^\infty e^{-st} f(t)dt$ is the Laplace transform of $f(t)$. Once again, the Laplace transform of Caputo's definition involves lower bound at $t = 0$, for which a certain physical interpretation exists (for example, $f(0)$ is the initial position and $f^{'}(0)$ is the initial velocity). It shows that this particular transformation could be useful for solving applied problems with initial conditions in the traditional form. Then, by applying the Laplace transform to the fractional order differential equation in Eq. (3.6), we arrive at the following input-output representation

$$G(s) = \frac{Y(s)}{U(s)} = \frac{b_m s^{\beta_m} + ... + b_0 s^{\beta_0}}{a_n s^{\gamma_n} + ... + a_0 s^{\gamma_0}}. \tag{3.8}$$

A fractional order transfer function is said to be a commensurate fractional order transfer function if it is given by a differential equation where all the orders are multiple integer of a base order, α, and the transfer function can be written as

$$G(s) = \frac{\sum_{j=0}^{m} b_j (s^\alpha)^j}{\sum_{k=0}^{n} a_k (s^\alpha)^k}, \tag{3.9}$$

which can be considered as a pseudo-rational function, $G(\sigma)$, of the variable $\sigma = s^\alpha$,

$$G(\sigma) = \frac{\sum_{j=0}^{m} b_j \sigma^j}{\sum_{k=0}^{n} a_k \sigma^k}. \tag{3.10}$$

An example of a commensurate fractional order transfer function is as follows

$$G(s) = \frac{s^{1.8} + 3s^{1.2} + 5s^{0.6} + 1}{s^{1.8} + 2s^{1.2} + 7s^{0.6} + 2}; \quad \alpha = 0.6. \tag{3.11}$$

3.1.3 Stability of fractional order systems

For simplicity, a commensurate fractional order transfer function is used to define the stability condition of fractional order systems. The stability condition of a commensurate fractional order system is stated as follows [47]:

Theorem 1. The commensurate fractional order system is stable if and only if

$$|\arg(\sigma_k)| > \alpha\frac{\pi}{2}, \tag{3.12}$$

where σ_k, $k = 1, 2, ..., n$, are the roots of the polynomial of the denominator of a fractional order system as given in Eq. (3.10).For a particular case of $\alpha = 1$, it is the well known stability condition for an integer order linear time invariant system, where the system is stable if and only of the all poles lie in the left half plane as shown in Figure 3.2. Figure 3.3 shows the stability domain for the fractional order system where $0 < \alpha < 2$.

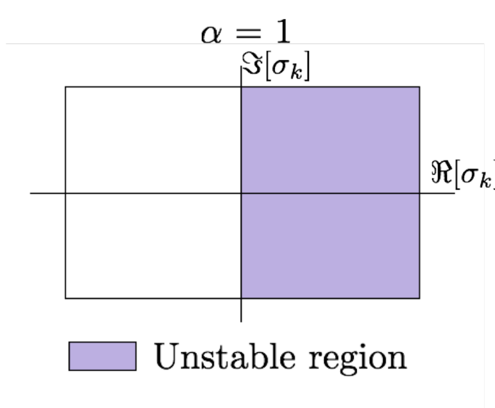

Figure 3.2: Stability condition map for an integer order system ($\alpha = 1$)

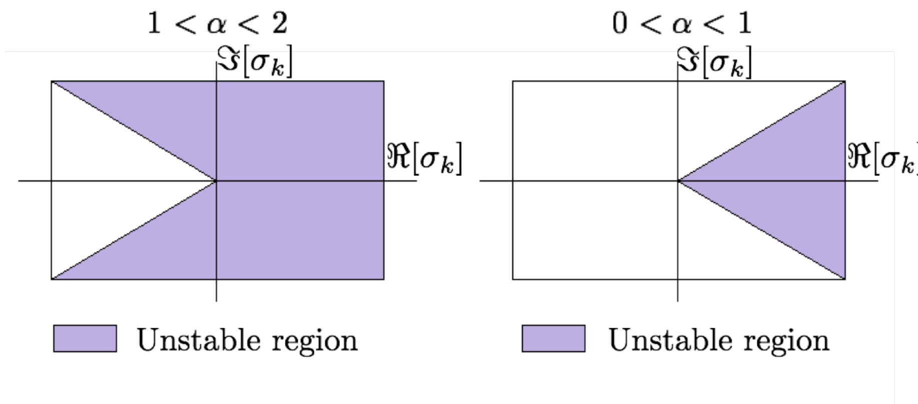

Figure 3.3: Stability condition map for a fractional order system ($0 < \alpha < 2$)

The following four examples show how to determine the stability of a commensurate fractional order system.

Example 1: $G(s) = \frac{1}{s^{\frac{2}{3}} - 5s^{\frac{1}{3}} + 8}; \alpha = \frac{1}{3}$.

$$\sigma_k = 2.5 \pm 1.3229j,$$
$$|\arg(\sigma_k)| = 0.155\pi < \alpha\frac{\pi}{2}.$$

Thus, the system is unstable.

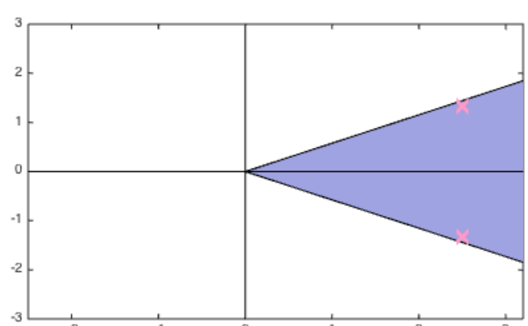

Figure 3.4: Stability domain of Example 1

Example 2: $G(s) = \frac{1}{s^{\frac{2}{3}} - 2s^{\frac{1}{3}} + 8}$; $\alpha = \frac{1}{3}$.

$$\sigma_k = 1.0 \pm 2.6458j,$$
$$|\arg(\sigma_k)| = 0.385\pi > \alpha\frac{\pi}{2}.$$

Thus, the system is stable.

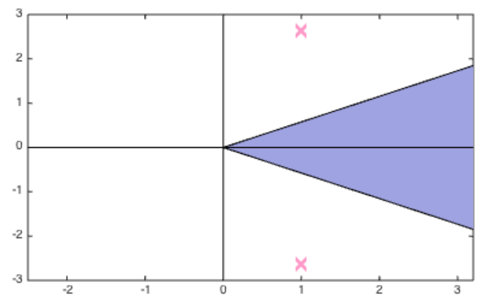

Figure 3.5: Stability domain of Example 2

Example 3: $G(s) = \frac{1}{s - 4s^{\frac{1}{2}} + 8}$; $\alpha = \frac{1}{2}$.

$$\sigma_k = 2 \pm 2j,$$
$$|\arg(\sigma_k)| = 0.25\pi = \alpha\frac{\pi}{2}.$$

Hence, the system is unstable.

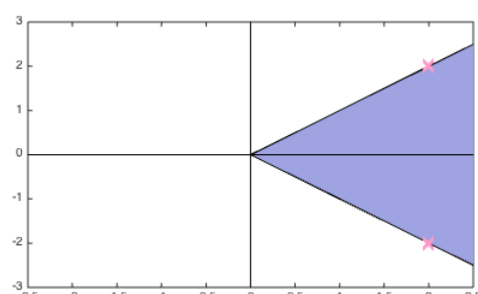

Figure 3.6: Stability domain of Example 3

Example 4: $G(s) = \frac{s^{\frac{4}{3}}-2}{s^{\frac{8}{3}}+4s^{\frac{4}{3}}+8}; \alpha = \frac{4}{3}$.

$$\sigma_k = -2 \pm 2j,$$
$$|\arg(\sigma_k)| = 0.75\pi > \alpha\frac{\pi}{2}.$$

Thus, the system is stable.

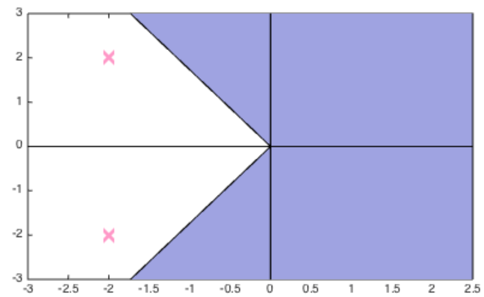

Figure 3.7: Stability domain of Example 4

3.1.4 Applications of fractional order calculus

There had not been many applications that involve fractional calculus in the past because of the lack of a simple geometrical interpretation, and the absence of solution methods for fractional order differential equations. However, the number of applications using fractional calculus has increased significantly in the past decades as more tools become available to help in solving complex fractional order differential equations. Examples of the toolbox available in MATLAB are N-integer [67], FOMCON [66] and CRONE [55]. Fractional calculus has been widely applied in many fields, such as viscoelasticity [3, 9, 24], electrochemistry [50], electromagnetism [27, 28], finance [36, 62], and control theory [22, 69].

The first sign of the potential of fractional calculus in control design was the work of Bode called *ideal cutoff characteristics* [13], where he proposed a feedback amplifier, in which the performance of the closed-loop is invariant to changes in the amplifier gain. The open loop transfer function that represents this characteristic can be expressed as

$$G_{\text{ideal}}(s) = \left(\frac{A}{s}\right)^{\alpha}, \tag{3.13}$$

where A is an amplifier gain and the value of α is the number of stages in a feedback amplifier. The value of α found in Bode's work was 1.667. However, afterwards, he described how to choose a suitable integer number of stages, which is not necessarily closest to the optimal non-integer number value of α. The extension of Bode's ideal loop arises from the fact that the phase of the open loop is constant. It can be expected that, if the gain increases or decreases by a certain percentage, the phase margin will remain unchanged. Therefore, in this case, the step responses with gains varying around the nominal gain will exhibit an iso-damping property [22], i.e., the overshoots of step responses will be almost the same as shown in Figure 3.8.

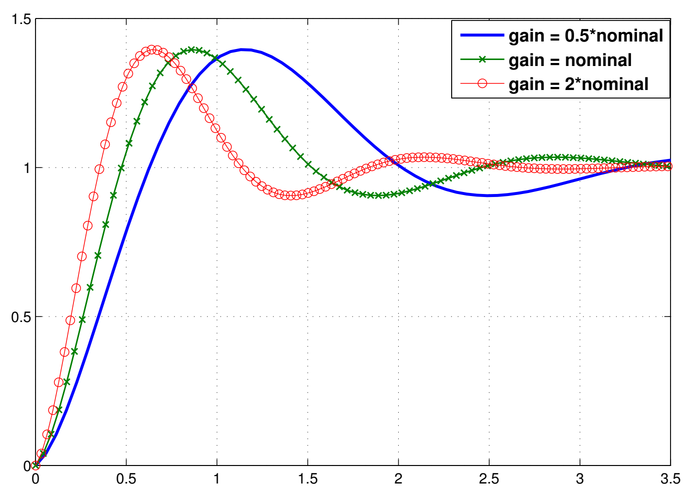

Figure 3.8: Iso-damping property

In theory, it will be most suitable if the fractional order plant is controlled by a fractional order controller. However, in practice, the integer plant model may have been already obtained from the physical characteristics. Therefore, the focus in most cases will be the development of fractional order controllers. After it is combined with the integer order plant, similar characteristics as suggested in Bode's work can still be achieved.

The first fractional order controller to appear in the literature is called Tilt-Integral-Derivative (TID) controller [45]. The TID controller is the modified version of the conventional PID controller where the proportional term is replaced by the transfer function $s^{-1/n}$ and n is a nonzero real number, preferably between 2 to 3. The aim of the TID controller is to provide more degrees of freedom to *tilt* or shape the open loop frequency response closer to the theoretically optimal response as mentioned in Bode's work. The benefits of the TID controller over the conventional PID controller is illustrated in [45].

Another well-known fractional order controller is called CRONE (Commande Robuste d'Ordre Non Entier, meaning Non-integer-order Robust Control) [53], which has the open loop transfer function template of a fractional derivative/integral order. The CRONE control is a frequency domain design to provide the robust control of perturbed plants using the common unity feedback configuration. For the nominal state of the plant, this approach involves determining the open-loop transfer function which guarantees the desired specifications such as rise time, overshoot and settling time. The controller can be obtained from the ratio of the open loop transfer function to the nominal plant transfer function. So far, three CRONE control generations have been developed. An example of the application in which CRONE control is successfully implemented can be found in [54].

In 1999, Podlubny [57] introduced a fractional order PID (FOPID) controller where the order of the derivative and integral terms are any real number. Podlubny's work shows that this type of controller outperforms the conventional PID controller. More details of the structure and characteristics of the FOPID controller will be explained in Section 3.2.

Applications of fractional calculus in control are numerous. In [8], the control of viscoelastic damped structure is presented. Control applications to a flexible transmission [54], an active suspension [4], a buck converter [14], a robotic manipulator [29], and a thermal system [33] are also found in the literature. For AMB system applications, there have also been a few works that make use of the fractional calculus concept. In [44, 76], the simplified model of eddy current losses in non laminated magnetic bearing is derived. The transfer function that represents the effective force $F_{\text{eff}}(s)$ after taking eddy current losses into account can be expressed as

$$F_{\text{eff}}(s) = \frac{R^0}{(cs^{0.5} + R^0)} \cdot F(s), \tag{3.14}$$

where $F(s)$ is the force input from the actuator, c is the coefficient of the total reluctance, and R^0 is the static value of the effective reluctance. This analytical model takes less time to obtain compared to the finite element method that is typically used for analysis. Moreover, this transfer function can be used directly for controller design. For the AMB control design in [42] the fractional order PID controller was designed to stabilize the AMB system by using the Particle Swarm Optimization (PSO) method to minimize the integral of time absolute error (ITAE) criterion. Other AMB control research can be found in [19], where the fractional order PID controller was designed by using the Genetic Algorithm (GA) to minimize overshoot, rise time, cumulative error, and control energy. The results reported in [42] and [19] show that FOPID control outperforms the conventional PID control in terms of error tracking and disturbance rejection. However, the designs of fractional order controller for AMB systems in both cases are only for the zero speed case. Furthermore, having only time domain specifications are not enough to guarantee the robustness requirement specified in the API and ISO standards for AMB supported machines. Lastly, experimental results of the proposed designs are not available, and the designs have not been validated in an actual application.

3.2 Fractional order PID control

Over the years, engineers and industrial practitioners aspired to substitute the traditional PID controller with a more powerful one. However, the PID controller remains the most popular due to its simplicity and clear physical interpretation of controller parameters. Recently, there has been an extension of the conventional PID controller by substituting the orders of the derivative and integral components to any arbitrary real numbers instead of fixing those orders to one. The fractional order PID (FOPID) controller was first introduced by Podlubny in 1999 [57]. The block diagram that represents the FOPID control structure is illustrated in Figure 3.9. The transfer function of an FOPID controller has the form of

$$C_{\mathrm{FOPID}}(s) = K_{\mathrm{P}} + \frac{K_{\mathrm{I}}}{s^{\lambda}} + K_{\mathrm{D}} s^{\mu}, \tag{3.15}$$

where λ is the order of the integral part, μ is the order of the derivative part, while K_{P}, K_{I}, and K_{D} are the controller gains similar to the conventional PID controller.

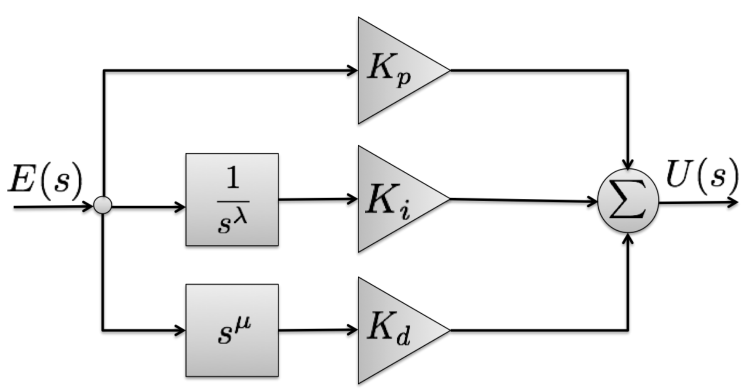

Figure 3.9: FOPID block diagram

3.2.1 Frequency domain characteristics

Similar to the classical PID controller, the FOPID controller behaves as a bandstop filter that passes most frequencies unaltered, but attenuates those in a specific range to very low levels. Generally, the integral part in conventional PID control helps the elimination of steady state error due to its infinite gain at zero frequency but it has 90 degree phase lag. On the other hand, the derivative part provides 90 degree phase lead, but has a large gain at high frequencies, which is susceptible to noise. By changing the derivative and the integral order in an FOPID controller, one can adjust the sharpness of the filter independently as illustrated in Figure 3.10. In the frequency domain, the magnitude curve of the fractional derivative and integral terms in the logarithmic scale can be calculated as

$$20 \cdot \log |s^{\mu}|_{s=j\omega} = 20\mu \cdot \log \omega, \tag{3.16a}$$

$$20 \cdot \log |s^{-\lambda}|_{s=j\omega} = -20\lambda \cdot \log \omega, \tag{3.16b}$$

and the phase plot is given by

$$\arg[s^{\mu}]_{s=j\omega} = \mu \frac{\pi}{2}, \tag{3.17a}$$

$$\arg[s^{-\lambda}]_{s=j\omega} = -\lambda \frac{\pi}{2}, \tag{3.17b}$$

For a special case, when μ and λ are equal to one, which represents integer order PID, the slope of the gain becomes -20 dB and the phase of the response is $-\frac{\pi}{2}$ radian in low frequencies. Similarly, the slope of the gain becomes $+20$ dB and the phase of the response is $+\frac{\pi}{2}$ radian in high frequencies.

Figure 3.10 confirms that, in the low frequency range, the slope of the gain becomes -20λ dB and the phase of the response is $-\lambda\frac{\pi}{2}$ radian. In the high frequency range, the slope of the gain becomes $+20\mu$ dB and the phase of the response is $+\mu\frac{\pi}{2}$ radian.

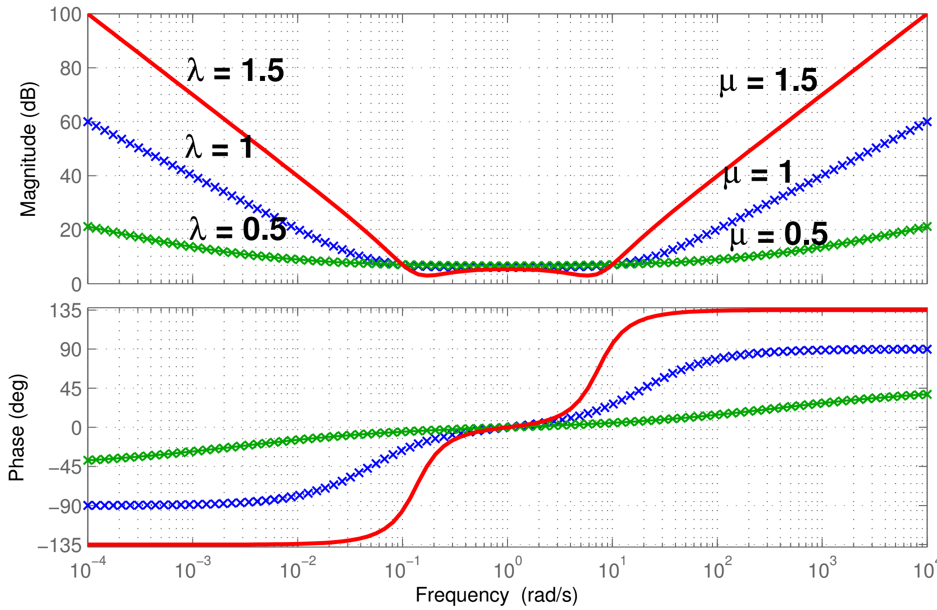

Figure 3.10: Frequency domain effects of fractional orders λ and μ

This shows that the FOPID controller preserves the characteristics of the traditional PID controller with additional flexibility in adjusting the phase and gain at the desired frequencies. This also implies that the FOPID controller, if properly tuned, may have a higher potential to meet the desired frequency domain specifications of the closed-loop system.

3.2.2 Time domain characteristics

In the control design process, another important specification is the transient response performance. Typically, the unit step response is used for the reference input signal in order to show the performances of the closed-loop system. To investigate the effects of fractional derivative and integral order in the FOPID controller, we consider the magnetic levitation system with one degree of freedom from [37], which has the following transfer function

$$P(s) = \frac{18400}{s^2 - 2.418s - 3998}.$$

This system has two poles at 64.45 and −62.03, which implies that the system is open loop unstable. Therefore, a PD controller is needed to stabilize the system. For the stability purpose, the values of K_{P} and K_{D} are chosen to be 8.476 and 0.022, respectively. To see the effect of the derivative gain, we observe the unit step response as the value of the K_{D} is varied as shown in Figure 3.11. It is clear that varying the derivative gain K_{D} will affect the size of the overshoot of the unit step response. In order to investigate the effect of fractional order derivative, the values of K_{P} and K_{D} are fixed to the nominal values and the fractional order μ of the derivative is varied. The unit step response with varying values of μ is shown in Figure 3.12. It can be seen that varying the value of μ can further reduce the overshoot.

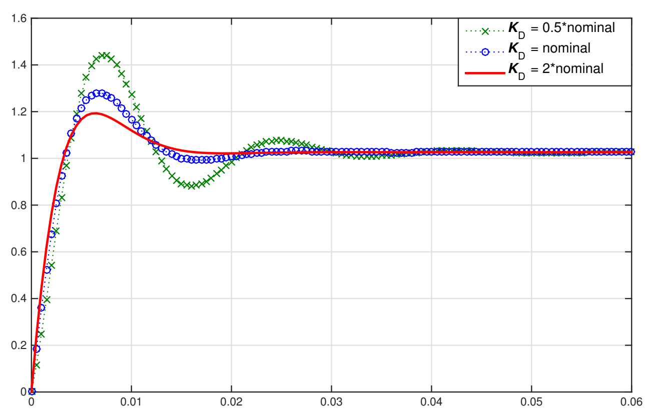

Figure 3.11: Time domain effects of derivative gain

As can be seen in both Figures 3.11 and 3.12, the steady state error is not exactly zero. Therefore, an integrator is added. Figure 3.13 shows the unit step responses with different values of K_{I} for integer order PID control with a nominal value of K_{D} as mentioned above. It can be seen that the steady state errors are eliminated. Also,

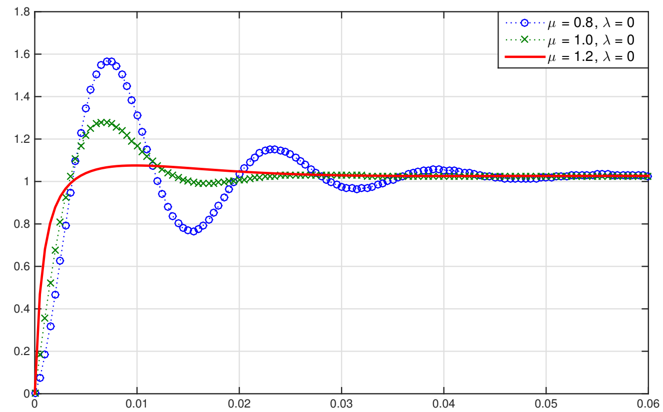

Figure 3.12: Time domain effects of fractional derivative order

the response that converges faster will have higher overshoot. Moreover, Figure 3.14 shows the unit step responses for different values of λ in the fractional order PID controller with nominal values of K_{D} and K_{I}. When λ is changed to 1.4, the overshoot is smaller than the integer order case and the settling time is approximately the same. This shows that varying fractional order derivative can further improve the transient response performances.

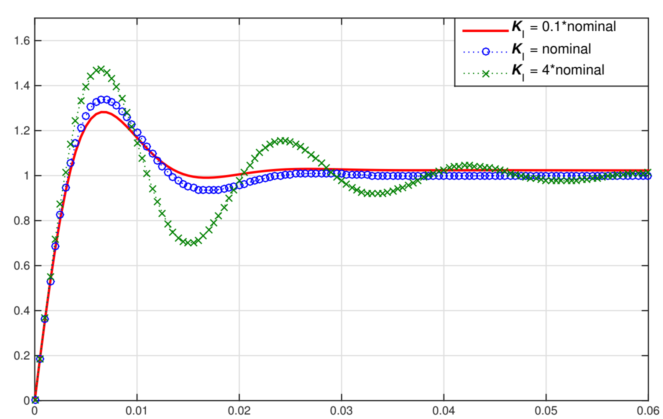

Figure 3.13: Time domain effects of integral gain

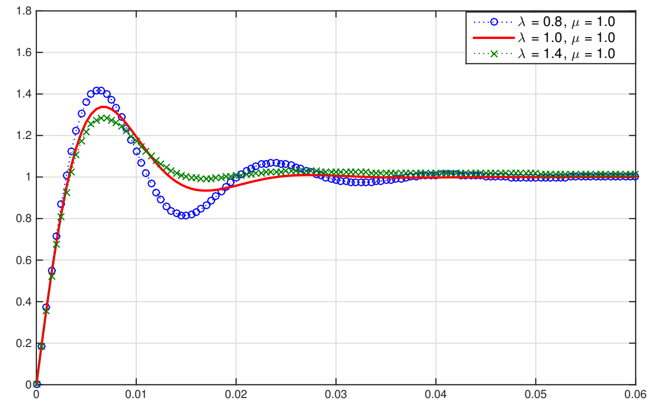

Figure 3.14: Time domain effects of fractional integral order

For the optimal performance comparison between the integer and fractional PID control in the time domain, the values of the controller gains are fixed to be the same in both integer and fractional order controllers while the fractional derivative and integral orders are changed to 1.18 and 1.13, respectively. The unit step responses of both cases are shown in Figure 3.15. It is clearly seen that the transient response performance can be improved significantly by varying the values of the derivative and integral orders.

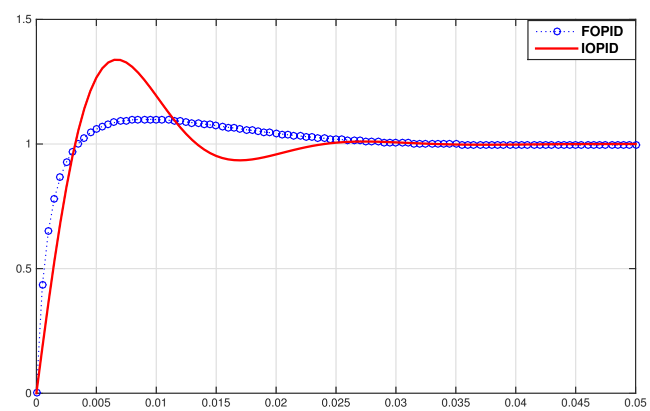

Figure 3.15: Step responses of FOPID and IOPID controllers

Essentially, both frequency and time domain specifications can be improved because FOPID control expands the four discrete control configurations (P, PI, PD, and PID) of the classical PID control to the range of control configurations in the quarter-plane defined by selecting the values of λ and μ as illustrated in Figure 3.16. Furthermore, the improvement of transient responses by using FOPID illustrated above is only obtained by observation of order variation. The better result can be achieved by fine tuning all five parameters of the FOPID control.

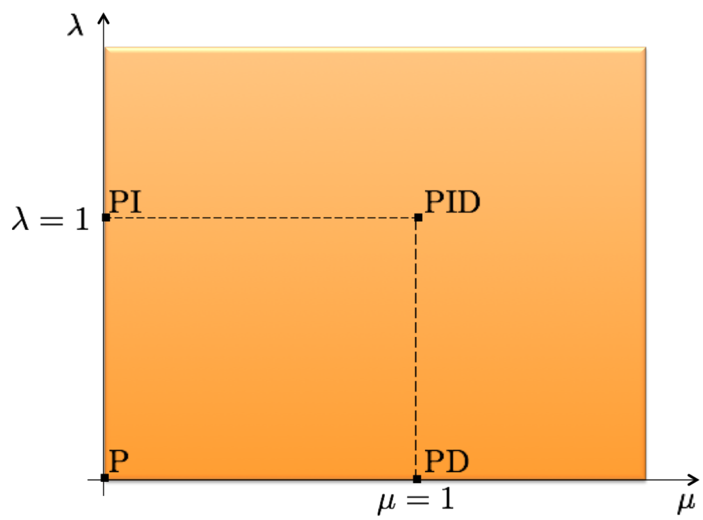

Figure 3.16: Parameters in the FOPID control

3.3 Fractional order PID tuning methods

With the additional flexibility of fractional derivative and integral orders of FOPID introduced in the previous section, controller parameter tuning is another important factor to pay attention to. There have been tremendous contributions on tuning methods for FOPID controller in the past years. FOPID tuning methods can be categorized by three major approaches including, analytical, rule-based, and numerical tuning methods [68]. The analytical and rule-based methods are widely used in many studies. These methods mainly concern the phase margin, gain margin, gain crossover frequency, and dominant poles. The studies of analytical tuning for FOPID can be found in [17, 46, 75]. The available rule-based methods can also be extended to the auto-tuning method by incorporating an additional test such as relay feedback test into the loop [49, 70].

One of the drawbacks of these two methods is the assumption that a plant is of minimum phase and open loop stable. Because of this limitation, this study will focus only on the numerical tuning method due to the fact that AMB systems are open loop unstable. The aim of numerical tuning methods is to optimize the specified objective functions with respect to the five adjustable parameters (K_{P}, K_{I}, K_{D}, λ, and μ).

3.3.1 Formulation of the objective function

Objective functions used for optimization can be categorized into two types, the time domain and frequency domain objectives.

Time domain objectives

Transient response performances subject to unit step reference are often used as the time domain objectives in the optimization process. These performances include overshoot, rise time, settling time, and steady state error. Sometimes, the system requirement only emphasizes on a single performance. In this case, the optimization process usually is simple. On the other hand, if two or more performances are set as the objective functions, a conflict may occur during optimization which can cause degradation in some objectives. To deal with these conflicts, performance indices are introduced, in terms of the accumulation error over time, to quantify these performances. Some of the frequently used performance indices are

$$\begin{aligned}
\text{IE} &= \int_0^\infty e(t)dt, \\
\text{IAE} &= \int_0^\infty |e(t)|dt, \\
\text{ISE} &= \int_0^\infty e^2(t)dt, \\
\text{ITAE} &= \int_0^\infty |e(t)|tdt, \\
\text{ITSE} &= \int_0^\infty [e(t)\cdot t]^2 tdt, \\
\text{ISESC} &= \int_0^\infty [e(t)^2 + \beta(u(t)-u_\infty)^2]dt.
\end{aligned}$$

Integral Error (IE) is suitable for highly damped or monotonic responses. Integral Absolute Error (IAE) is suitable for non-monotonic responses. For a system that concerns more on the overshoot performance, Integral Square Error (ISE) is recommended because it highly penalizes large control errors, even though the settling time will be longer. Integral Time Absolute Error (ITAE) and Integral Time Square Error (ITSE) have an effect similar to IAE and ISE, respectively, but they add a heavy penalty for errors that do not die out rapidly. Integral Square Error and Square Control Effort (ISESC) take into account the control energy. Typically, the overshoot will be larger, but with a shorter settling time and the choice of the weight β is subjective.

Frequency domain objectives

Most studies of numerical tuning methods for FOPID controllers used only time domain objectives. Therefore, the results cannot indicate some important specifications such as robust stability and disturbance rejection capability. These specifications are defined in the frequency domain. Some of the frequently used specifications are

- Sensitivity function:

$$S(s) = \frac{1}{1+L(s)}.$$

- Complementary sensitivity function:

$$T(s) = \frac{L(s)}{1 + L(s)}.$$

- Disturbance sensitivity:

$$S_{\mathrm{d}}(s) = \frac{G(s)}{1 + L(s)}.$$

- Control sensitivity:

$$S_{\mathrm{u}}(s) = \frac{C(s)}{1 + L(s)},$$

where $G(s)$ represents the plant, $C(s)$ represents the controller, and $L(s)$ is the loop transfer function ($L(s) = G(s)C(s)$). With the specifications mentioned above, the optimization goal is mostly to minimize the H_∞ or H_2 norm of the specified objective. Some examples of objective functions using the above transfer functions are

- Disturbance rejection objective function:

$$J_{\mathrm{d}} = \left\| \frac{1}{s} S_{\mathrm{d}}(s) \right\|_\infty .$$

- Control output objective function:

$$J_{\mathrm{d}} = \left\| S_{\mathrm{u}}(s) \right\|_\infty .$$

- Robust stability objective function:

$$J_{\mathrm{S}} = \left\| W_{\mathrm{S}}(S) S(s) \right\|_\infty .$$

- Noise rejection objective function:

$$J_{\mathrm{T}} = \left\| W_{\mathrm{T}}(s) T(s) \right\|_\infty .$$

Here, $W_{\mathrm{S}}(s)$ and $W_{\mathrm{T}}(s)$ are weighing functions that shape the robust stability noise rejection performances at the desired frequency.

- Set-point tracking objective function:

$$J_{\mathrm{t}} = \left\| \frac{1}{s} S(s) \right\|_2 .$$

Moreover, to guarantee the stability of the closed-loop system, the following condition must be satisfied.

$$\Re(\mathrm{eig}(T(s))) < 0. \tag{3.18}$$

Note that the described time and frequency domain objectives can be combined as a single objective function with different weights on each objective. This allows the optimization problem to be computed in less time. Alternatively, each objective can be optimized individually by using the approach of multi-objective optimization, resulting in an optimal solution for each objective. In this case, additional computing time is required to determine the final optimal solution.

3.3.2 Optimization algorithms

Many optimization algorithms for control design have been studied to examine their effectiveness for different purposes. Evolutionary Algorithms (EAs) are one of the most efficient and robust optimization methods. EAs are influenced by the principles of natural selection proposed by Charles Darwin. The idea of "the survival of the fittest" is the key concept behind all evolutionary algorithms [31]. These algorithms are also able to cope with systems that are highly nonlinear, discontinuous, and time-varying. The reason that EAs have become a popular alternative optimization algorithm is that the *evolution* process enhances the global minimum search whereas conventional optimization algorithms are based on a local gradient search. One of the most popular EAs used with FOPID control design is the Genetic Algorithm (GA) (see [16, 18, 19]). Other popular evolutionary algorithms used with FOPID control design include particle swarm optimization (PSO) [10, 15], differential evolution (DE) [11, 20], and various modifications of the mentioned methods. It is also convenient that all of the mentioned evolutionary algorithms are easily implemented in software.

Genetic Algorithm (GA)

GA is the heuristic optimization algorithm influenced by the concept of the population genetics. The following are the steps involved in the algorithm:

1. Initialize population: The population of the search is set by converting the controller parameters to binary strings known as chromosomes, where each chromosome represents a possible solution of the problem. Note that the size of the population for each generation is set by the user at the beginning.

2. Objective evaluation: Each generated chromosome is evaluated based on the specified objective function.

3. Selection: Chromosomes will be selected based on the level of their fitness. The higher fitness level of an individual chromosome, the better chance it will be selected.

4. Crossover: The selected chromosomes will randomly exchange some bit(s) to generate the offspring for an evaluation in the next iteration. This process helps expand the possibility of the search space.

5. Mutation: The mutation operator will make some small, random, change to the *surviving* chromosomes. This process prevents the solutions from being trapped in local minima. Typically, a low mutation rate is chosen, otherwise the search will become totally random.

6. Elitism: The best found solution in each generation may be lost in the subsequent generation due to the crossover and mutation processes. Therefore, elitism is introduced to simply copy the best found chromosomes to the next generation. Normally, the number of elite is chosen to be a small fraction of the overall population so that the optimization process is not biased on these solutions.

Differential Evolution (DE)

DE is introduced by Storn and Prince in 1995 [65] and is essentially the refined version of the GA with some changes that overcome the disadvantage of the GA. The DE algorithm has an optimization process similar to GA, except that DE uses floating point number instead of bit representation for solution vectors [59]. Therefore, instead of logical operators used in GA, DE uses arithmetic operators for mutation and crossover processes, which lower the computational complexity and facilitate greater flexibility in the design of the mutation distribution [56]. The optimization step of the DE algorithm is slightly different from GA and can be summarized as follows:

1. Initialize population: The population is initialized randomly and uniformly distributed in the range of the specified lower and upper bound of the variables. The size of the population generated is prescribed by the user.

2. Mutation: First, three solution vectors from the initial population are chosen randomly. Then the donor vector d_i is generated by adding the weighted difference of the first two vectors, x_{r1} and x_{r2} to the base solution vector x_{r0}, as shown in Eq. (3.19),

$$d_i = x_{r0} + F(x_{r1} - x_{r2}). \tag{3.19}$$

There are some modifications to let x_{r0} be the best solution from the initial population. Generally, the factor F can vary between 0 and 2, which makes the

DE algorithm sensitive to the choice of F. As suggested in [59], a good initial value of F is between 0.5 and 1.

3. Crossover: To increase the diversity of the population, the donor vector d_i exchanges its components with the base vector x_{r0} to form the trial vector u_i with the crossover probability C_r. The range of C_r is between 0 and 1, where the value of C_r equals to 1 means that all components of the donor vector d_i are replaced by the base vector x_{r0}. The initial good guess of C_r value is 0.5 in order to maintain the diversity of the population.

4. Selection: At this stage, the trial vector u_i is evaluated. If the trial vector yields the lower value of the objective function, then it replaces the corresponding base vector x_{r0} in the next generation. Otherwise, base vector x_{r0} is retained in the population. Hence, the population either gets better or remains the same (with respect to the minimization of the objective function), but never deteriorates.

The process is iterated and terminated when a specified number of iterations are exceeded or the value of the objective function falls below a prescribed value. For more variations of the mutation and crossover scheme, see [59].

Particle Swarm Optimization (PSO)

PSO is a population-based stochastic optimization technique developed by Eberhart and Kennedy in 1995 [26]. The method is inspired by the social behavior of bird flocking, fish schooling, etc. Unlike the GA and DE algorithms that use the concept of the fittest to survive, PSO algorithm uses the particles that constitute a swarm to move around the prescribed space in order to find the best solution. Each particle adjusts its position x_j based on its experience from previous iterations as well as the experience of other particles. The two important values used for adjusting the moving direction in the concept of PSO are the best solution of each particle (*pbest*) and the best solution of the entire swarm (*gbest*). The searching algorithm to calculate the new position of each particle based on *pbest* and *gbest* is described in the following equations:

$$v_{j,N}^{(t+1)} = w \cdot v_{j,N}^{(t)} + c_1 r_1 (pbest_{j,N} - x_{j,N}^{(t)}) + c_2 r_2 (gbest - x_{j,N}^{(t)}), \tag{3.20a}$$

$$x_{j,N}^{(t+1)} = x_{j,N}^{(t)} + v_{j,N}^{(t+1)}, \tag{3.20b}$$

where $v_{j,N}^{(t+1)}$ is the velocity of particle j at iteration t, with $j = 1,2,...,n$, $N = 1,2,...,m$, and

- n is the number of particles (population size);
- m is the dimension of the problem (number of variables);
- c_1, c_2 are the acceleration factors;
- r_1, r_2 are the uniformly distributed numbers between 0 and 1.

The weight w provides a balance between local and global exploration. The value of w often decreases linearly from $w_{\max} \approx 0.9$ to $w_{\min} \approx 0.4$. The value of w is given by

$$w = w_{\max} - \frac{w_{\max} - w_{\min}}{iter_{\max}} \times iter \tag{3.21}$$

where $iter_{\max}$ is the maximum number of the iteration and $iter$ is the current number of iterations.

3.4 Fractional order PID controller implementation

A feasible way to implement a fractional order operator is to use a finite dimensional integer order transfer function, which requires approximation. The fractional order operator can be approximated in both continuous time and discrete time. This work will focus on continuous time approximation because the result of approximation in continuous time is more suitable for further analysis.

One of the well-known approximation methods is proposed by Oustaloup [52]. Oustaloup's approximation of fractional order α in the specified frequency range $[\omega_l, \omega_h]$ is given as

$$s^\alpha = K \prod_{k=1}^{N} \frac{s + \omega_k'}{s + \omega_k}, \qquad 0 < \alpha < 1, \tag{3.22}$$

where N is the number of poles and zeros which is chosen beforehand and a good approximation strongly depends on this number. Then, the zeros, poles, and gain are evaluated as

$$\omega_k' = \omega_l \omega_u^{(2k-1-\alpha)/N}, \quad \omega_k = \omega_l \omega_u^{(2k-1+\alpha)/N}, \quad \omega_u = \sqrt{\omega_h/\omega_l}, \quad K = \omega_h^\alpha.$$

For the case $\alpha < 0$, the right hand side of equation (3.22) will be inverted. But if $|\alpha| > 1$, the approximation becomes unsatisfactory. Accordingly, it is usual to split the fractional power of s into the following form

$$s^\alpha = s^n s^\gamma,$$

where n is an integer number, $\alpha = n + \gamma$, and $\gamma \in [0,1]$. In this manner, only the s^γ term needs to be approximated.

It has been proven that this approximation method is accurate enough for the implementation purpose [53]. Modified versions of Oustaloup's approximation can be found in [71, 72].

Additionally, attempts have also been made for analog realization of a fractional order controller by using a combination of resistors, inductors, and capacitors [21, 58].

However, modifications are difficult to be made on analog devices.

Chapter 4

Description of the Test Rig

In this chapter, the single-stage compressor test rig equipped with AMBs and its components used in this study are described. Then models of lateral and axial rotor dynamics are derived for the FOPID control design for rotor suspension. Lastly, the compression system model is derived for the FOPID control design for surge control.

4.1 Overview of the test rig

For the purpose of investigating the capability of AMBs in high-speed compressor applications, the single-stage centrifugal compressor equipped with AMBs was built and commissioned in the Rotating Machinery and Control Laboratory (ROMAC) at the University of Virginia, as shown in Figures 4.1 and 4.2. Specifically, this test rig is used as a platform to demonstrate flow instabilities caused by surge in a centrifugal compressor. The rotor is levitated by two radial AMBs for smooth rotation without mechanical contact. The rotor is supported axially by the thrust AMB, which is also used to modulate the impeller tip clearance for the purpose of surge control. The designed maximum operational speed is 23,000 RPM, which requires a power supply of 52 kW.

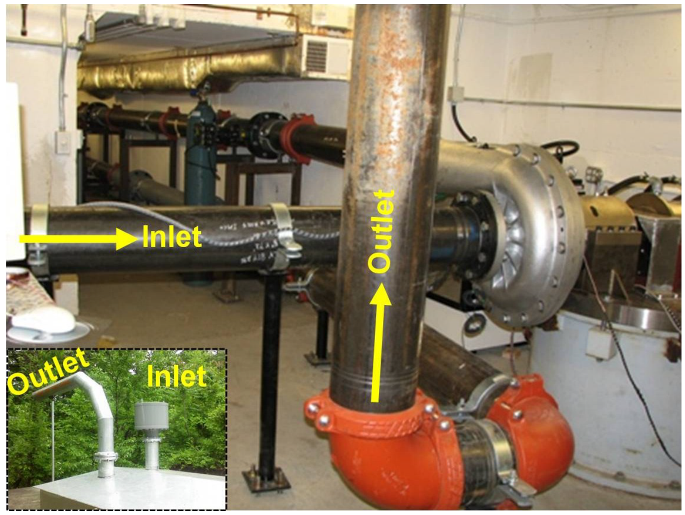

Figure 4.1: Compressor and piping system

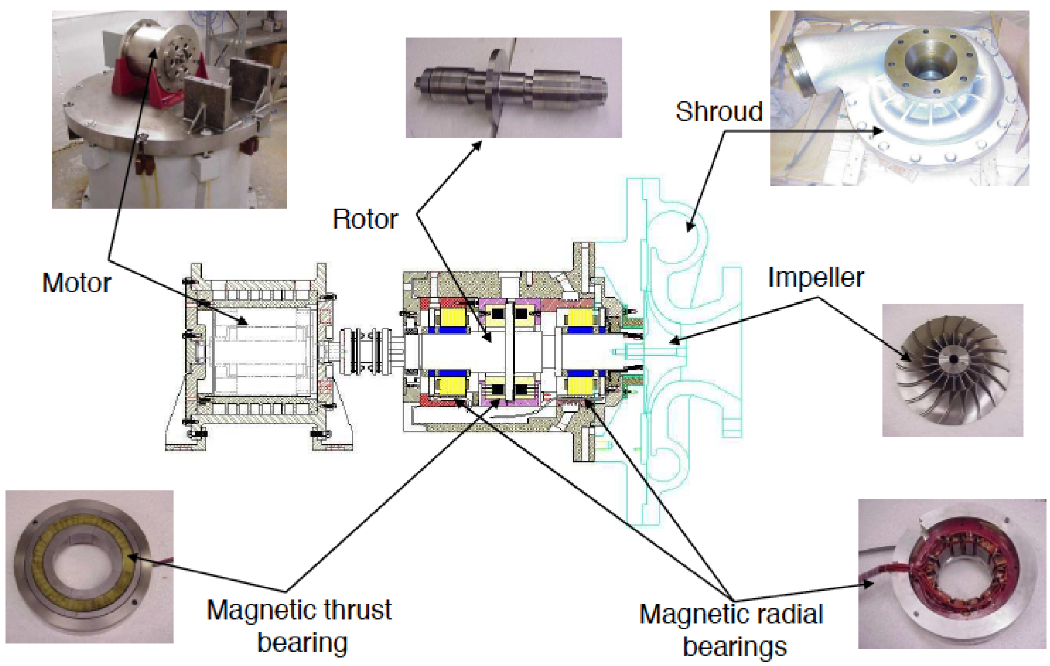

Figure 4.2: Centrifugal compressor components

For the control design purpose, the test rig can be divided into two main subsystems, the suspension system and the compression system.

4.2 Suspension system

For this test rig, instead of mechanical bearings, AMBs are used to support the rotor for smoother operation and an ability to control the rotor position actively.

4.2.1 Components

Components in the suspension system include the following.

Rotor

Within the operating speed range (maximum at 23,000 rpm), the rotor is considered to be a rigid rotor since the first bending mode is at 40,792 rpm. The rotor has a length of 0.517 m and is 27 kg in mass. This rotor is made of AISI 4340 steel. As can be seen in Figure 4.3, the thrust disk is integrated at the midspan of the rotor as a target for the thrust AMB. In order to reduce the eddy current effect, the laminations for two radial AMBs are also attached at both ends of the rotor.

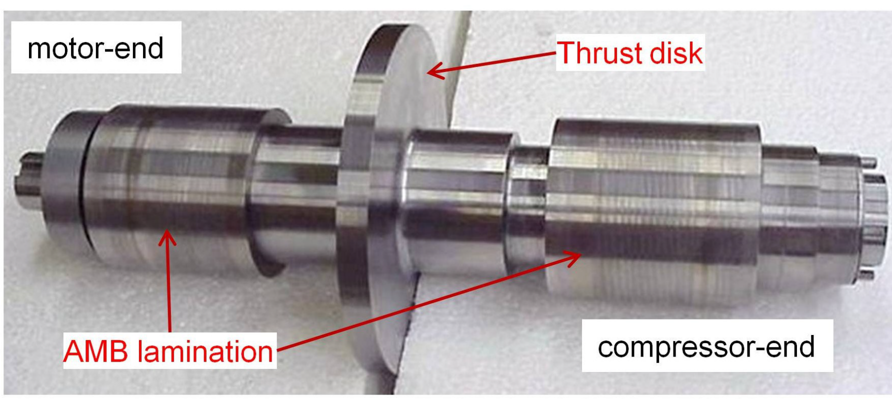

Figure 4.3: Rotor

Active magnetic bearings

- Radial AMBs

  AMBs used for radial suspension are 12 poles E-core design, which are separated into four quadrants. The width of the primary and secondary poles are 27.94 mm and 13.97 mm respectively. Each pole has 51 turns of 17 AWG wire. Similar to the rotor, the stators of the radial AMBs are laminated in order to reduce the eddy current effect. The designed maximum load capacity per quadrant is 1,414 N and the nominal air gap is 0.5 mm.

From the design analysis, the compressor-side AMB is subject to a higher disturbance due to the aerodynamic forces on the impeller. The worst case disturbance of the compressor-side AMB is approximated to be 455 N and 231 N for the motor-side AMB. Therefore, the selected bias current, I_b, for the motor-side AMB was 3 A and slightly raised to 4 A for the compressor-side AMB. The corresponding values of negative stiffness K_x and current gain K_i were obtained experimentally and summarized in Table 4.2.1.

Radial AMB	I_b (A)	K_x (N/m)	K_i (N/A)
Motor side	3	1.27×10^6	199.34
Compressor side	4	2.26×10^6	265.86

Table 4.1: Radial AMB properties

- Thrust AMB

  Thrust AMB is used to regulate the axial position of the rotor by the double acting force from two coils to the thrust disk. The clearance in the axial direction is 0.5 mm. The predicted axial load on the impeller was 3,300 N. Therefore, the target load capacity is selected to be 6,600 N for the capability to supply additional force during a surge control event. The bias current for the thrust AMB is chosen to be 5 A. The corresponding values of negative stiffness K_x and current gain K_i are summarized in Table 4.2.1. Unlike the radial AMBs, the lamination for the reduction of eddy current effects cannot be implemented due to the limitations in the manufacturing process. Therefore, the effect of the eddy current needs to be included in the model for the control design. The eddy current model will be discussed in Section 4.2.3.

AMB	I_b (A)	K_x (N/m)	K_i (N/A)
Thrust AMB	3	4.23×10^6	664.12

Table 4.2: Thrust AMB properties

Instrumentation

To measure the displacement of the compressor rotor in the radial direction, variable reluctance sensors are placed near the location of radial AMBs. For the axial position measurement, the eddy proximity type sensors are used. These displacement values are necessary for the feedback control of AMBs. Power amplifiers are also required to supply electrical current to the coils which generate the electromagnetic forces. Power amplifiers will convert the control output voltage to electrical current. The instrumentation properties are summarized in Table 4.2.1.

AMB	Motor side	Compressor side	Thrust
Amplifier gain (A/V)	1.5	1.5	1.5
Amplifier bandwidth (rad/s)	5026.5	5026.5	5026.5
Sensor gain (V/m)	3.937×10^4	3.937×10^4	3.937×10^4
Sensor bandwidth (rad/s)	1.26×10^4	1.26×10^4	1.26×10^4
Maximum slew rate (N/s)	2.2×10^6	2.2×10^6	1.9×10^6

Table 4.3: Instrumentation properties

4.2.2 Rotor lateral dynamics

The rotor lateral dynamics can be represented as the block diagram shown in Figure 4.4, where the rotor model is derived by the finite element analysis approach. The values of negative stiffness K_x and current gain K_i are summarized as mentioned in

Section 4.2.1. The complete radial AMB system combines the rotor-AMB model with

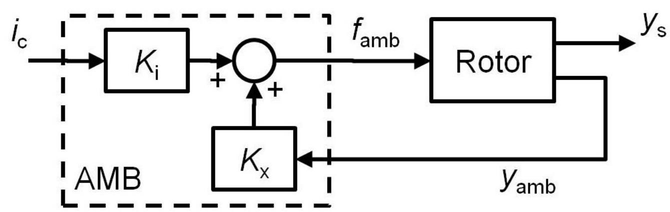

Figure 4.4: Rotor-AMB system block diagram

the power amplifiers, sensors, and time delay models as shown in Figure 4.5. The control output voltage v_c is the input to the system and the sensor measurement voltage v_s is the output of the system. A time delay is also added to complete the model in order to represent the sampling and computational delays that occur in the digital controller.

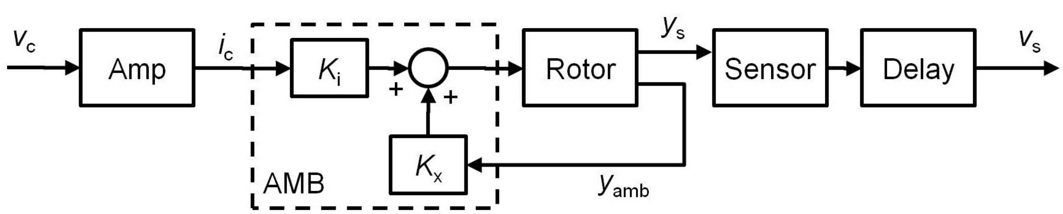

Figure 4.5: Radial AMB system block diagram

4.2.3 Rotor axial dynamics

The rotor axial dynamics can be simply represented as a single mass, and the equation of motion is

$$m_{\mathrm{r}}\ddot{z} = u_z, \tag{4.1}$$

where m_{r} is the rotor mass, $\ddot{z}$ is the axial acceleration, and u_z is the axial external force acting on the rotor. As mentioned in Section 4.2.1, laminations are not practical to manufacture for the thrust AMB. This means that the eddy current losses need to be included. The eddy current loss model was proposed by Zhu in [76]. The transfer function that represents the effective force $F_{\text{eff}}(s)$ after taking eddy current losses into account can be expressed as

$$F_{\text{eff}}(s) = \frac{R^0}{(cs^{0.5} + R^0)} \cdot F(s), \tag{4.2}$$

where $F(s)$ is the force input from the actuator, c is the coefficient of the total reluctance, and R^0 is the static value of the effective reluctance. For simplicity in the design process, the effective force $F_{\text{eff}}(s)$ is approximated to integer order form. The rotor-AMB model in the axial direction can be represented as the block diagram in Figure 4.6. The more complete thrust AMB model is constructed the same way as illustrated in Figure 4.5.

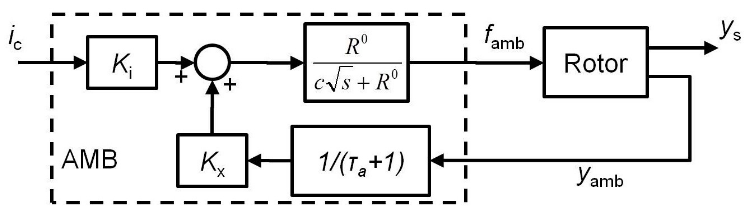

Figure 4.6: Thrust AMB system block diagram

4.2.4 Integer order model versus fractional order model

Normally, integer order models are used for the control design and are derived from the physical properties of the system and some parameters are tuned based on experimental data. However, since the fractional order controller will be designed, it is worthwhile to investigate how well the fractional order system model can capture the dynamics of the system. In order to justify the accuracy of the models, the experimental frequency responses of lateral and axial rotor dynamics are compared to the integer order and fractional order models. The integer order models are already derived in Sections

4.2.2 and 4.2.3 by using the physical properties of the system as well as the additional tuning based on experimental data. On the other hand, the fractional order model is obtained from the system identification with the model structure

$$\tilde{G}(s) = \frac{\sum_{j=0}^{m} b_j (s^q)^j}{\sum_{k=0}^{n} a_k (s^q)^k}, \tag{4.3}$$

where m is the order of the numerator, n is the order of the denominator, and q is the fractional order. For the identification process, these three parameters need to be specified beforehand. The identification method used for this case is the least square method. The method searches for coefficients of the numerator and the denominator by minimizing the following cost function J within a specified frequency range,

$$J = \int_{-\infty}^{+\infty} \left| G(j\omega)\frac{1}{j\omega} - \tilde{G}(j\omega)\frac{1}{j\omega} \right|^2 d\omega. \tag{4.4}$$

The objective of this cost function is the minimization of the square error between the identified model $\tilde{G}(j\omega)$ and the response data $G(j\omega)$. The resulting parameters from the identification of the fractional order system model are given in Table 4.4.

Figures 4.7 show the comparison of the frequency responses of the lateral dynamics. The measurement is from the control output voltage $\mathrm{v_c}$ to the sensor measurement voltage $\mathrm{v_s}$ as shown in Figure 4.5. Figure 4.8 show the comparison of the frequency responses of the axial dynamics, and the response data is measured in a similar way to the lateral dynamics. Table 4.5 summarizes the percentage fit to the measurement of both the integer order and the fractional order models.

Plant	q	n	m
Motor side (MS)	0.36	9	9
Compressor side (CS)	0.51	9	9
Thrust (TH)	1.15	4	4

Table 4.4: The parameters of the identified fractional order model

% fit to measurement of	MS	CS	TH
IO model	96.07%	95.08%	98.99%
FO model	99.86%	99.77%	99.91%

Table 4.5: The percentage fit of the models to the measurement

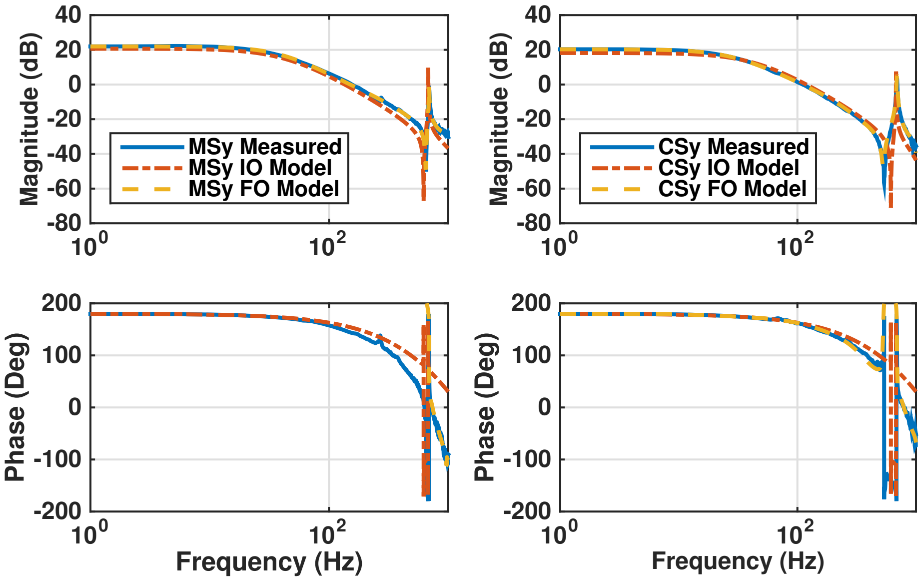

Figure 4.7: Frequency responses of the models and the measurement of the lateral rotor dynamics

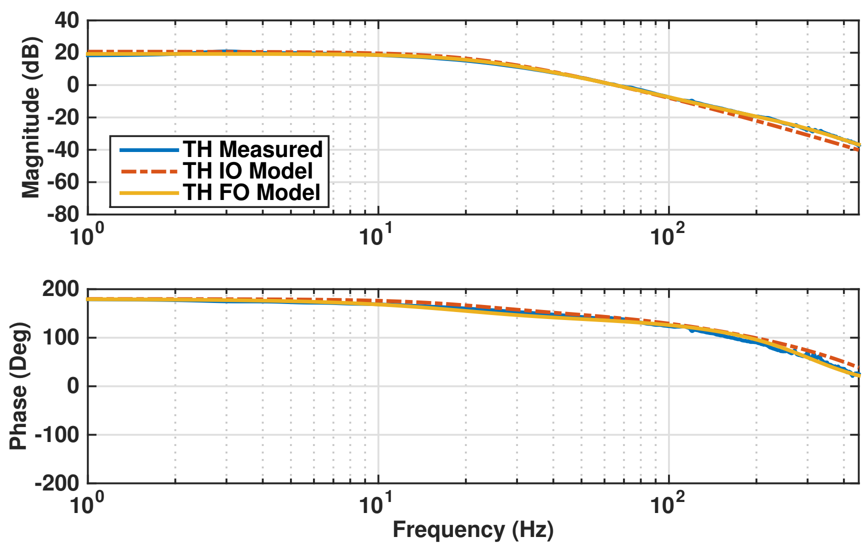

Figure 4.8: Frequency responses of the models and the measurement of the axial rotor dynamics

It can be observed that both models fit the measurement very well. Therefore, for this study, the integer order models will be used for the control design in order to avoid the computational error resulting from the more complicated fractional order models.

4.3 Compression system

4.3.1 Components

The compression system consists of three main components, the centrifugal compressor, the modular ducting system, and the throttle valve. The location of each component installed in the system is illustrated in Figure 4.9.

1. Centrifugal compressor: The compressor is a single stage with an unshrouded impeller as shown in Figure 4.2. It was manufactured and donated by Kobe Steel, Ltd, Japan. The compressor design parameters are summarized in Table 4.6. For this compressor, the impeller tip clearance, which is the axial clearance between the static shroud and the impeller tip, is regulated by the thrust AMB.

Parameter	Unit	Value
Maximum speed	rpm	23,000
Design mass flow rate	kg/s	0.833
Design pressure ratio	-	1.68
Impeller tip diameter	mm	250
Impeller tip blade height	mm	8.21
Inducer hub diameter	mm	56.3
Inducer diameter	mm	116.72

Table 4.6: Compressor parameters

2. Modular ducting system: Figures 4.1 and 4.9 illustrate the modular ducting system. This system allows the change of the plenum volume, which in turn

allows flexibility in controlling the compression system behavior. The ducting system design parameters are summarized in Table 4.7.

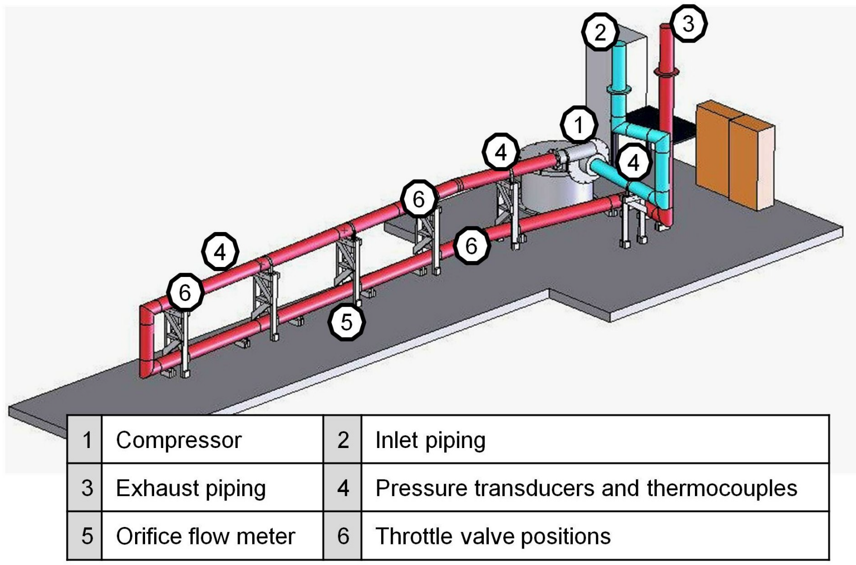

Figure 4.9: Test rig layout

Parameter	Unit	Value
Piping diameter	m	0.203
Inlet piping length	m	5.2
Exhaust piping length	m	21.3
Plenum volume #1	m^3	0.07
Plenum volume #2	m^3	0.23
Plenum volume #3	m^3	0.49

Table 4.7: Ducting system parameters

3. Throttle valve: Along the pipeline, the throttle valve is installed (with three possible locations as shown in Figure 4.9) to control the steady state flow rate. Changes in the flow rate will change the volume in the plenum. These throttle valves are common commercially available butterfly type valves.

Pressure transducers, thermocouples, and orifice flow meters are installed in the compression system in order to measure the pressure, temperature, and mass flow rate respectively. The location of these sensors can be found in Figure 4.9. These measurements will be used to generate the compressor characteristic curve as well as to provide information for the surge controller. Additionally, the compressor is driven by an induction motor with the output power of 125 kW at the maximum speed of 29,680 rpm. Due to the high power density of the motor, a cooling system is required when operating continuously at high speeds. Therefore, a chiller is installed to circulate the refrigerant fluid in the cooling system of the motor. In addition, rotor suspension and surge control algorithms are implemented by the computer operating on a real-time RTLinux operating system, with a sampling rate of 5kHz. Input signals to the control computer include rotor position measurements from sensors and the plenum pressure rise measurement, which are sampled at the same time interval. The temperature and flow measurements are collected by the Labview data acquisition system, which is used to operate the motor drive and throttle valve as well. For the user's safety, these two computers can be controlled remotely from a control room separated from the compressor test rig. The layout drawing of the control/data-acquisition system is illustrated in Figure 4.10.

4.3.2 Compression system modeling

To design the surge controller, a model that describes the flow instabilities in the compression system is required. The well-known one-dimensional compression model was derived by Greitzer in [35]. Greitzer's model describes the flow of fluid through the compressor, the plenum volume, and the throttle valve as shown in Figure 4.11. The non-dimensional states of the compression system are the compressor mass flow rate Φ_{c}, the compressor pressure rise Ψ_{c}, the plenum pressure rise Ψ_{p}, and the throttle mass flow rate Φ_{th}.

In [61], the effect of the impeller tip clearance was studied and the non-dimensional compressor pressure rise was derived as a function of the non-dimensional steady-

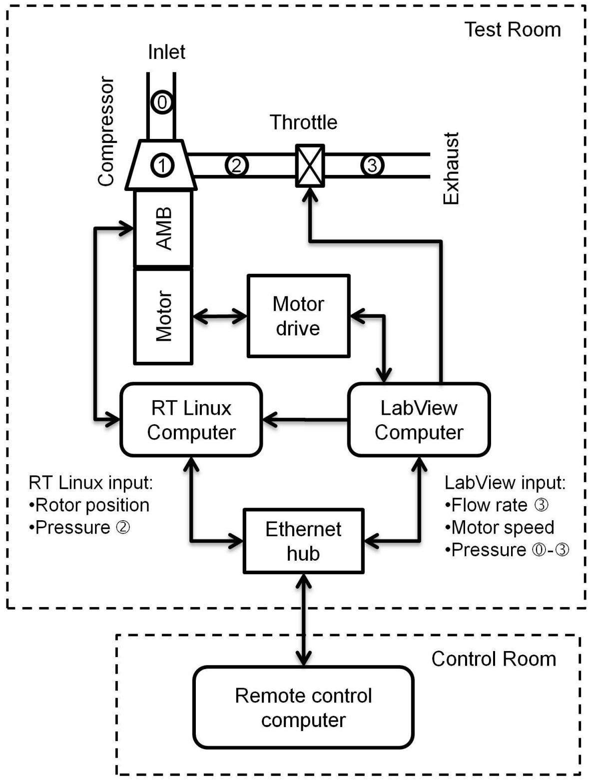

Figure 4.10: Layout of the control/data-acquisitions system of the test rig [73]

state compressor pressure and the variation of the impeller tip clearance. However, Greitzer's compression model does not capture the effect of the pipeline, which might cause additional resonances in the system characteristics. Therefore, an enhanced model of the compression system which includes the pipeline dynamics of this test rig was derived in [73]. The block diagram of the compression system model with the pipeline dynamics at the plenum output is illustrated in Figure 4.12.

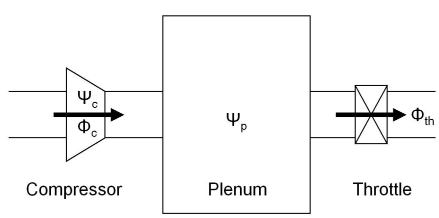

Figure 4.11: Compression system described by Greitzer's compression system model

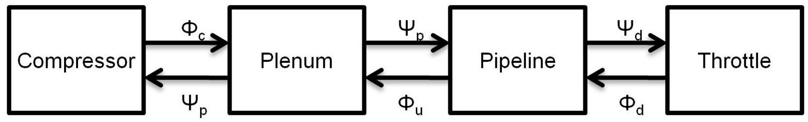

Figure 4.12: Block diagram of the compression system model with the pipeline dynamics at the plenum output

The overall compression system equations are assembled as

$$\dot{\Phi}_{\mathrm{c}} = B\omega_{\mathrm{H}}\left(A_1\Phi_{\mathrm{c}}^3 + B_1\Phi_{\mathrm{c}}^2 + D_1 + \frac{p_{\mathrm{o}1}}{\frac{1}{2}\rho_{\mathrm{o}1}U^2}k_{cl}\delta_{cl} - \Psi_{\mathrm{p}}\right), \tag{4.5a}$$

$$\dot{\Psi}_{\mathrm{p}} = \frac{\omega_{\mathrm{H}}}{B}\left(\Phi_{\mathrm{c}} - \Phi_{\mathrm{p}}\right), \tag{4.5b}$$

$$\dot{\Psi}_{\mathrm{th}} = \frac{2A_{12}A_{\mathrm{c}}}{\rho_{\mathrm{u}}U}\Phi_{\mathrm{p}} + \frac{2B_{12}A_{\mathrm{c}}}{\rho_{\mathrm{u}}U}u_{\mathrm{th}}c_{\mathrm{th}}\sqrt{\Psi_{\mathrm{th}}}, \tag{4.5c}$$

$$\dot{\Phi}_{\mathrm{p}} = \frac{A_{21}\rho_{\mathrm{u}}U}{2A_{\mathrm{c}}}\Psi_{\mathrm{th}} + A_{22}\Phi_{\mathrm{p}} + \frac{B_{21}\rho_{\mathrm{u}}U}{2A_{\mathrm{c}}}\Psi_{\mathrm{th}} + B_{22}u_{\mathrm{th}}c_{\mathrm{th}}\sqrt{\Psi_{\mathrm{th}}} + \frac{\rho_{\mathrm{u}}p_{\mathrm{o}1}}{\rho_{\mathrm{o}1}UA_{\mathrm{c}}}(A_{21} + B_{21}), \tag{4.5d}$$

where Eqs. (4.5a) and (4.5b) describe the compressor dynamics with the linearized impeller tip clearance effect, and Eqs. (4.5c) and (4.5d) represent the pipeline dynamics. For the complete derivation of each component's dynamics in the compression system, see reference [73]. All relevant parameters that appear in the overall compression system equations can be found in Table 4.8. In addition, the characteristic curve coefficients, A_1, B_1, and D_1, of the unstable region were obtained by the third-order polynomial fitting of the measured steady-state compressor flow when the rotor was spinning at 16,290 rpm as shown in Figure 4.13.

To design a linear controller to stabilize the compression system in a surge condition, the compression system dynamics in Eqs. (4.5a) - (4.5d) are linearized at an equilibrium operating point (Φ_{eq}, Ψ_{eq}). The new states ξ_1, ξ_2, ξ_3, and ξ_4 of the compression system that represent the variation of the original state variables from the corresponding equilibrium point are defined as

Parameter	Symbol	Unit	Value
Comp. duct length	L_c	m	1.86
Comp. duct cross. area	A_c	m^2	0.0082
Corrected A_1 coeff	A_1	-	-172.6
Corrected B_1 coeff	B_1	-	36.88
Corrected D_1 coeff	D_1	-	1.029
Design tip clearance	cl_n	mm	0.6
Greitzer stab. parameter	B	-	0.44
Helmholtz freq.	ω_H	rad/s	80.1
Impeller tip speed	U	m/s	213.24
Impeller blade height	b_2	mm	8.21
Inlet pressure	p_{o1}	Pa	101,325
Inlet gas density	ρ_{o1}	kg/m^3	1.165
Line dissipation number	d	-	2.83×10^{-5}
Line impedance constant	Z	Pa s/m	4.39×10^4
Plenum volume	V_p	m^3	0.049
Pipeline length	L	m	6.5
Throttle constant	c_{th}	-	1.7197

Table 4.8: Compression system model parameters

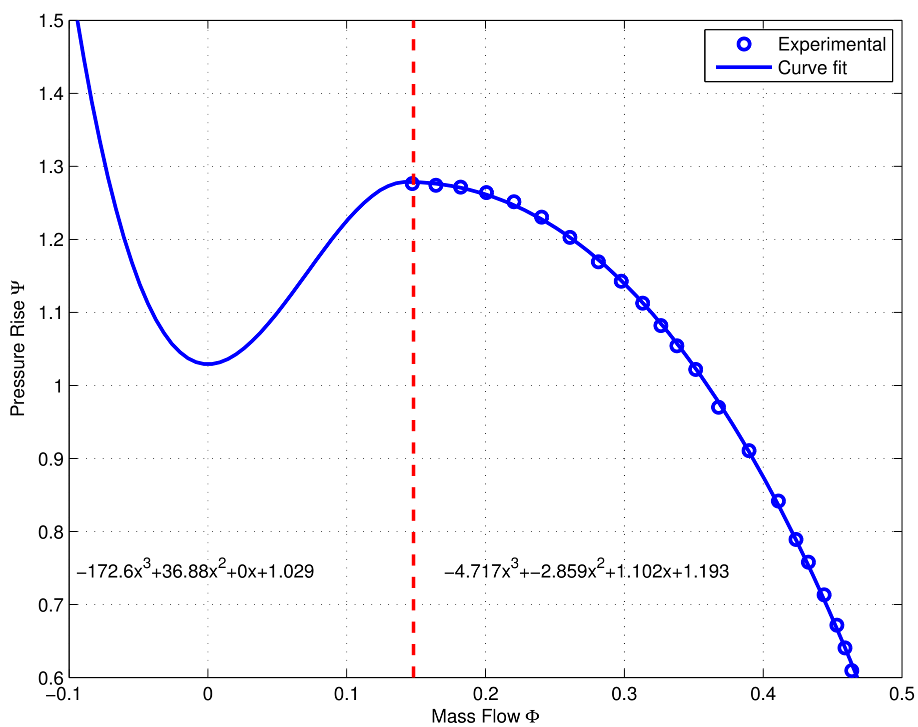

Figure 4.13: Fitted characteristic curve at 16,290 rpm [73]

$$\xi_1 = \Phi_\mathrm{c} - \Phi_\mathrm{eq}, \tag{4.6a}$$

$$\xi_2 = \Psi_\mathrm{p} - \Psi_\mathrm{eq}, \tag{4.6b}$$

$$\xi_3 = \Psi_\mathrm{th} - \Psi_\mathrm{eq}, \tag{4.6c}$$

$$\xi_4 = \Phi_\mathrm{p} - \Phi_\mathrm{eq}. \tag{4.6d}$$

By taking the derivatives of the new states in Eqs. (4.6a) - (4.6d), and applying a Taylor series expansion and ignoring the second order and higher order terms, the linear approximation of the compression system dynamics around the equilibrium operating point (Φ_eq, Ψ_eq) can be obtained. The linearized system equations are written in the state space form as

$$\dot{\xi} = \mathbf{A}\xi + \mathbf{B}\delta_\mathrm{cl}, \tag{4.7a}$$

$$y = C\xi, \tag{4.7b}$$

where

$$\xi = \begin{bmatrix} \xi_1 \\ \xi_2 \\ \xi_3 \\ \xi_4 \end{bmatrix}, \mathbf{A} = \begin{bmatrix} B\omega_\mathrm{H}\left(3A_1\Phi_\mathrm{eq}^2 + 2B_1\Phi_\mathrm{eq}\right) & -B\omega_\mathrm{H} & 0 & 0 \\ \frac{\omega_\mathrm{H}}{B} & 0 & 0 & -\frac{\omega_\mathrm{H}}{B} \\ 0 & 0 & \frac{B_{12}A_\mathrm{c}u_\mathrm{th,eq}c_\mathrm{th}}{\rho_\mathrm{u}U\sqrt{\Psi_\mathrm{eq}}} & \frac{2A_{12}A_\mathrm{c}}{\rho_\mathrm{u}U} \\ 0 & \frac{B_{21}\rho_\mathrm{u}U}{2A_\mathrm{c}}\Psi_\mathrm{th} & \frac{A_{21}\rho_\mathrm{u}U}{2A_\mathrm{c}}\Psi_\mathrm{th} + \frac{B_{22}u_\mathrm{th}c_\mathrm{th}}{2\sqrt{\Psi_\mathrm{eq}}} & A_{22} \end{bmatrix},$$

$$\mathbf{B} = \begin{bmatrix} 2\frac{B_{\omega_\mathrm{H}}p_\mathrm{o1}k_{cl}}{\rho_\mathrm{o1}U^2} \\ 0 \\ 0 \\ 0 \end{bmatrix}, \mathbf{C} = [1\ 1\ 0\ 0].$$

According to the linearized compression system in Eqs. (4.7a) and (4.7b), the system input is the impeller tip clearance δ_cl and the two outputs are the compressor mass flow rate ξ_1 and the plenum pressure rise ξ_2. For the throttle valve opening value $u_{\mathrm{th,eq}}$ greater than 0.185, the compression system remains stable in the neighborhood of the equilibrium operating point. In order to capture the instability dynamics during a surge condition, the equilibrium value of the throttle valve opening $u_{\mathrm{th,eq}}$ was chosen to be 0.17 for linearization. For the compression system model linearized at $u_{\mathrm{th,eq}} = 0.17$, the frequency responses from the impeller tip clearance δ_{cl} to two outputs, ξ_1 and ξ_2, are shown in Figure 4.14. From the Bode plots, it can be noticed that there are two resonances that occur at around 7 Hz and 21 Hz, which correspond to the frequencies of the surge limit cycle and the acoustic resonance of piping.

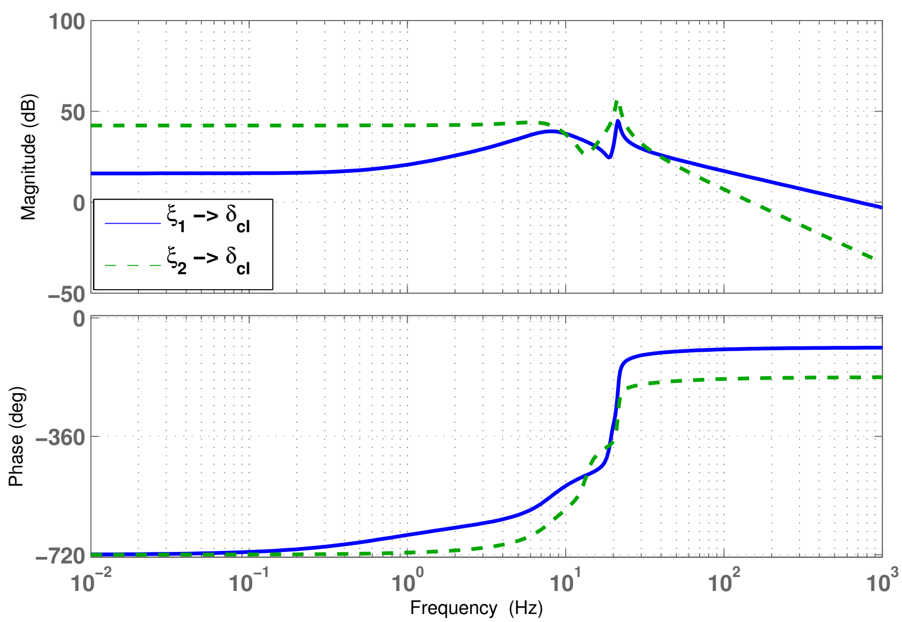

Figure 4.14: Bode plots of the linearized compression system

For the surge controller implementation, the information of the mass flow rate and the plenum pressure rise are required. However, the orifice flow meter installed in the system as described earlier in this section provides only the steady-state flow. For the feedback control operation, transient flow rate measurement is required. Therefore, a mass flow rate observer needs to be designed to provide the transient flow rate information. In [73], the observer was derived based on the system state equations given in Eq. (4.5a) - (4.5d). The mass flow rate observer state equations are given as follows,

$$\dot{z} = B\omega_{\mathrm{H}}\left(\hat{\Psi}_{\mathrm{c,ss}} + \frac{p_{\mathrm{o1}}}{\frac{1}{2}\rho_{\mathrm{o1}}U^2}k_{cl}\delta_{cl} - \Psi_{\mathrm{p}} - c\hat{\Phi}_{\mathrm{c}} + c\Phi_{\mathrm{p}}\right), \tag{4.8a}$$

$$\dot{\Psi}_{\mathrm{th}} = \frac{2A_{12}A_{\mathrm{c}}}{\rho_{\mathrm{u}}U}\Phi_{\mathrm{p}} + \frac{2B_{12}A_{\mathrm{c}}}{\rho_{\mathrm{u}}U}u_{\mathrm{th}}c_{\mathrm{th}}\sqrt{\Psi_{\mathrm{th}}}, \tag{4.8b}$$

$$\hat{\Phi}_{\mathrm{c}} = z + B^2c\Psi_{\mathrm{p}}, \tag{4.8c}$$

$$\dot{\Phi}_{\mathrm{p}} = \frac{A_{21}\rho_{\mathrm{u}}U}{2A_{\mathrm{c}}}\Psi_{\mathrm{th}} + A_{22}\Phi_{\mathrm{p}} + \frac{B_{21}\rho_{\mathrm{u}}U}{2A_{\mathrm{c}}}\Psi_{\mathrm{th}} + B_{22}u_{\mathrm{th}}c_{\mathrm{th}}\sqrt{\Psi_{\mathrm{th}}} + \frac{\rho_{\mathrm{u}}p_{\mathrm{o1}}}{\rho_{\mathrm{o1}}UA_{\mathrm{c}}}(A_{21} + B_{21}), \tag{4.8d}$$

where $\hat{\Phi}_{\mathrm{c}}$ is the estimated mass flow rate and $\hat{\Psi}_{\mathrm{c,ss}}$ is the observed non-dimensional steady-state compressor pressure rise, which can be obtained from the characteristic curve illustrated in Figure 4.13, and $c = 5$.

Chapter 5

Fractional Order Control of Rotor Suspension

In this chapter, the design of the fractional order PID controller for the lateral and axial rotor dynamics explained in Chapter 4 is presented. First, the control design specifications for the rotor suspension are formulated based on the industrial standards. Then, the design process of the FOPID controller for rotor suspension is explained, including the considerations between decentralized and centralized control methods, the FOPID controller tuning methods, and approximation of the fractional order terms. Lastly, the simulation and experimental results of the designed FOPID controller are presented. These results are compared with the LQG controller from the previous work [73] as well as the PID controller that is designed based on the same specifications and tuning methods as the FOPID controller.

5.1 Control design specifications

A commonly used rotor-dynamic specifications of AMB systems are developed by American Petroleum Institute (API) and International Organization for Standardization (ISO). The specifications are developed based on the API 617 [5], which is for centrifugal compressors equipped with traditional rolling element or fluid-film bearings. Since the clearance available in the AMB system is larger than the clearance in machines equipped with traditional rolling element or fluid-film bearings, the standard includes a section on machines equipped with magnetic bearings. This additional section states that the maximum vibration must be lower than 30% of the minimum clearance $C_{\min}$. In AMB systems, $C_{\min}$ usually refers to the clearance relative to the center of auxiliary bearing. Moreover, the forced response analysis with different locations of unbalance mass placement is also used for AMB systems. Unbalance values and locations for different modes are illustrated in Figure 5.1. This analysis is used to predict the amount of vibration when each mode is excited according to the placement of unbalance values. Unbalance values and locations for different modes are illustrated in Figure 5.1, where U is the unbalance force, N is the maximum continuous operating speed (rpm), and W is the static journal load (kg).

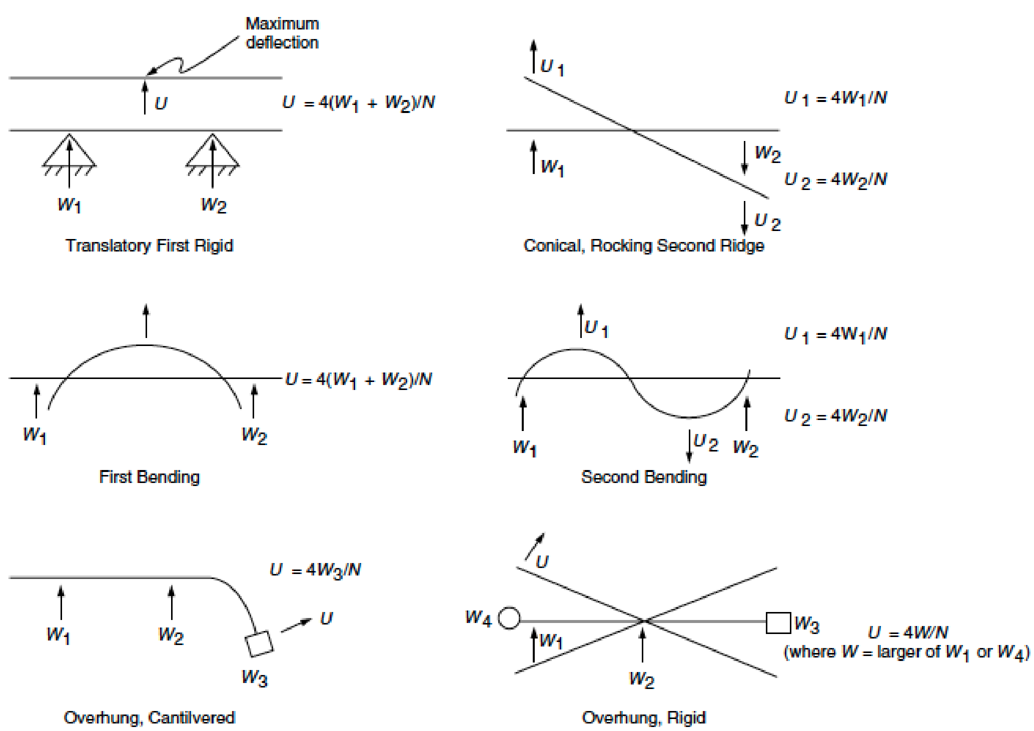

Figure 5.1: Unbalance values and locations as specified in API 617 [5]

Another set of widely used specifications for AMB systems is stated in ISO 14839. This standard is used as a recommended specification instead of as a requirement. Vibration level and stability margin are the two specifications recommended in ISO 14839. The stability margin is determined by the peak value of sensitivity function. This margin implies how sensitive the system response is to variations in the system. As illustrated in Figure 5.2, the sensitivity function is defined as the transfer function either from *disturbance* D_1 *to controller input* ($D_1 \rightarrow V_1$) or from *disturbance* D_2 *to plant input* ($D_2 \rightarrow U_2$). The specifications categorize the system into Zone A through D depending on the maximum displacement and peak value of the sensitivity function as summarized in Table 5.1. At the present, ISO 14839 is merged in as one of the sections in API 617 [5].

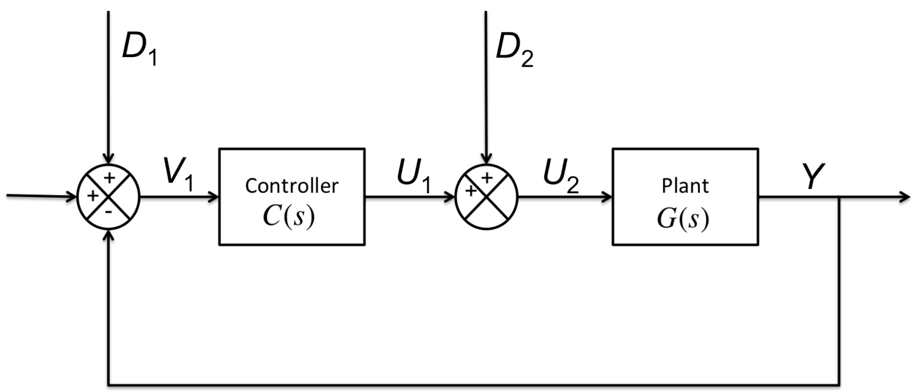

Figure 5.2: Closed-loop system block diagram with disturbances

Zone limit	Maximum displacement	Peak Sensitivity
A/B	$< 0.3C_{\min}$	< 3 (9.5 dB)
B/C	$< 0.4C_{\min}$	< 4 (12 dB)
C/D	$< 0.5C_{\min}$	< 5 (14 dB)

Table 5.1: Recommended criteria of zone limits in ISO 14839 [39, 40]

The definitions of each zone are described as follows.

Zone A: newly commissioned machines normally fall into this zone

Zone B: acceptable for unrestricted long-term operation

Zone C: unsatisfactory for long-term continuous operation

Zone D: sufficiently severe to cause damage to the machine

Another control design specification that is used widely in most control system designs is the transient response performance. These performance parameters show how smooth the operation could be in case there are external disturbances. Typically a unit step response test is performed to demonstrate this specification. The performances considered in the step test are rise time, settling time, and overshoot.

5.2 Design and experimental test of FOPID controller for rotor lateral dynamics

5.2.1 Design of FOPID controller

The FOPID controller for the rotor lateral dynamics takes the form of

$$C_{\mathrm{FOPID}}(s) = K_{\mathrm{P}} + \frac{K_{\mathrm{I}}}{s^{\lambda}} + K_{\mathrm{D}} s^{\mu}. \tag{5.1}$$

This controller is also coupled with a second order low-pass filter in order to limit the bandwidth as well as to make the controller realizable for implementation. Here it is assumed that the two control axes (x and y) are symmetric. Therefore, the controllers used for both control axes will be identical.

As mentioned in Section 2.3, both decentralized and centralized control methods are used for AMB control systems. Therefore both methods will be used to design FOPID controllers for rotor lateral dynamics in order to determine the better design for implementation. The structure of the decentralized and centralized control methods are illustrated in Figures 5.3 and 5.4, respectively. For the decentralized method, only diagonal terms of a plant model are used with the assumption that the off-diagonal terms have a small coupling effect. On the other hand, the centralized method decouples the inputs and outputs of the AMB system into rigid tilt and translate modes of the rotor. The transformation of the sensor measurements to the modal coordinate is given by the difference of the two sensor signals for the tilting mode, and the addition of the signals for the translate mode [74]. The transformation of the original plant $G(s)$ to the centralized coordinate is given by

$$G_c(s) = H(s)G(s)H^{-1}(s), \tag{5.2}$$

where

$$H = \begin{bmatrix} 1 & -1 \\ 1 & 1 \end{bmatrix}.$$

Two independent controllers are designed for the two decoupled systems. After two centralized controllers, C_{11} and C_{22}, are derived, they must be transformed back to the original physical coordinates by

$$C(s) = H^{-1} \begin{bmatrix} C_{11} & 0 \\ 0 & C_{22} \end{bmatrix} H. \tag{5.3}$$

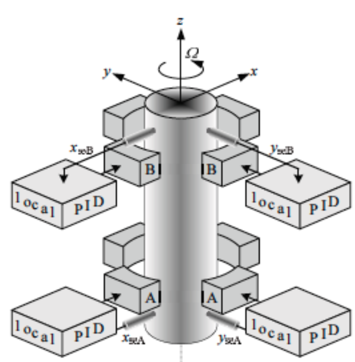

Figure 5.3: Structure of the decentralized control method [63]

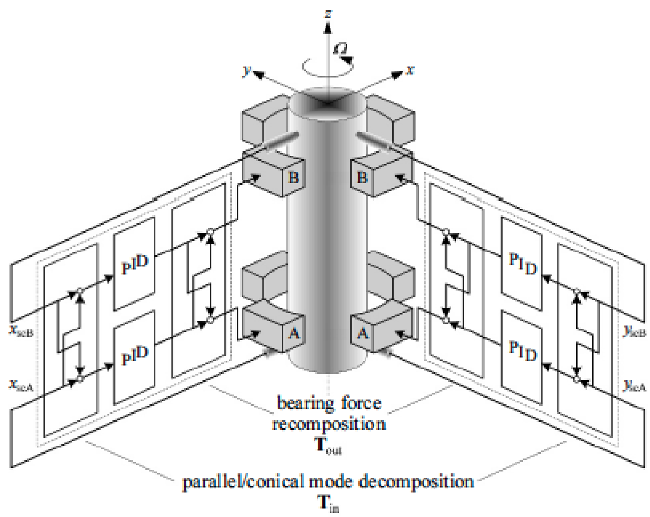

Figure 5.4: Structure of the centralized control method [63]

In addition, these two designs are tuned using the Genetic Algorithm (GA). Two additional tuning methods, namely Differential Evolution (DE) and Particle Swarm Optimization (PSO), will be used in the FOPID controller design after determining preferability between the decentralized and centralized control methods. The first step in the tuning process is to specify the objective functions. As previously mentioned, vibration level and stability margin are the two main specifications. Furthermore, the step response performance objective is also important to include in order to provide smooth rotation during the transition between rotational speeds and an ability to reject disturbances. Thus, the objective functions used for the control of the rotor lateral dynamics are listed below.

1. Stability of closed-loop system (J_1): Closed-loop stability will be determined by the number of poles that have a positive real part. The optimization goal of this objective is zero.

2. Stability margin (J_2): A peak magnitude of the sensitivity function as described in Chapter 3 will be used to determine a stability margin.

3. Vibration level (J_3): A maximum magnitude of forced responses among three cases (translate mode, conical mode, and overhung cantilevered) as illustrated in Figure 5.1. This objective will be used to determine the maximum vibration.

4. Integral square error (ISE) of a unit step response (J_4): Instead of specifying transient response performance separately, the performance index ISE will be used in order to reduce conflict between different performances.

All objective functions will be combined as a single cost function J during the optimization process. Therefore, it is proper to add some constant weights, w_i, for each specified objective so that all weighted objectives are normalized,

$$J = \max\{w_1 J_1, w_2 J_2, w_3 J_3, w_4 J_4\}.$$

These constant weights are the inverse of the desired values of each specification. For example, the desired value of peak sensitivity must be less than 3 according to ISO specification, thus the initial value of w_2 is 1/3.

Next, the parameter values of the GA optimization must be initialized. These values include the size of the population, the initial population values, the crossover rate, and the mutation rate. The selected size of the population reflects the total tested solutions for each generation. A larger population can lead to better minimization results, but the computation will be longer. For this study, the population size is chosen to be 200. The initial population consists of the gains and orders of the FOPID controller. These initial values were obtained from the manual tuning of the conventional PID controller for the system, which means that the initial derivative and integral orders are set to 1. The closed-loop system is stable with these initial values, which can reduce the load on the stability objective during the optimization process. The value of the crossover rate is 0.8 and the uniform mutation rate is 0.01. After 50 generations, the optimization is completed. The whole process will be repeated with the new initial populations based on the solution from the previous iteration. There may be slight changes in lower and upper bounds of the tuning parameters as well. Normally, after 3 to 5 iterations, the improvement of the solution will be very small.

Note that the main difference of this study from the existing works in the field is that the approximation of the fractional order operators, s^λ and s^μ, occur during the tuning process. Studies in the past generally have addressed the approximation step after the optimization is completed, which can degrade the performance of the FOPID controller due to errors from the approximation. Therefore, in this study, the approximation is included in the optimization process and uses the approximated FOPID controller to evaluate all objective functions. Oustaloup's method is used for the fractional order approximation as explained in Chapter 3 and the chosen number of poles and zeros used for the approximation is 2.

The performance of the designed decentralized and centralized FOPID controllers is summarized in Table 5.2 and the Bode plots of the sensitivity functions of both FOPID controllers are illustrated in Figure 5.5. Clearly, the peak value of the sensitivity function and the maximum vibration of the centralized FOPID controller are smaller than that of the decentralized FOPID controller, while the transient responses of the two controllers are similar. From these results, it is evident that the centralized FOPID controller outperforms the decentralized FOPID controller. Therefore, the centralized FOPID controller will be used for the rest of the designs for lateral rotor dynamics.

For the next design, the centralized FOPID controller will be designed based on two additional tuning methods. First the DE tuning method is employed in the design process. As described in Chapter 3, parameters needed for the optimization process are similar to the GA algorithm except for the weight factor F for the mutation process, which is set to be 0.85 in this study. Otherwise, the size of population, the number of maximum iterations, and the crossover rate remain the same as in the GA

Specifications	Decentralized	Centralized
Sensitivity function peak	2.8839	2.4414
Peak unbalance vibration (mm)	0.0032	0.0029
Controller output peak (V)	0.3341	0.3909
Overshoot (%)	4.2894	6.1020
Rise time (s)	0.0094	0.0077
Settling time (s)	0.0425	0.0205

Table 5.2: Comparison of performances between decentralized and centralized FOPID controllers

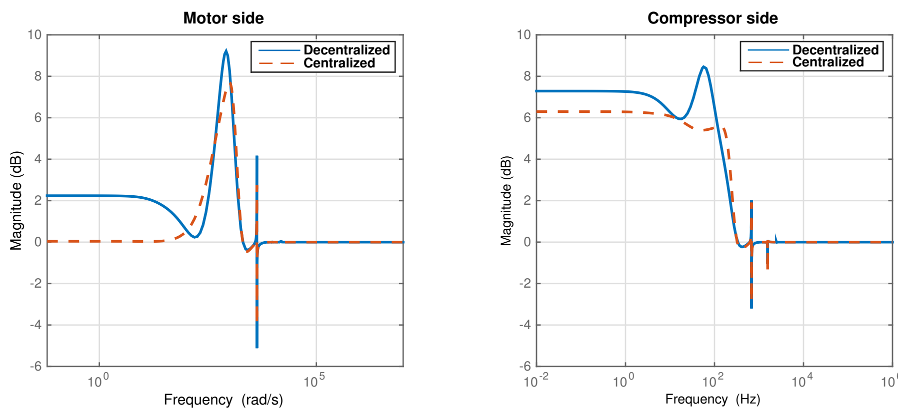

Figure 5.5: Bode plots of sensitivity function of the decentralized and the centralized control methods

optimization case. Second, the FOPID controller parameters are tuned by the PSO tuning method. The size of the population and the maximum iterations are the same as in the two previous methods. The acceleration factors c_1 and c_2 are set to be 0.5 and 1.25, respectively. The value of c_2 is set to be greater than c_1 so as to assign heavier weight to the acceleration rate for the global best solution in each generation.

The performance of the FOPID controllers tuned by the GA, DE, and PSO methods are summarized in Table 5.3 and the Bode plots of the sensitivity functions of both FOPID controllers are illustrated in Figure 5.6. It can be observed that the FOPID controller tuned by the DE algorithm gives better results in terms of the peak of the sensitivity function and maximum vibration levels. In addition, the corresponding

FOPID controller has a good transient response for a smooth rotation. Therefore, this FOPID controller will be used for implementation as well as for comparison with other kinds of controllers.

Specifications	GA	PSO	DE
Sensitivity function peak	2.4414	2.3947	2.2727
Peak unbalance vibration (mm)	0.0029	0.0027	0.0024
Controller output peak (V)	0.3909	0.3639	0.4176
Overshoot (%)	6.1020	5.7632	2.7300
Rise time (s)	0.0077	0.0077	0.0071
Settling time (s)	0.0205	0.0161	0.0151

Table 5.3: Comparison of performances of FOPID controllers tuned by different Evolutionary algorithms

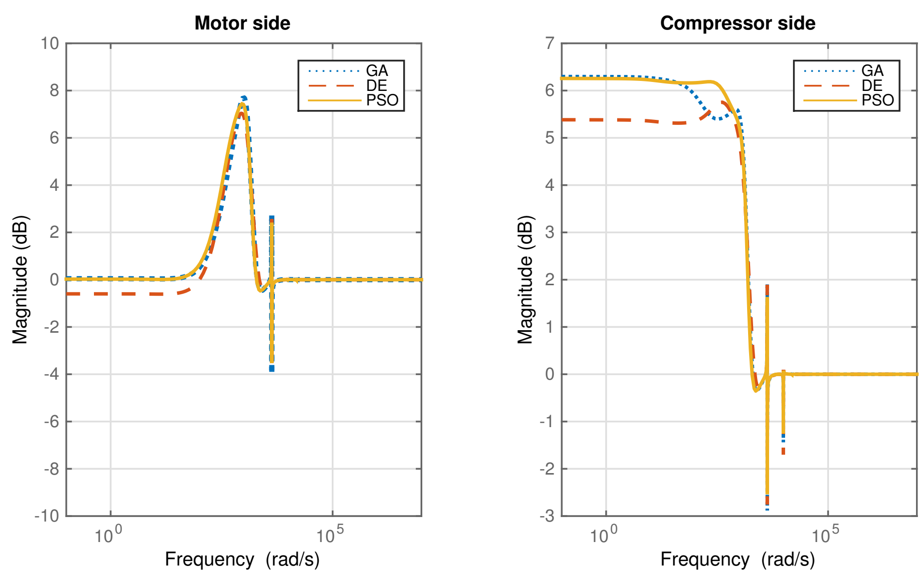

Figure 5.6: Magnitude plots of the sensitivity functions of FOPID controllers with different tuning algorithms

To emphasize the best case of the centralized FOPID controller design, Table 5.4 summarizes the values of the FOPID controller parameters obtained from DE optimization. The vibration level and stability margin results are illustrated in Figures 5.7 and 5.8, respectively. The vibration level is well below 30% of the minimum clearance. The peak of the sensitivity function over the rotational speed range is below a magnitude of 3. This shows the Zone A specification as recommended by ISO 14839 is satisfied by the FOPID controller.

Bearing	K_{P}	K_{I}	K_{D}	λ	μ
Motor side	0.1752	0.120	0.0011	0.752	0.942
Compressor side	0.1795	0.112	0.0010	0.834	0.902

Table 5.4: Parameters in the the FOPID controllers tuned by the DE algorithm

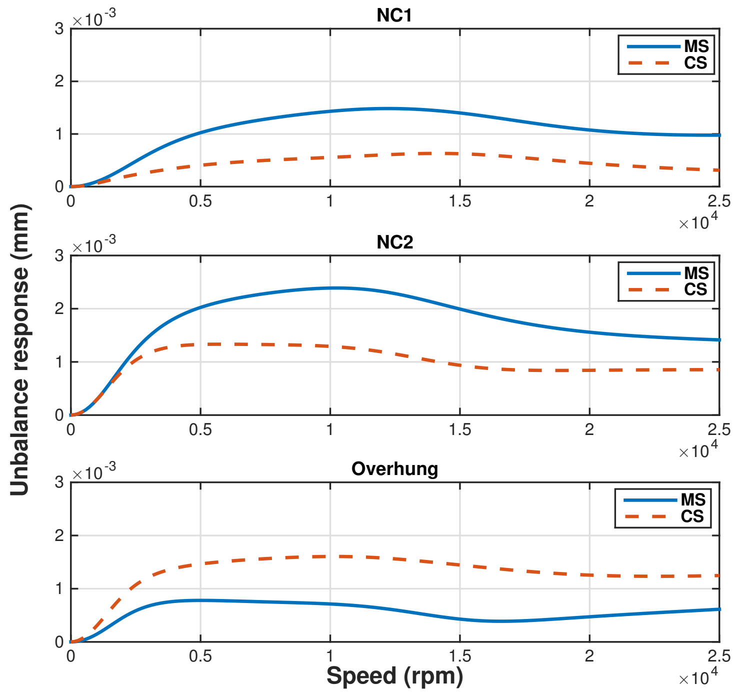

Figure 5.7: Forced response with unbalance mass placing for three excitation cases as specified in API 617 [5]

For comparison, the conventional PID controller is tuned based on the same objectives and algorithms as the best case of the FOPID controller. Moreover, performances based on the LQG controller that were designed for the same system reported in [73] are compared with both the FOPID and PID controllers in Table 5.5.

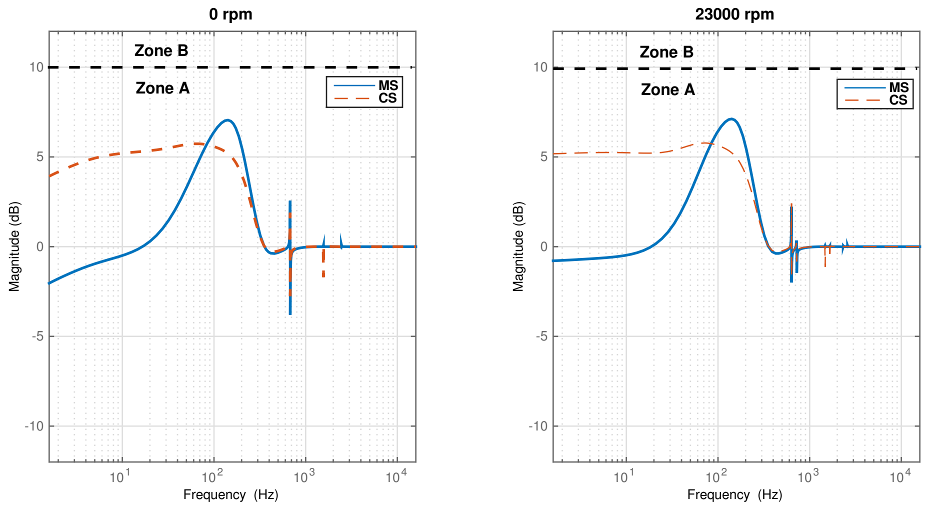

Figure 5.8: Magnitude plots of the sensitivity functions at zero and maximum continuous speed under the FOPID controllers tuned by the DE algorithm

Specifications	PID	FOPID	LQG
Sensitivity function peak	2.6742	2.2727	2.4794
Peak unbalance vibration (mm)	0.0037	0.0024	0.0026
Controller output peak (V)	0.4228	0.3340	0.1810
Overshoot (%)	0.172	0.033	0.178
Rise time (s)	0.003	0.003	0.005
Settling time (s)	0.023	0.042	0.016
Bandwidth (rad/s)	12757	13759	14377
Controller dimension as implemented	6	7	11

Table 5.5: Comparison of performances in radial AMBs

As shown in Table 5.5 and Figure 5.9, the stability margin of all controllers fall within Zone A specification (smaller than 3). Moreover, the sensitivity function peak of the FOPID controller is smaller than the value achieved by the PID and LQG controllers. Another advantage of the FOPID controller over the LQG controller is the reduction of the controller size by 50 percent. Transient response of each controller is approximately the same. Each controller has a bandwidth within the limit for digital implementation at a 5 kHz sampling frequency.

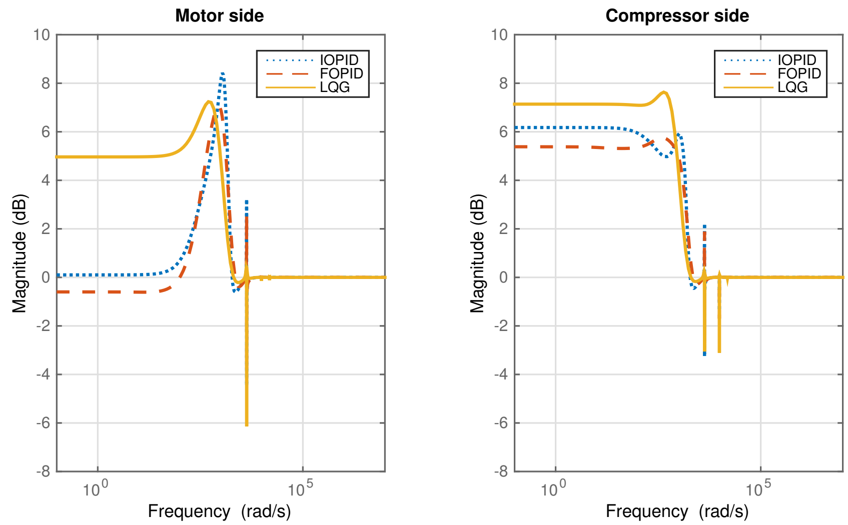

Figure 5.9: Bode plots of the lateral AMB sensitivity function at the motor side and compressor side under three different controllers

5.2.2 Experimental test of lateral rotor suspension

To validate the design of the FOPID controller for lateral rotor dynamics in the previous section, two types of measurements are made. The first type of measurement is the rotor vibration magnitude for speeds ranging from 500 rpm to 16,500 rpm, in 500 rpm increments. Three separate cases are tested including the IOPID and FOPID controllers tuned by the DE algorithm and the LQG controller that was previously designed in [73].

The results in Figures 5.10 and 5.11 show the rotor vibration within the specified speed range of the motor side and compressor side, respectively. The FOPID controller leads to the smallest vibration magnitude throughout the speed range among all three tested controllers and its peak magnitude is well within the limit of Zone A specified by ISO [39]. The IOPID controller leads to the largest vibration magnitude which can be observed from the motor side measurement. The result agrees with the prediction of the maximum vibration magnitudes tested in the forced response analysis.

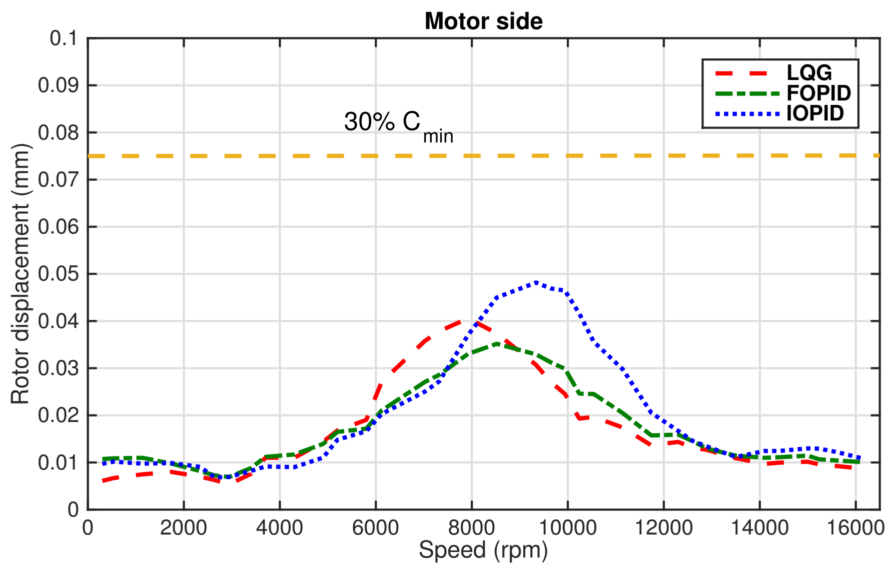

Figure 5.10: Rotor displacements at the motor side under the IOPID, FOPID, and LQG controllers

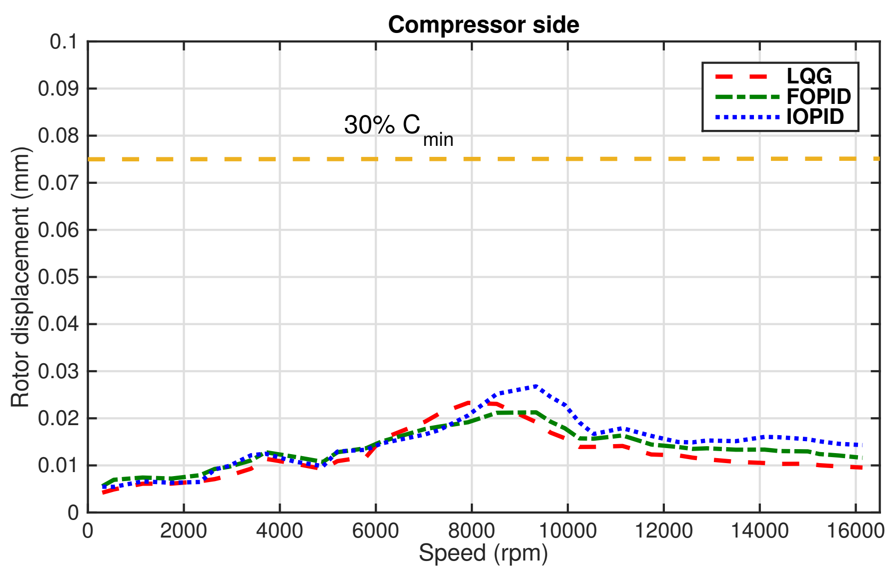

Figure 5.11: Rotor displacements at the compressor side under the IOPID, FOPID, and LQG controllers

The second test is the sensitivity function frequency response measurement. Again, the three controllers used in the rotor vibration experiment are tested. For this testing, the perturbation signal of 100 mv with frequencies ranging from 0.1 Hz to 1200 Hz is added at the controller input and the sensitivity function frequency response is obtained from the relationship between the sum of perturbation and controller input signals and the perturbation signal itself. The frequency response plots for the cases of all three controllers for both the motor side and the compressor side are shown in Figures 5.12 and 5.13, respectively. From these results, the sensitivity function peak under the FOPID controller is the smallest and falls into Zone A specification of the ISO standard [40], while the IOPID controller results in the largest sensitivity function peak and its magnitude falls into Zone B specification. Lastly, the trend of the sensitivity function frequency responses match the theoretical prediction in Figure 5.9.

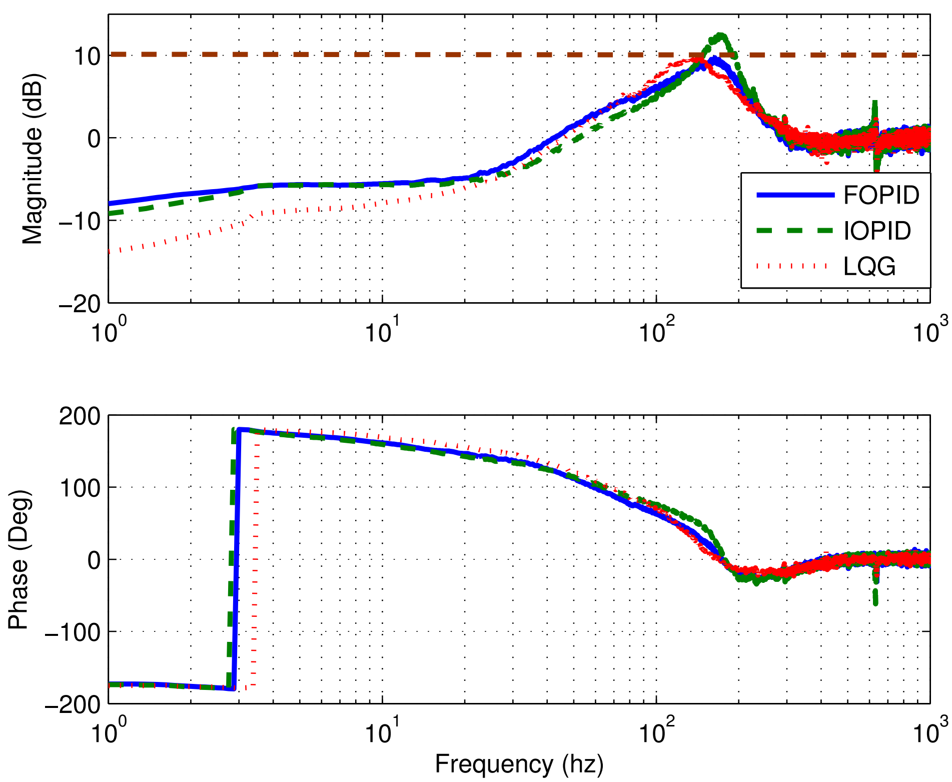

Figure 5.12: Bode plots of the lateral AMB sensitivity function at the motor side

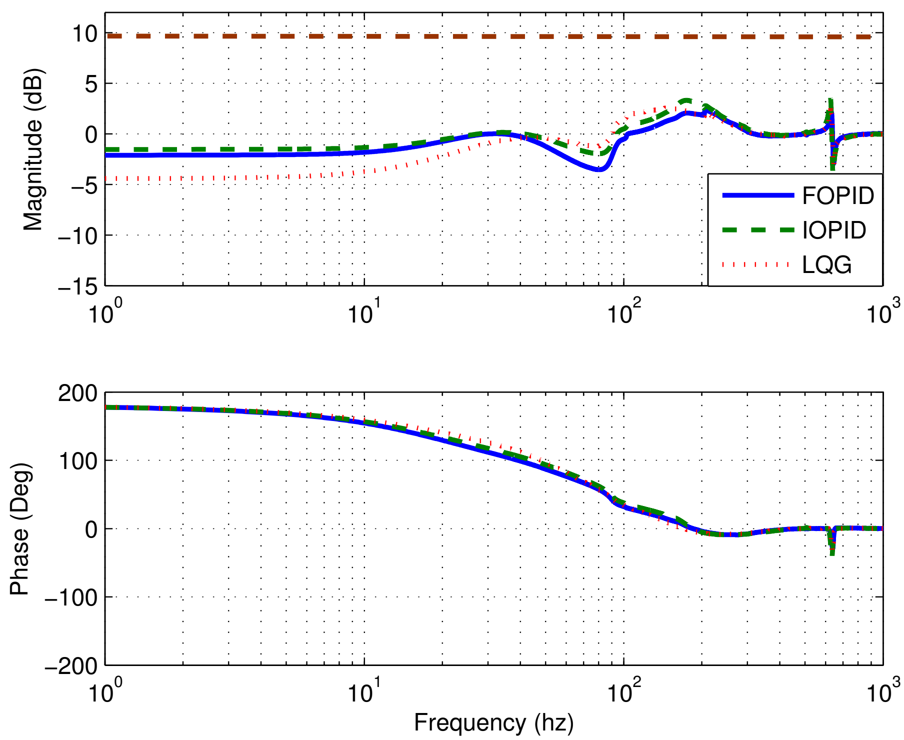

Figure 5.13: Bode plots of the lateral AMB sensitivity function at the compressor side

5.3 Design and experimental test of FOPID controller for rotor axial dynamics

5.3.1 Design of FOPID controller

The ultimate goal of the control design for the thrust AMB system is to achieve good rotor tracking performance at a low/mid frequency range. In addition, the closed-loop system should have a capability to reject external disturbances such as aerodynamic disturbances acting on the compressor impeller during surge. The designed controller with these capabilities must have a bandwidth within the range limited by the sampling frequency. The controller structure will have the same form as in the lateral dynamics design, where the FOPID controller is coupled with a second order low pass filter. The objective functions will be similar to the objectives defined for the H_∞ controller design for axial rotor support in [73]. The objective functions will combine the weighting functions with the sensitivity function S, the complementary sensitivity function T, the plant transfer function G, and the controller transfer function K, in order to specify the desired performance in the frequency domain. All these objective functions are listed below.

1. Stability of the closed-loop system (J_1): Closed-loop stability will be determined by the number of poles that have positive real part. The optimization goal of this objective is zero.

2. Tracking error performance: $J_2 = \|W_3 S W_2\|_\infty$.

3. Control effort according to the reference input signal: $J_3 = \|W_4 S K W_2\|_\infty$.

4. Transmission of the input disturbance to the control output: $J_4 = \|-W_3 S G W_1\|_\infty$.

5. Closed-loop dynamics from the reference input to the rotor position: $J_5 = \|-W_4 T W_1\|_\infty$,

where the weighting functions were defined in [73], which are based on the interconnected system shown in Figure 5.14, as follows.

$$\begin{aligned}
W_1(s) &= 0.07, \\
W_2(s) &= 1, \\
W_3(s) &= 100\frac{(0.0015s+1)}{(0.5s+1)}, \\
W_4(s) &= 0.01\frac{(10^{-3}s+1)^2}{(10^{-5}s+1)^2}.
\end{aligned}$$

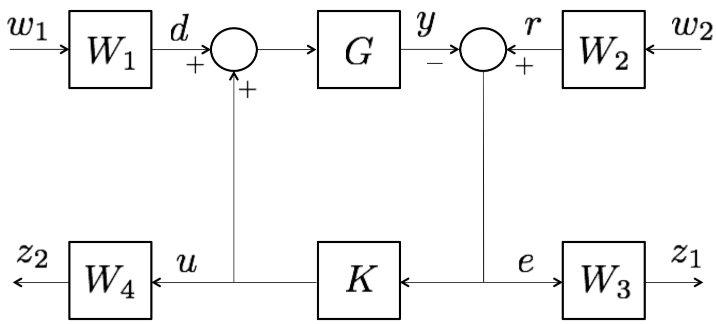

Figure 5.14: Interconnected system for the design of the thrust AMB rotor support controller

Similar to the previous design, all objective functions will be combined as a single cost function during the optimization process as follows,

$$J = \max\{J_1, J_2, J_3, J_4, J_5\}.$$

The optimization goal is to have the infinity norm of all objective functions smaller than 1. Once again, the three tuning methods used for the optimization are the GA, DE, and PSO methods. The size of the population for all cases is reduced to 100 since there are fewer tuned parameters than the control of rotor lateral dynamics. The crossover rate, the weight factor, the acceleration rate, and the mutation rate are kept the same as in the previous design. Table 5.6 shows the resulting infinity norm of the objective functions for all tuning methods. All tuning methods have similar optimization results. Yet, the DE algorithm achieves the lowest infinity norm. Thus, this design will be used for implementation.

Controller characteristics	GA	DE	PSO
Infinity norm of objective functions	1.061	1.034	1.035

Table 5.6: Comparison of the objective function peaks resulting from different tuning methods

Table 5.7 summarizes the values of the FOPID controller parameters obtained from the DE optimization. The resulting magnitude plots of all objectives, except the stability objective, are shown in Figure 5.15.

Bearing	K_P	K_I	K_D	λ	μ
Thrust AMB	0.0743	11.3933	0.00468	0.6249	0.9068

Table 5.7: The tuned FOPID controller parameters for rotor axial dynamics

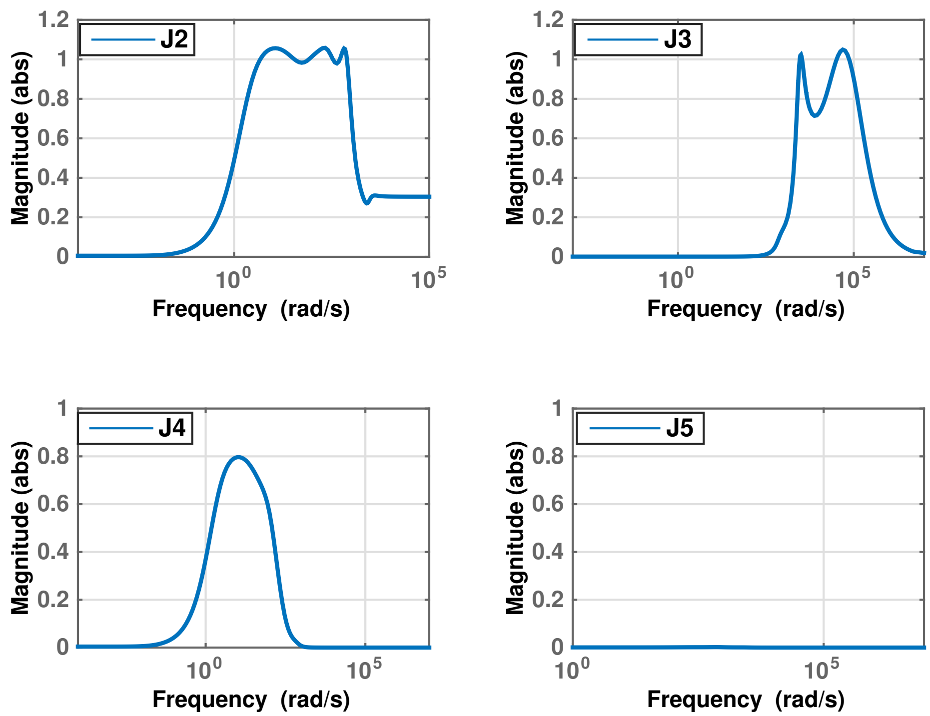

Figure 5.15: Magnitude of the objective functions under the FOPID controller

The sensitivity function in Figure 5.16 shows that the stability margin specification qualifies for Zone A, where a sensitivity peak is less than 3. Besides the peak of the sensitivity function, tracking error performance can also be observed from the magnitude of the complementary sensitivity function T, which represents the relationship between the reference input and the rotor position. Figure 5.16 shows that, at low/mid frequencies the magnitude of T is 1 and the phase is 360 deg (in phase). This implies that the rotor position follows the change of the input reference signal closely in that frequency range.

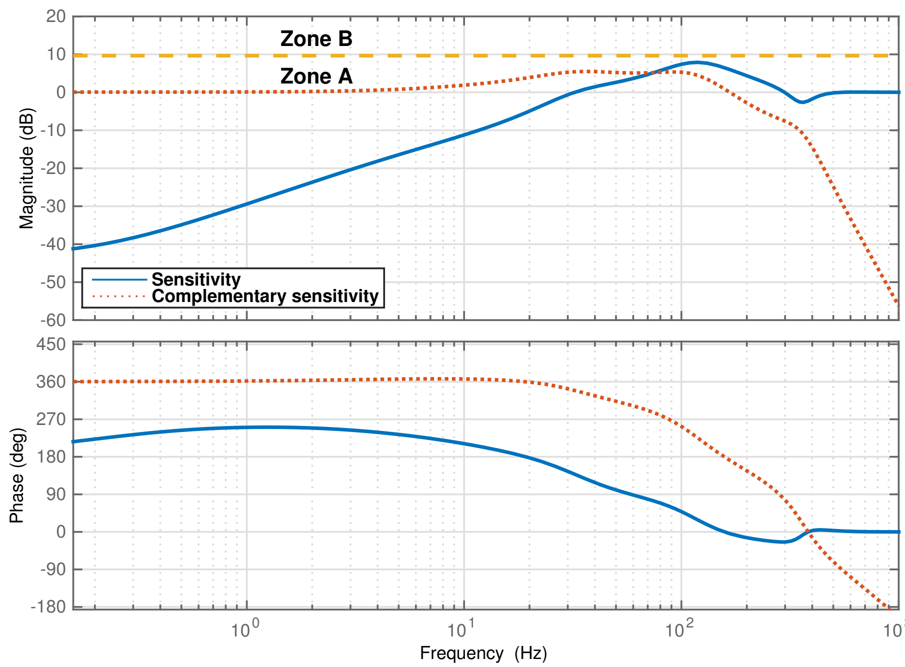

Figure 5.16: Bode plots of the thrust AMB sensitivity and complementary sensitivity functions under the FOPID controller tuned by the DE algorithm

For comparison, the conventional PID controller is tuned based on the same objectives and algorithms as the FOPID controller. Moreover, performance based on the H_∞ controller that was designed for the same system reported in [73] are compared with both the FOPID and the IOPID controllers in Table 5.8.

In Table 5.8, both the FOPID and the H_∞ controllers achieve a stability margin to satisfy the Zone A requirement. On the other hand, the stability margin falls into Zone B when using a PID controller as shown in Figure 5.17. Moreover, the sensitivity function peak under the FOPID controller is close to the value achieved by the H_∞

Specifications	IOPID	FOPID	H_∞
Sensitivity function peak	3.312	2.482	2.433
Infinity norm of objectives	1.380	1.034	0.907
Controller bandwidth (rad/s)	2045	2841	2754
Controller order as implemented	4	6	8

Table 5.8: Comparison of performances in the thrust AMB system

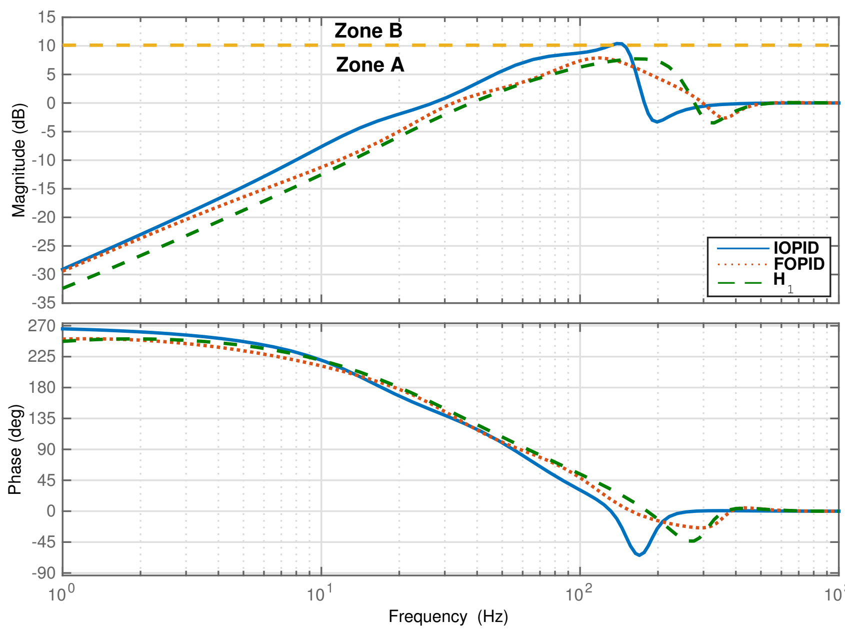

Figure 5.17: Bode plots of the thrust AMB sensitivity and complementary sensitivity functions

controller. The advantage of the FOPID controller over the H_∞ controller is that the dimension of the controller is reduced by 50 percent. Lastly, all controllers have a bandwidth within the limit for the digital implementation of 5 kHz sampling frequency.

5.3.2 Experimental test of axial rotor suspension

The sensitivity function frequency response measurement is conducted the same way as in the lateral rotor dynamics case. The frequency response plots of all three controllers are shown in Figures 5.18. From these results, the sensitivity function peak under the FOPID controller is the smallest and falls into Zone A specification of the ISO standard [40], while the IOPID controller has the largest sensitivity function peak and its magnitude falls into Zone B specification. The trend of the sensitivity function frequency responses matches the theoretical prediction in Figure 5.17. Figure 5.19 shows that the closed-loop bandwidth when using the FOPID controller matches the simulation result.

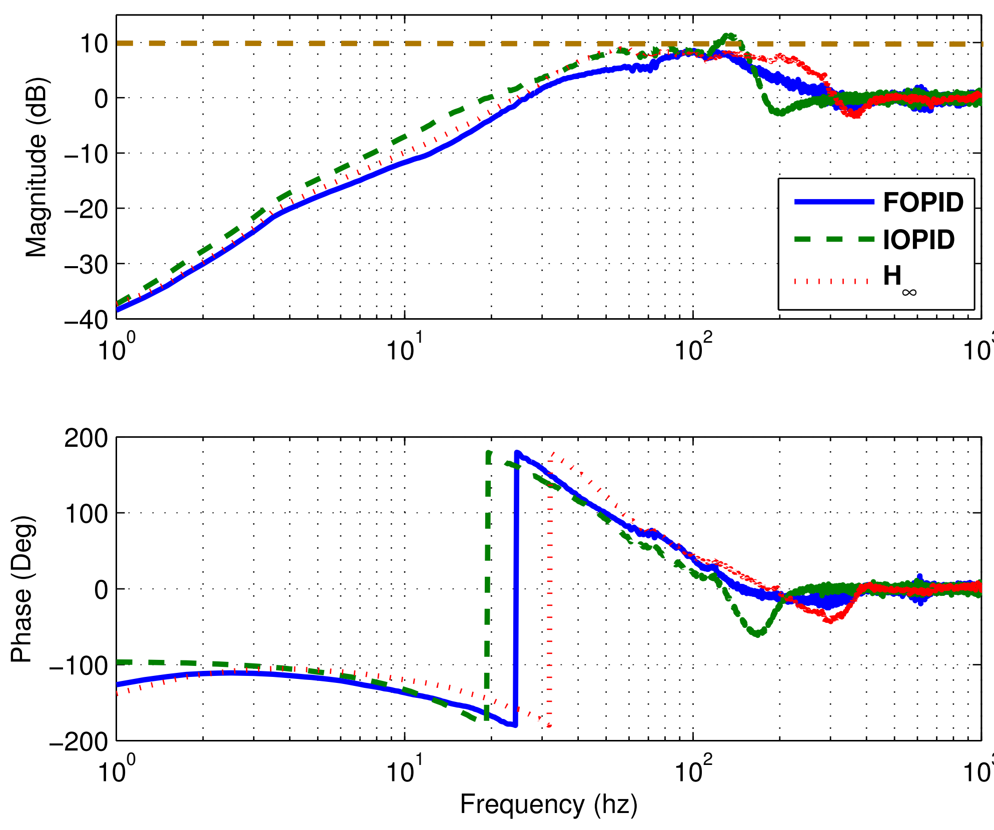

Figure 5.18: Bode plots of the thrust AMB sensitivity function

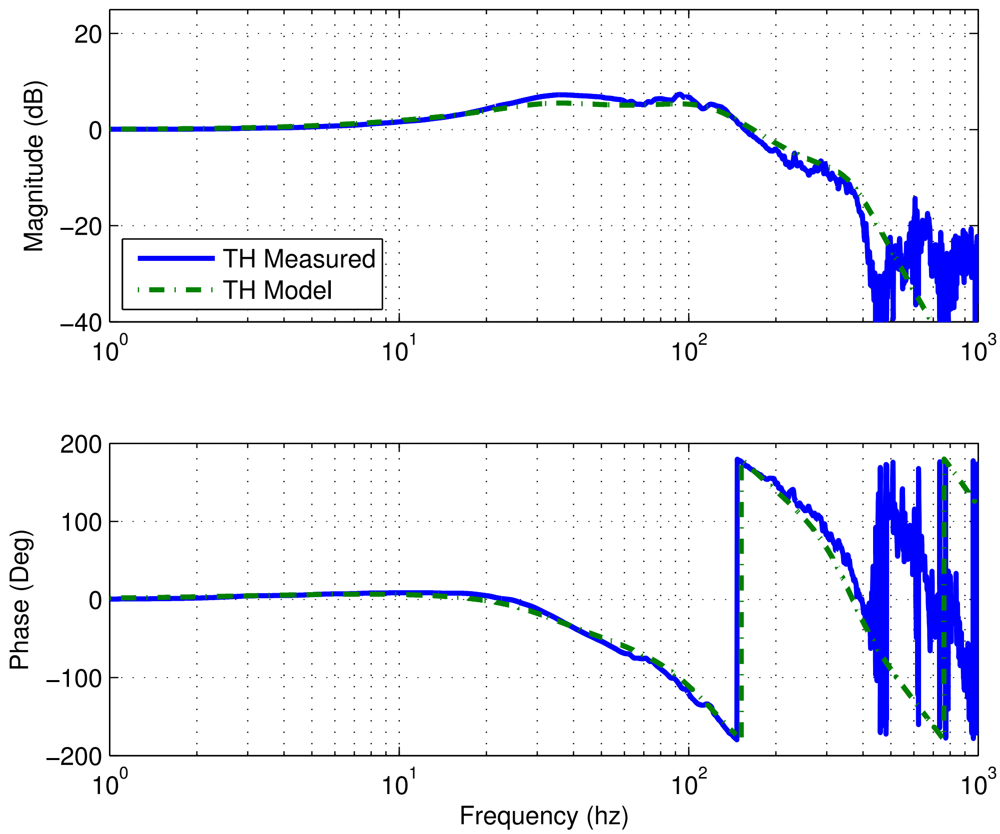

Figure 5.19: Bode plots of the thrust AMB sensitivity function under the FOPID controller

5.4 Summary

With the specified control objectives that are based on the accepted industrial standards for machinery equipped with magnetic bearings, including ISO 14839 and API 617, the FOPID controllers are designed for rotor suspension in both the radial and the axial directions.

For the rotor lateral dynamics, the control objectives include the peak of the sensitivity function, the rotor vibration caused by the unbalanced forces, and the transient response performance. The design begins with the determination of whether to use the centralized or the decentralized control structure. The simulation results reveal that the centralized control structure provides better performance. Afterward, three tuning methods namely, the Genetic Algorithm (GA) method, the Differential Evolution (DE) method, and the Particle Swarm Optimization (PSO) method, are investigated for their effectiveness for the FOPID controller design. The results show that the DE method achieves the best performance. For comparison, the IOPID controller is designed based on the centralized structure and tuned by the DE optimization method. Moreover, the designed and implemented LQG controller reported in [73] is also compared with the designed FOPID controller. The experimental results for rotor vibration with the rotor spinning at speeds ranging from 500 rpm to 16,500 rpm show that the FOPID results in the smallest rotor vibration and the IOPID results in the largest vibration peak, while the rotor vibration under the LQG controller falls in between the results under the FOPID and the IOPID controllers. In addition, in terms of the peak value of the sensitivity function, the FOPID controller results in the smallest and it falls into Zone A specified by the ISO standard, while LQG controller also achieve the Zone A specification with a slightly larger peak value of the sensitivity function than the FOPID controller. On the other hand, the IOPID controller can achieve only Zone B specification.

For the rotor axial dynamics, the FOPID controller is designed based on the objectives specified by weighting functions developed in the previous work [73]. Three different tuning methods are investigated. The results show that the DE method can achieve the best performance as in the previous design. For comparison, the IOPID controller is designed based on the same objectives and the same optimization algorithm as the FOPID controller. Moreover, the designed H_∞ controller for the rotor axial dynamics in [73] is also analyzed for comparison. Finally, the experimental results show that the FOPID controller achieves approximately the same value of the sensitivity function peak as achieved by H_∞ controller, and once again their performance falls into Zone A specification. In contrast, the value of the sensitivity function peak under the IOPID controller exceeds the Zone A level.

Chapter 6

Fractional Order Control of Compressor Surge

6.1 Design of FOPID surge controller

The objective in the surge control design is to stabilize the compression system in the surge condition, where the equilibrium operating point ($\Phi_{\rm eq}$, $\Psi_{\rm eq}$) is beyond the surge line limit. As shown in Figure 6.1, the two inputs of the surge controller K from the compression system G are the compressor mass flow rate ξ_1 and the plenum pressure rise ξ_2. The controller output is the reference impeller tip clearance $\delta_{\rm cl,ref}$, which is fed into the closed-loop thrust AMB system $T_{\rm amb}$. The thrust AMB controller will track the desired tip clearance specified by the surge controller in order to induce an appropriate amount of pressure rise for surge stabilization. In the actual implementation, it is impossible to have perfect tracking by the thrust AMB due to external disturbances. This means that the performance of the surge controller will be degraded. Because of this limitation, the surge control design must take into account disturbances, which can impact the interaction between the surge and thrust AMB controllers. Moreover, Yoon et al. suggested in [73] that the closed-loop system shown in Figure 6.1 can be restructured as shown in Figure 6.2. This way the closed-loop dynamics of the compression system and the rotor/thrust AMB system are separated.

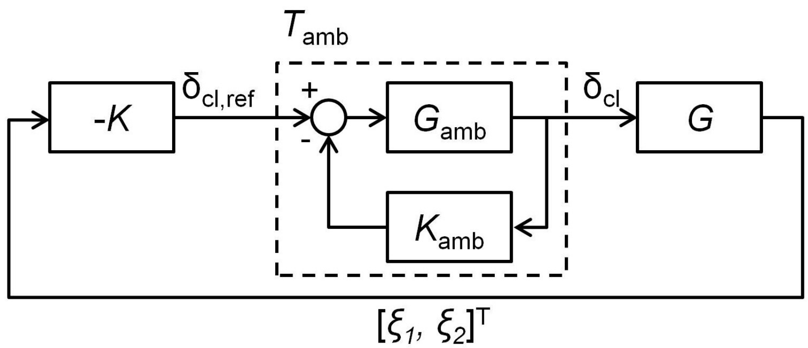

Figure 6.1: Closed-loop compression system with surge controller diagram

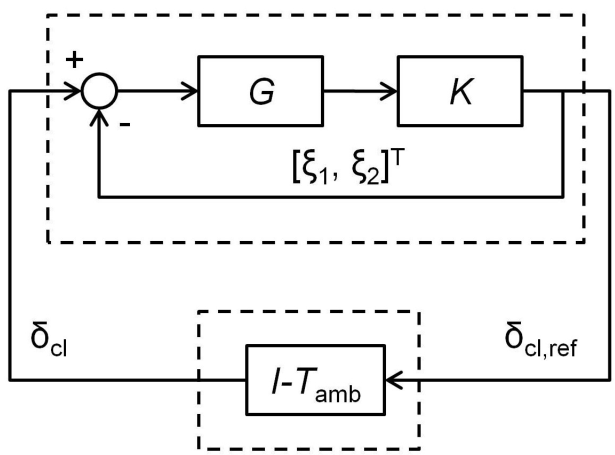

Figure 6.2: Modified closed-loop compression system with surge controller diagram

Here, the surge controller for each input-output pair consists of a fractional PD controller, a lowpass filter, and a notch filter. The center frequency of the notch filter is placed at a frequency slightly lower than the critical frequency of the system (approximately 5-10 Hz lower) so that the designed controller can provide more damping at the critical frequency. The structure of the notch filter is

$$G_{\text{notch}} = \frac{s^2 + \omega_n^2}{s^2 + 2\zeta\omega_n s + \omega_n^2},$$

where ω_n is the center frequency of the notch and ζ indicates the notch sharpness. The objectives for the surge controller tuning are adopted from [73] as follows.

1. Stability of closed-loop system: The closed-loop stability condition is derived from the Small Gain Theorem. The optimization goal is to have $J_1 < 1$.

$$J_1 = \left\|(I + KG)^{-1}KG(I - T_{\text{amb}})\right\|_\infty .$$

2. Robust stability condition:

$$J_2 = \|W_1 S_i K G W_3\|_\infty .$$

3. Control effort according to the reference equilibrium operating point condition:

$$J_3 = \|W_1 S_i K W_4\|_\infty .$$

4. Transmission of the input disturbance to the plant output signal condition:

$$J_4 = \|W_2 S_o G W_3\|_\infty .$$

5. Closed-loop dynamics from the reference equilibrium operating point to the plant output signal condition:

$$J_5 = \|W_2 S_o G K W_4\|_\infty ,$$

where

$$S_i = (I + KG)^{-1},$$

$$S_o = (I + GK)^{-1},$$

and the weighting functions are as defined in [73], which are based on the interconnected system shown in Figure 6.3, as follows.

$$\begin{aligned} W_1(s) &= I, \\ W_2(s) &= 0.001I, \\ W_3(s) &= 2\frac{(s+0.1)}{(s+300)}I, \\ W_4(s) &= 2000\frac{(s+0.1)}{(s+3000)}\begin{bmatrix} 1.5 & 0 \\ 0 & 1 \end{bmatrix}. \end{aligned}$$

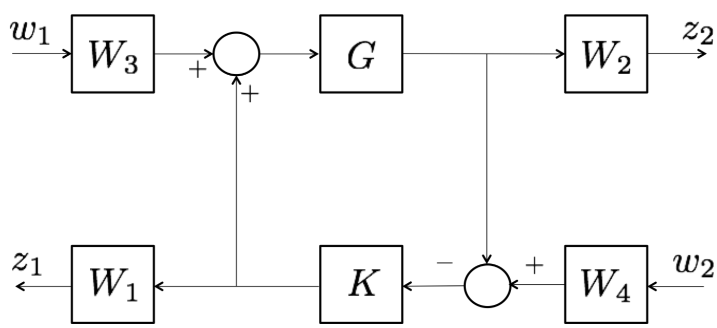

Figure 6.3: Interconnected system for the design of the surge controller

Similar to the rotor suspension control design, all objective functions will be combined as a single cost function during the optimization process, which is as follows.

$$J = \max\{J_1, J_2, J_3, J_4, J_5\}.$$

The optimization goal is to have the infinity norm of all objective functions to be smaller than 1. Once again, the investigation of three tuning methods is performed.

The population size is 200, which is the same value used in the control of rotor lateral dynamics because the number of parameters to tune are equal. The crossover rate, the weight factor, the acceleration rate, and the mutation rate are kept the same as in the previous design.

Controller characteristics	GA	DE	PSO
Infinity norm of objective functions	1.048	0.991	1.019

Table 6.1: Comparison of the performance of different tuning methods

Table 6.1 summarizes the resulting infinity norms of the objective functions of all tuning methods. In addition, the resulting magnitude plots of all objectives, except the stability objective, resulting from the three different tuning methods are shown in Figure 6.4. It can be observed that only the DE algorithm results in the maximum magnitude of the objective functions smaller than 1. Therefore, this controller design will be used for implementation and comparison with the other kind of controllers.

Table 6.2 summarizes the values of the FOPD controller and the notch filter parameters obtained from the DE optimization.

Input - Output	K_P	K_D	μ	ζ	ω_n
ξ_1 - $\delta_{\mathrm{cl,ref}}$	2.49×10^{-3}	9.11×10^{-5}	1.123	0.709	18.46 Hz
ξ_2 - $\delta_{\mathrm{cl,ref}}$	1.21×10^{-2}	1.01×10^{-4}	0.563	3.489	12.10 Hz

Table 6.2: Parameters of tuned fractional surge controller

For comparison, the conventional PID controller is tuned based on the same objectives and algorithms as the FOPID controller. Moreover, the surge H_∞ controller that was designed for the same compression system reported in [73] is also considered. Table 6.3 summarizes the infinity norms of all objectives of the IOPID, the FOPID, and the H_∞ controllers, and their magnitude plots are illustrated in Figure 6.5.

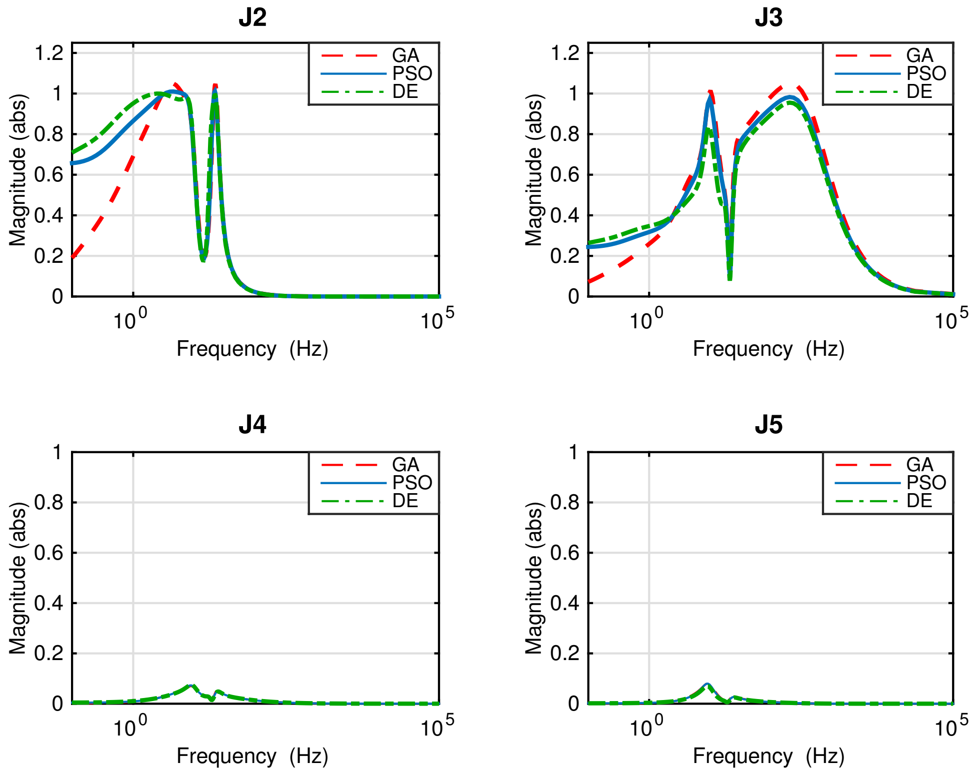

Figure 6.4: Magnitudes of objective functions from three different tuning methods (GA, DE, and PSO)

Controller characteristics	PID	FOPID	H_∞
Infinity norm of objectives	1.143	0.991	0.969
Controller order as implemented	6	6	7

Table 6.3: Performance of surge controllers

6.2 Simulation results of surge control

With the derived surge controller, the simulation was carried out on the nonlinear compression system model described by Eqs. (4.5a) - (4.5d). The closed-loop dynamics

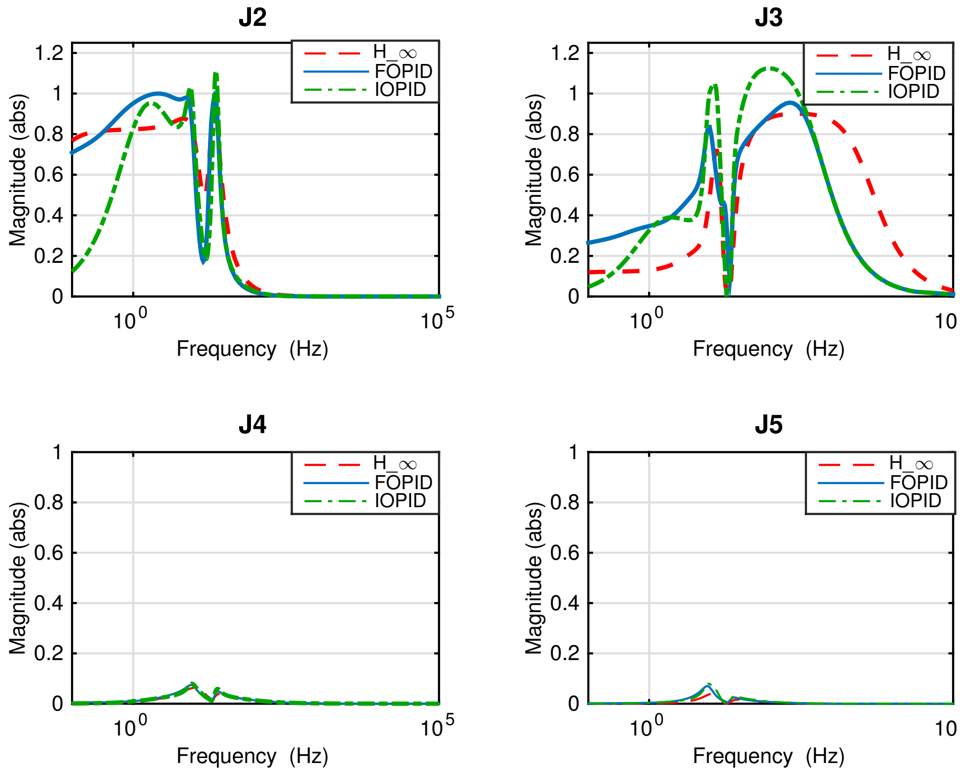

Figure 6.5: Magnitudes of objective functions for all controllers

of the thrust AMB is represented by a third order low-pass Butterworth filter with the cutoff frequency of 70 Hz. Figure 6.6 shows the simulation results of the compression system when the surge controller is unactivated. In the simulation, the throttle valve was gradually closed from 20% opening (stable) to 16% opening (unstable), where the crossing between the two regions occurs at 18.5% opening. Since there is no surge controller activated, the variation of the impeller tip clearance remains zero as shown in Figure 6.6(b). Figure 6.6(c) shows that the states ξ_1 and ξ_2 of the compression system demonstrate large oscillation magnitudes after the system enters the surge region. Similarly, the value of the plenum pressure rise Ψ_p demonstrates large oscillation magnitudes after the system enters the surge region as shown in Figure 6.6(d).

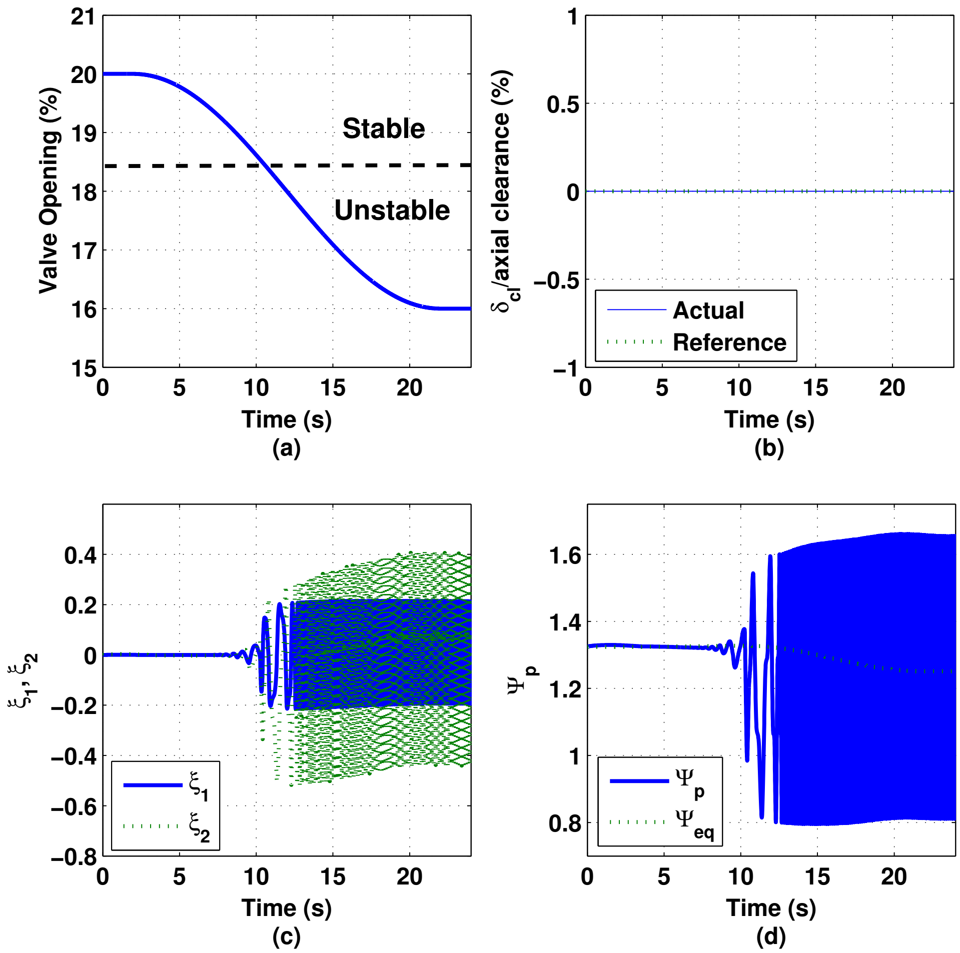

Figure 6.6: Simulation results of the compression system with the surge controller unactivated

Figure 6.7 shows the simulation results of the compression system when using the PID controller that is tuned with the same algorithm and objectives as for the FOPID controller. This conventional PID controller can stabilize the compression system even after the system enters the surge region, but the system becomes unstable at approximately 16.2% of throttle valve opening.

Figure 6.8 shows the simulation results of the compression system when the H_∞ surge controller is activated. The compression system is stabilized even when it enters the unstable region by modulating the impeller tip clearance as shown in Figure 6.8(b).

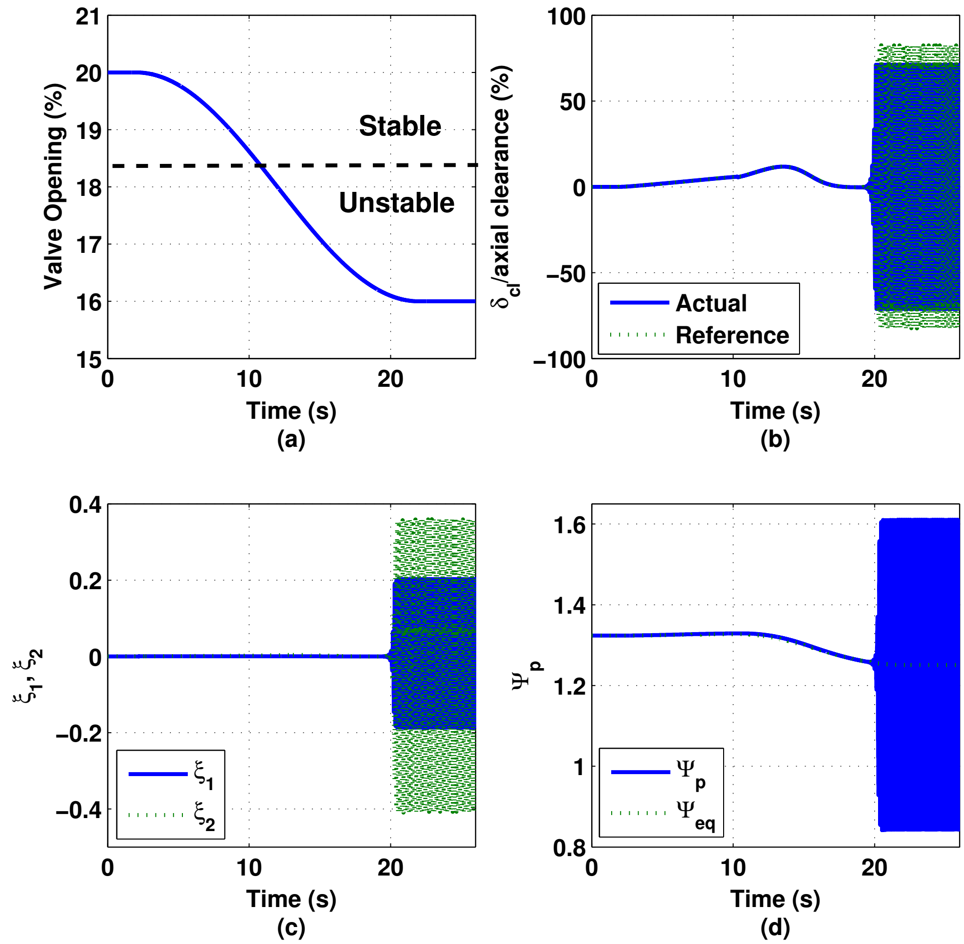

Figure 6.7: Simulation results of the compression system under the PID surge controller

Both states ξ_1 and ξ_2 of the compression system are still stable even after the system enters the unstable region as shown in Figure 6.8(c). Finally, Figure 6.8(d) shows the values of the plenum pressure rise Ψ_p and the equilibrium pressure rise Ψ_eq that stabilize the compression system. Similar to the performance provided by the H_∞ surge controller, the FOPID surge controller stabilizes the compression system. In addition, the peak value of the tip clearance modulation is approximately the same as in the case of the H_∞ surge controller as shown in Figure 6.9(b). Also, the maximum values of the states shown in Figure6.9(c) stay stable after the system enters the surge

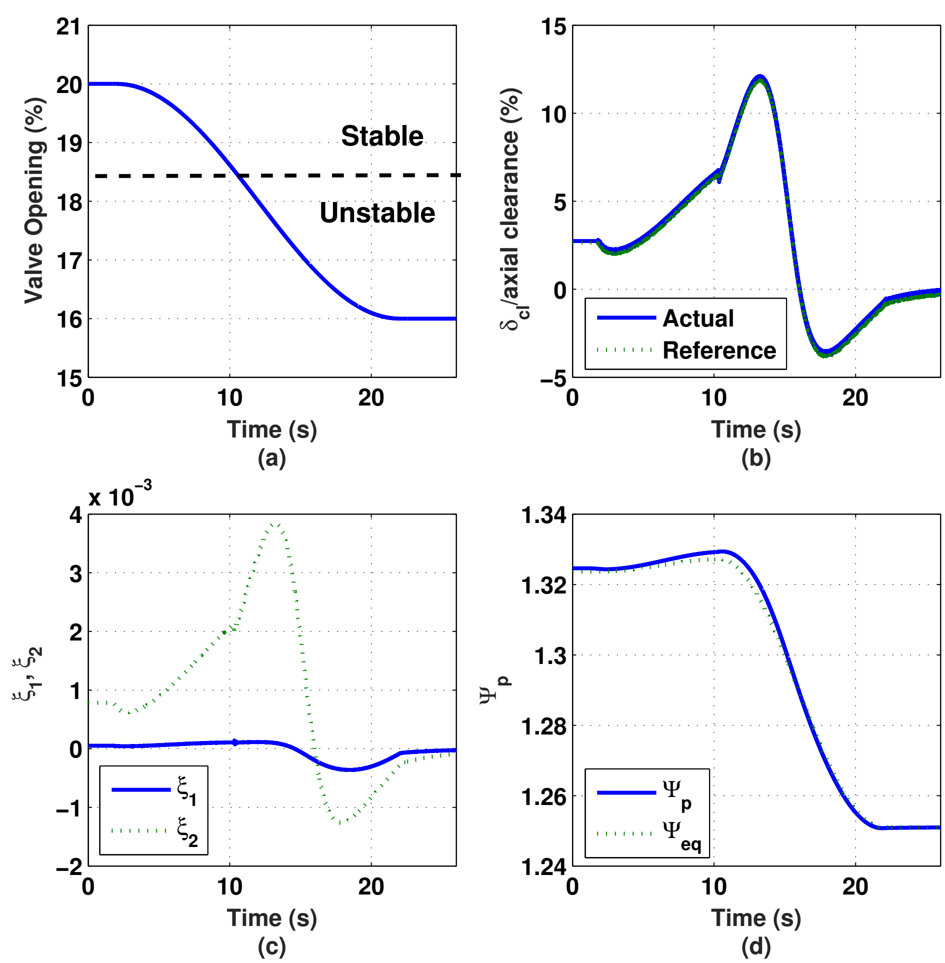

Figure 6.8: Simulation results of the compression system under the H_∞ surge controller

region. It can be seen that the closed-loop system with the FOPID surge controller is more robust than in the case of the PID surge controller. Finally, the simulation results demonstrate that the FOPID surge controller can stabilize the compression system to the same level as the H_∞ surge controller during the simulation.

6.3 Experimental test of surge control

The surge controller will be activated when needed on top of the rotor suspension controllers that are always active throughout the operating period. Since the surge

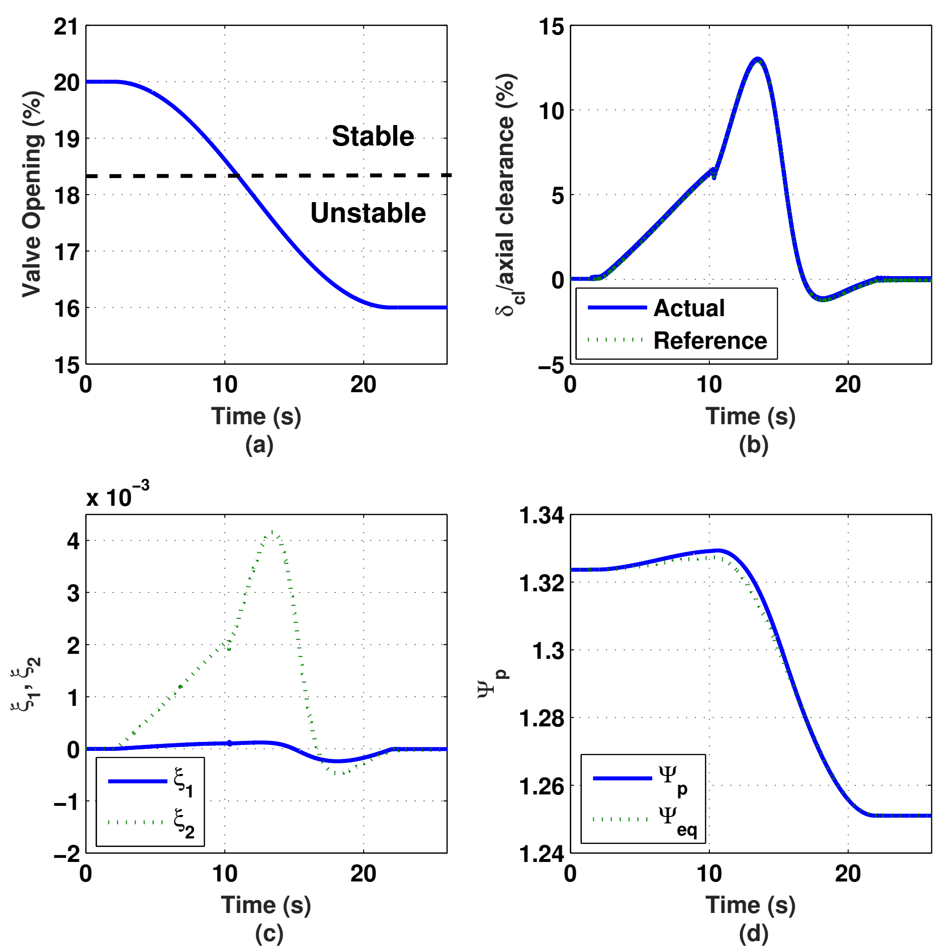

Figure 6.9: Simulation results of the compression system under the FOPID surge controller

control implementation will be tested at 16,290 rpm, which will store high potential energy, the accidental contact by improper surge controller implementation can cause more damage to the compressor than the surge instability. Therefore, a safety mechanism for the surge controller activation is required. Within this study, prior to the surge controller activation, rotor vibration is checked. If rotor vibration is within the predefined limit, the surge controller is engaged in the control process. Then, the reference of the rotor axial position computed by the surge controller is limited to ±70% of the available axial clearance. Otherwise, the reference of the rotor axial position is set to zero for a safe operating environment. The flow chart of the surge controller operation is illustrated in Figure 6.10.

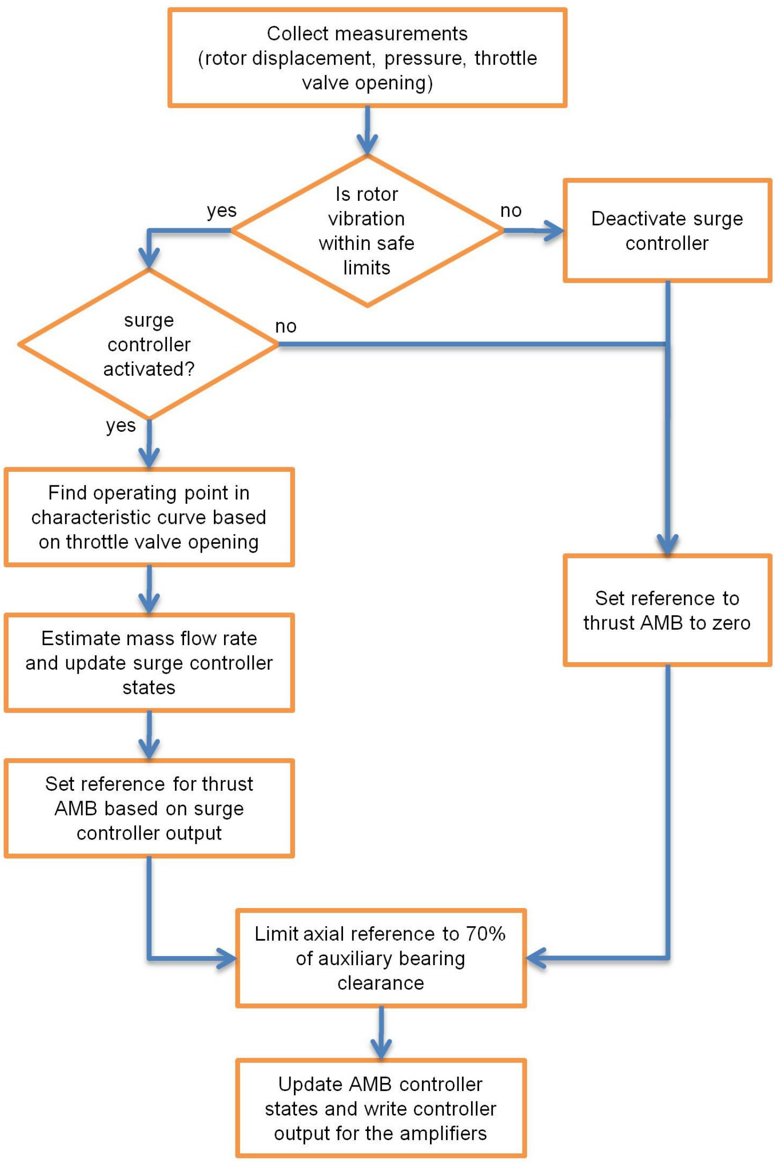

Figure 6.10: Flow chart of the surge control implementation [73]

With the rotor spinning at 16,290 rpm, the system is driven into surge by gradually closing down the throttle valve starting from a 21.0% opening, in 0.1% decrements, for smooth operation. Figure 6.11 shows that the compression system enters the surge at a 17.8% of the throttle valve opening in the absence of the surge controller.

The frequency response plot shows large peaks at approximately 7 Hz and 21 Hz, which agrees with the prediction of the compression system characteristics described in Section 4.3.

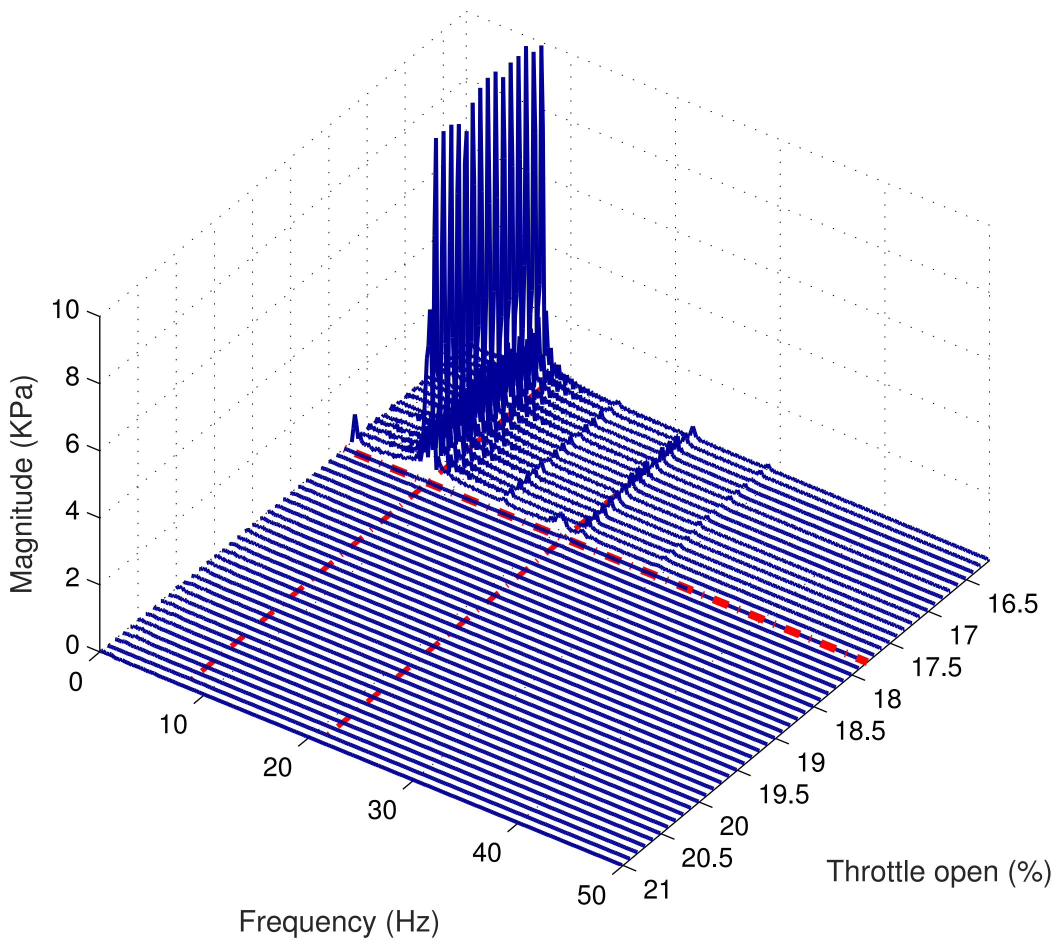

Figure 6.11: Waterfall plot of the frequency response of the measured plenum pressure signal at 16,290 rpm with the surge controller unactivated

For the next surge test, the IOPID surge controller is activated under the same testing condition as for the previous test. Figure 6.12 shows the frequency response of the measured plenum pressure rise when the IOPID surge controller is activated. The large peaks of the frequency response initiate at a 16.9% throttle valve opening position.

The result shows that, with the IOPID surge controller activated, the compression system can operate stably beyond the original surge limit.

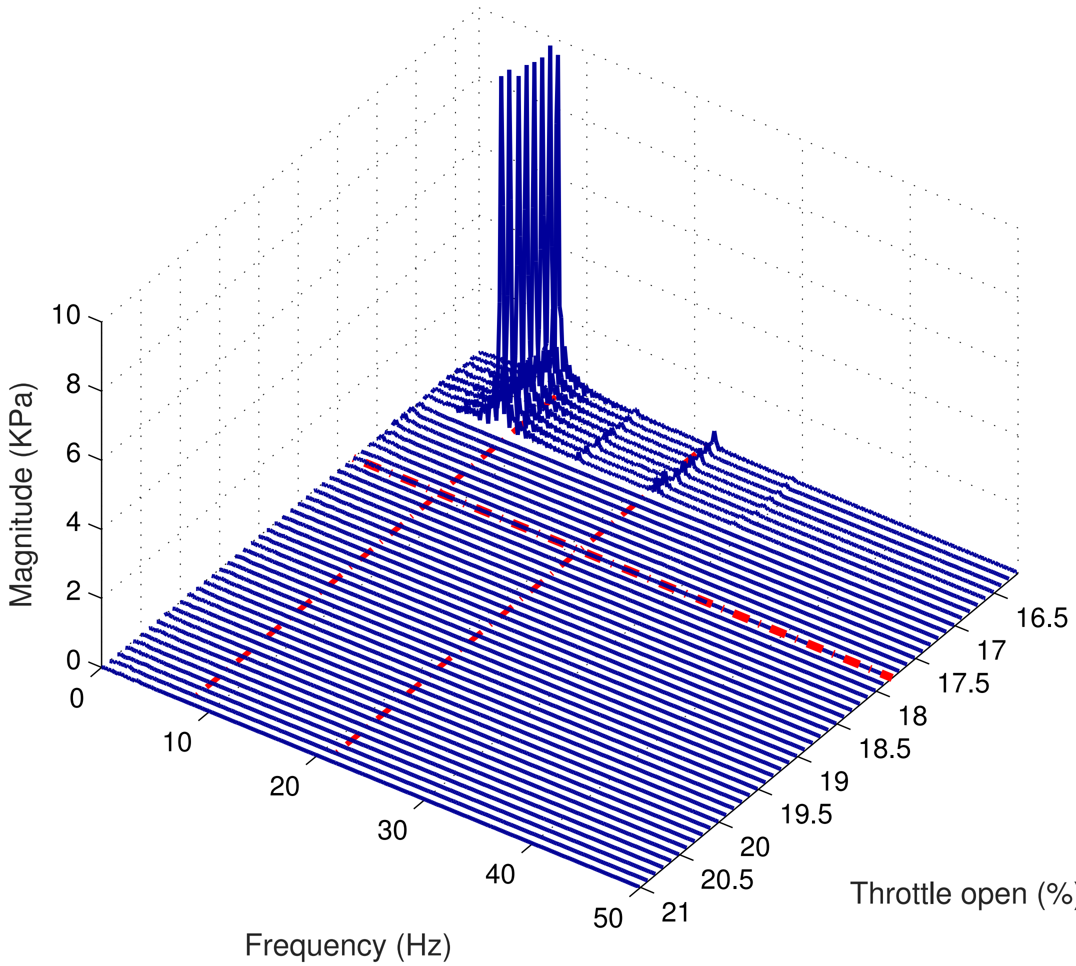

Figure 6.12: Waterfall plot of the frequency response of the measured plenum pressure signal at 16,290 rpm with the IOPID surge controller activated

Figure 6.13 shows the non-dimensional mass flow rate and the plenum pressure rise on the characteristic curve during stable operation. The measurements with the surge controller unactivated are marked by 'o'. These values are measured from 21% valve opening until 17.8%, where the surge initiates. The measurements marked by 'x' represent the extended operating points when the IOPID controller is activated. It can be observed that the surge limit is extended in terms of the mass flow range from the uncontrolled case by 11.97%.

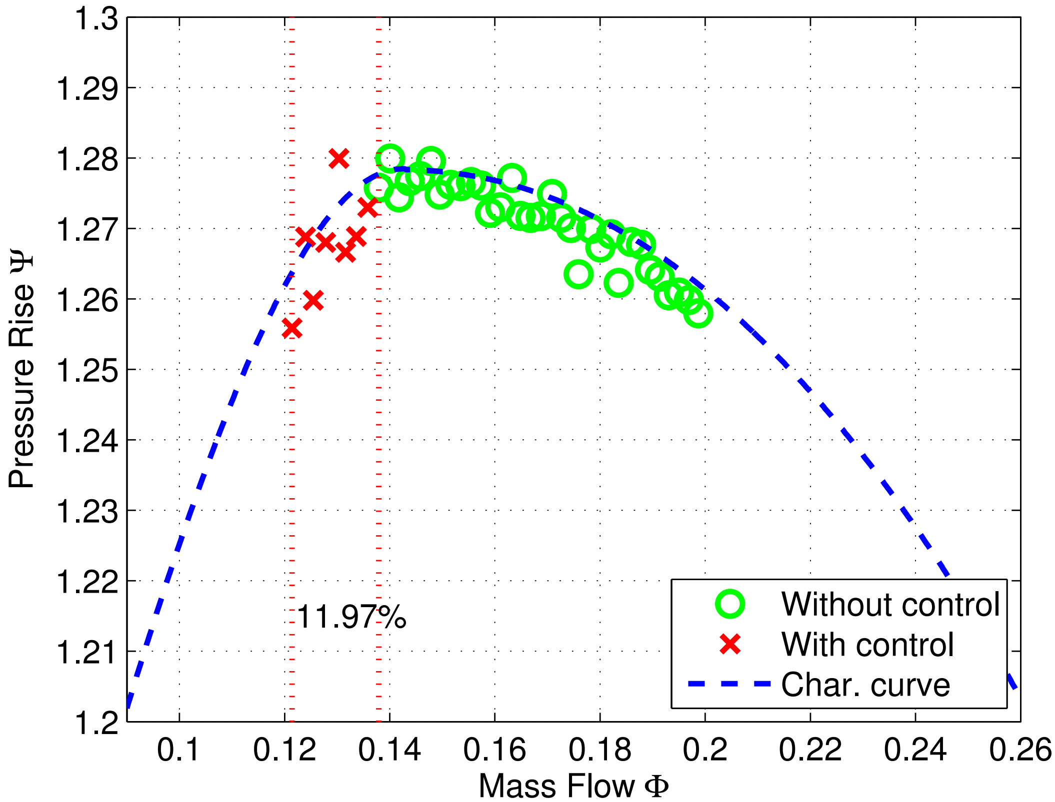

Figure 6.13: Compressor steady-state operation on the characteristic curve at 16,290 rpm with the IOPID surge controller activated and unactivated, respectively

In addition, the measured and the reference of the ratio of the impeller tip clearance and the available axial clearance are shown in Figure 6.14(b). The maximum value of the impeller tip clearance is about 40% of the available axial clearance. This shows that the IOPID surge controller can operate stably with some axial position margin compared with the predefined ±70% of the available clearance. Figure 6.14(c) shows the values of the surge controller states, ξ_1 and ξ_2, when the throttle valve is opened at

17.0%. Then, the non-dimensional measured pressure rise and its equilibrium values are illustrated in Figure 6.14(d).

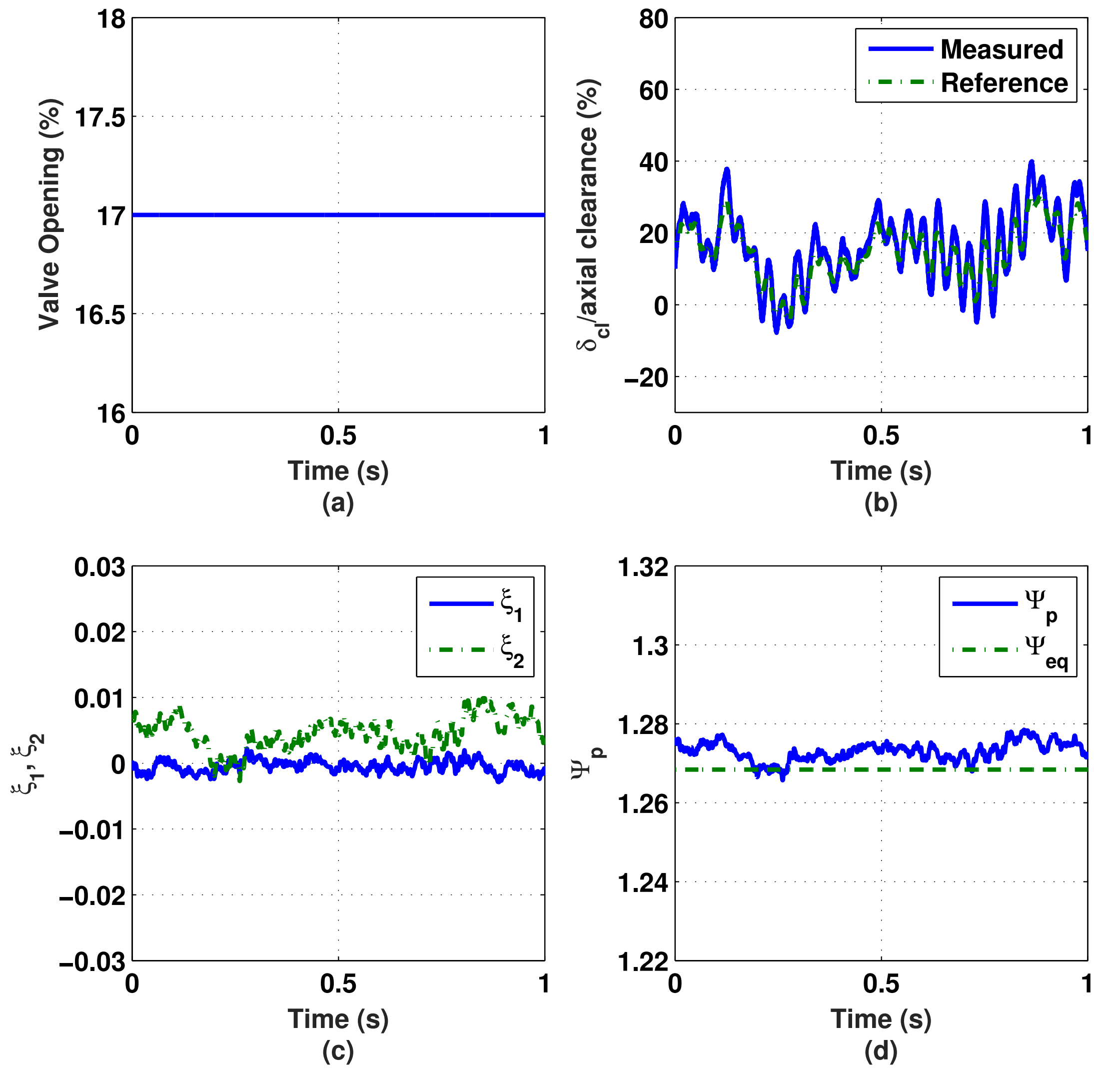

Figure 6.14: Experimental results of the compression system under the PID surge controller at 17.0% throttle valve opening

For the case of the FOPID surge controller test, Figure 6.15 shows the frequency response of the measured plenum pressure rise. It can be noticed that the compression system enters surge when the throttle valve opens at 16.2%, which further extends the surge limit where the IOPID surge controller remains stable until 17.0% opening.

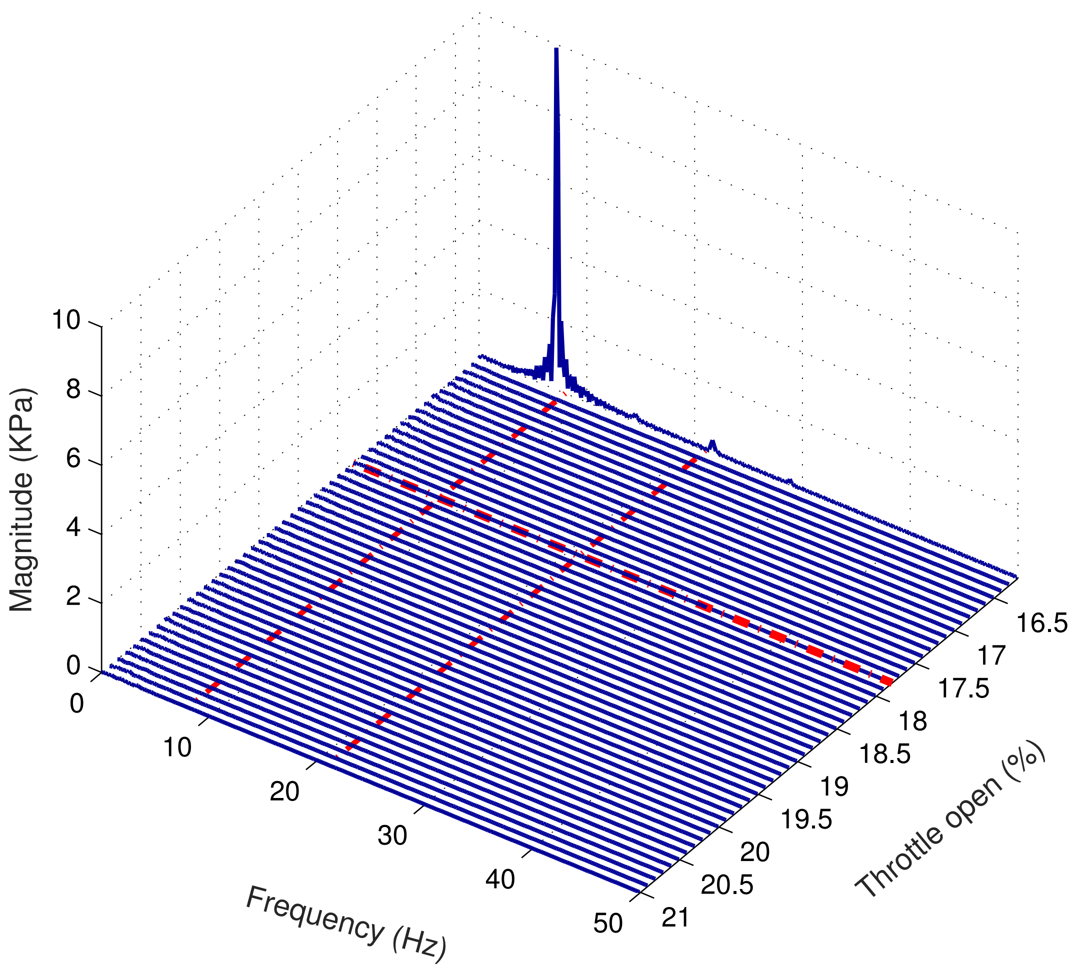

Figure 6.15: Waterfall plot of the frequency response of the measured plenum pressure signal at 16,290 rpm with the FOPID surge controller activated

Figure 6.16 shows the non-dimensional mass flow rate and the plenum pressure rise on the characteristic curve during stable operation with the FOPID surge controller activated after the surge limit. The measurements with the FOPID surge controller unactivated are marked by ‘o’. These values are measured from 21% valve opening until 17.8%, where the surge initiates. The measurements marked by ‘x’ represent the extended operating points when the FOPID controller is activated. It can be observed that the surge limit is extended in terms of the mass flow range from the uncontrolled case by 22.26%.

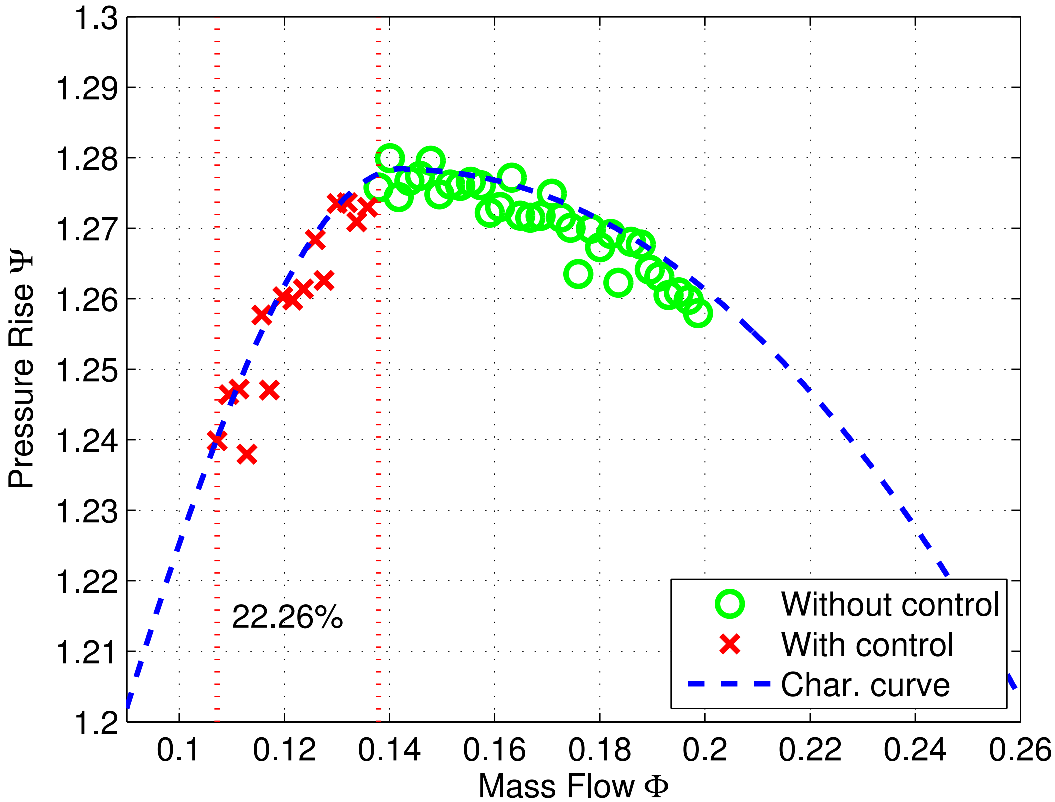

Figure 6.16: Compressor steady-state operation on the characteristic curve at 16,290 rpm with the FOPID surge controller activated and unactivated, respectively

In addition, the maximum value of the impeller tip clearance is approximately 35% of the available axial clearance as shown in Figure 6.17(b). This shows that the FOPID surge controller results in a slightly larger axial clearance margin than the IOPID surge controller case. Figure 6.17(c) shows the values of the surge controller states, ξ_1 and ξ_2, when the throttle valve is opened at 16.3%. The non-dimensional measured pressure rise and its equilibrium values are illustrated in Figure 6.17(d).

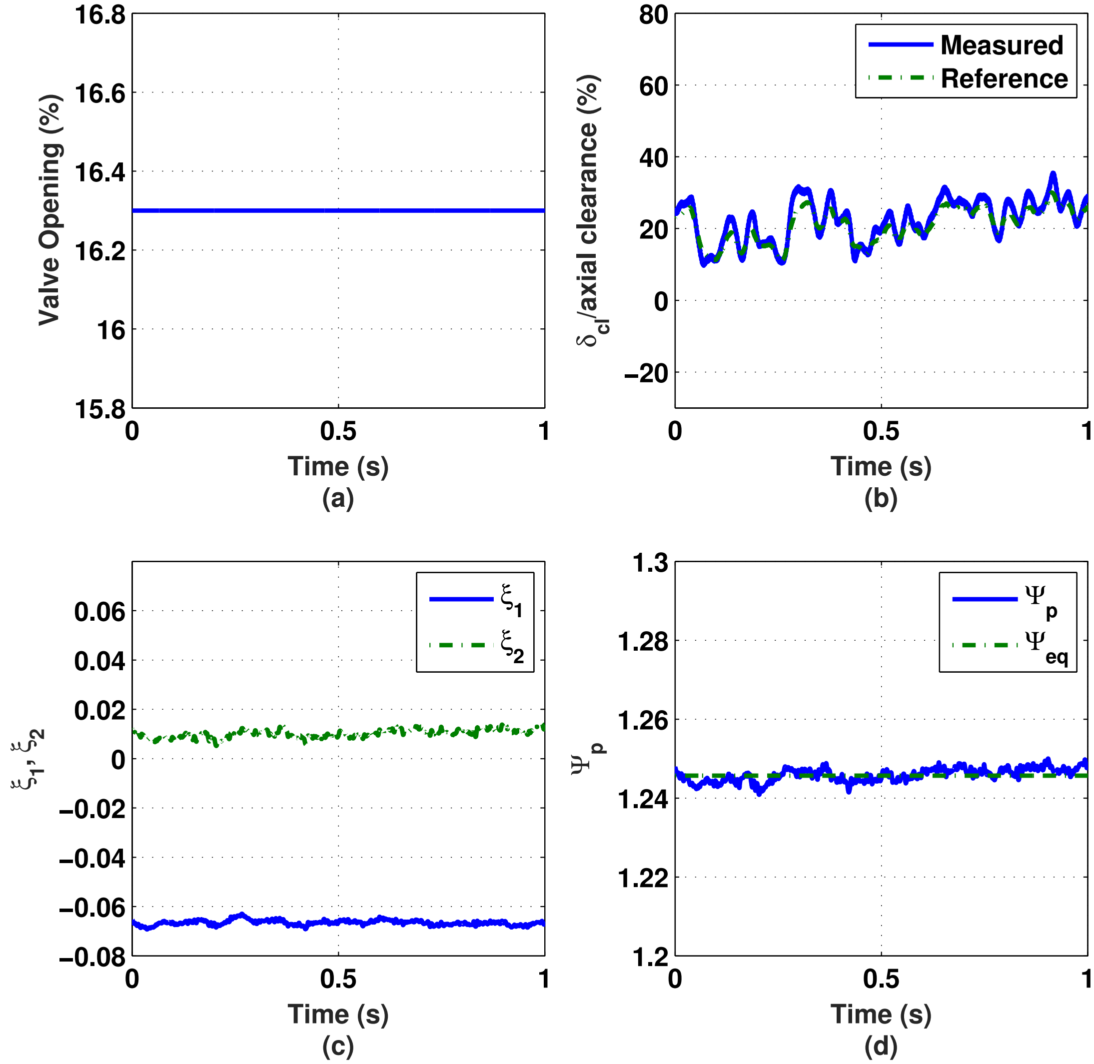

Figure 6.17: Experimental results of the compression system under the FOPID surge controller at 16.3% throttle valve opening

Finally, for the case when the H_∞ surge controller is activated, Figure 6.18 shows that the compression system remains stable when the throttle valve opens as small as 16.2%. This extends the throttle valve opening for another 0.1% beyond the FOPID surge controller case. Figure 6.19 shows the non-dimensional mass flow rate and the plenum pressure rise on the characteristic curve during stable operation with the H_∞

surge controller activated after the surge limit. The measurements with the surge controller unactivated are marked by 'o'. These values are measured from 21% valve opening until 17.8%, where the surge initiates. The measurements marked by 'x' represent the extended operating points when the H_∞ controller is activated. It can be observed that the surge limit is extended in terms of the mass flow range from the uncontrolled case by 22.92%.

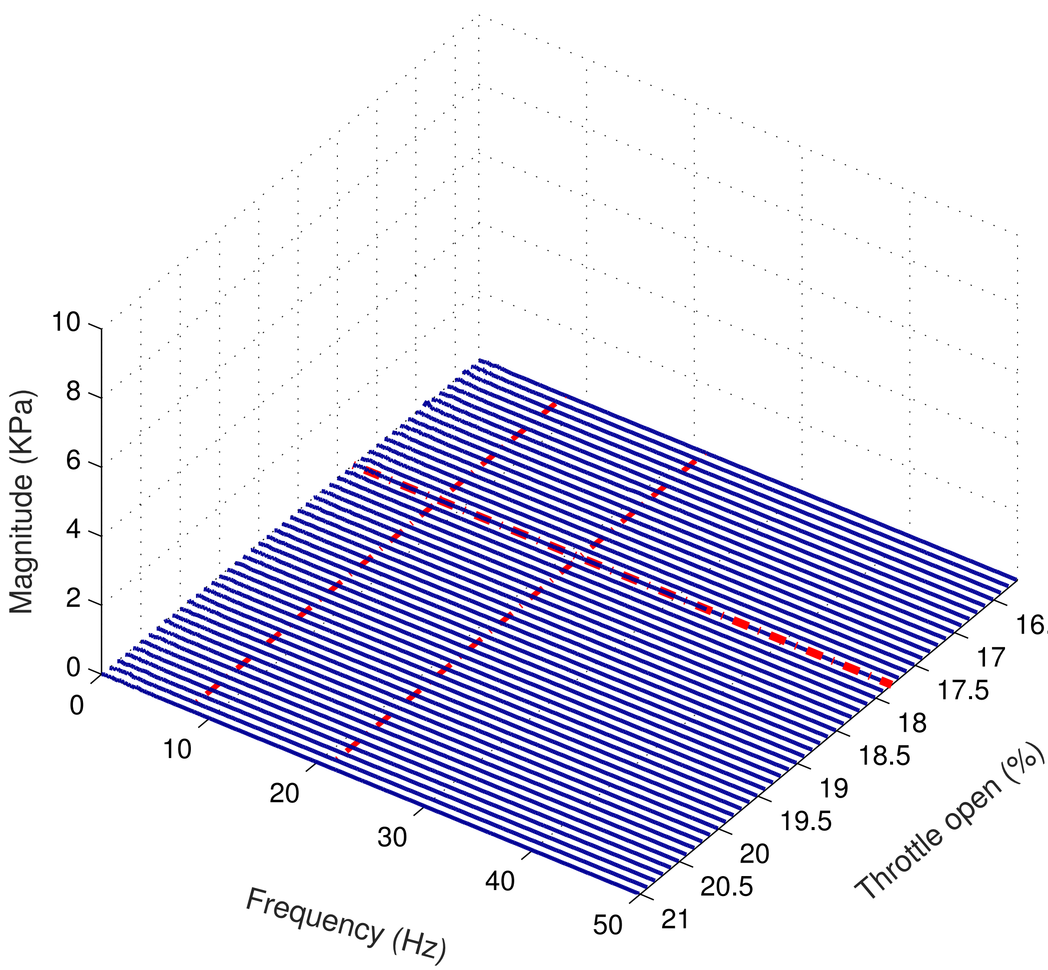

Figure 6.18: Waterfall plot of the frequency response of the measured plenum pressure signal at 16,290 rpm with the H_∞ surge controller activated

In addition, the maximum value of the impeller tip clearance is about 35% of the available axial clearance as shown in Figure 6.20(b). This shows that the H_∞ surge controller can operate stably with approximately the same axial clearance margin as the FOPID surge controller case. Figure 6.20(c) shows the values of the surge controller states, ξ_1 and ξ_2, when the throttle valve is opened at 16.2%. The non-dimensional measured pressure rise and its equilibrium values are illustrated in Figure 6.20(d).

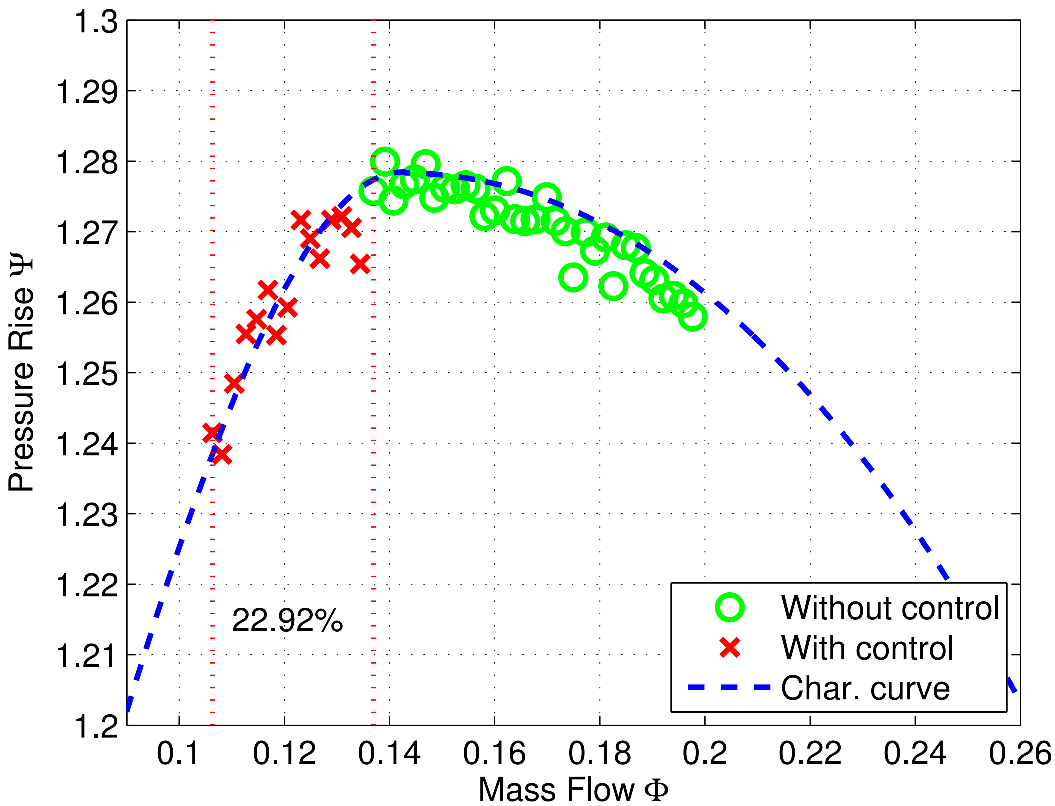

Figure 6.19: Compressor steady-state operation on the characteristic curve at 16,290 rpm with the H_∞ surge controller activated and unactivated, respectively

6.4 Summary

This chapter presents the design of the FOPID surge controller with three different tuning methods namely, the Genetic Algorithm (GA) method, the Differential Evolution (DE) method, and the Particle Swarm Optimization (PSO) method. Simulation results show that the FOPID surge controller tuned by the DE method achieves the best performance. Therefore, this design is used for the implementation on the compressor test rig. For comparison, the IOPID surge controller was designed based on the same objectives and optimization algorithm.

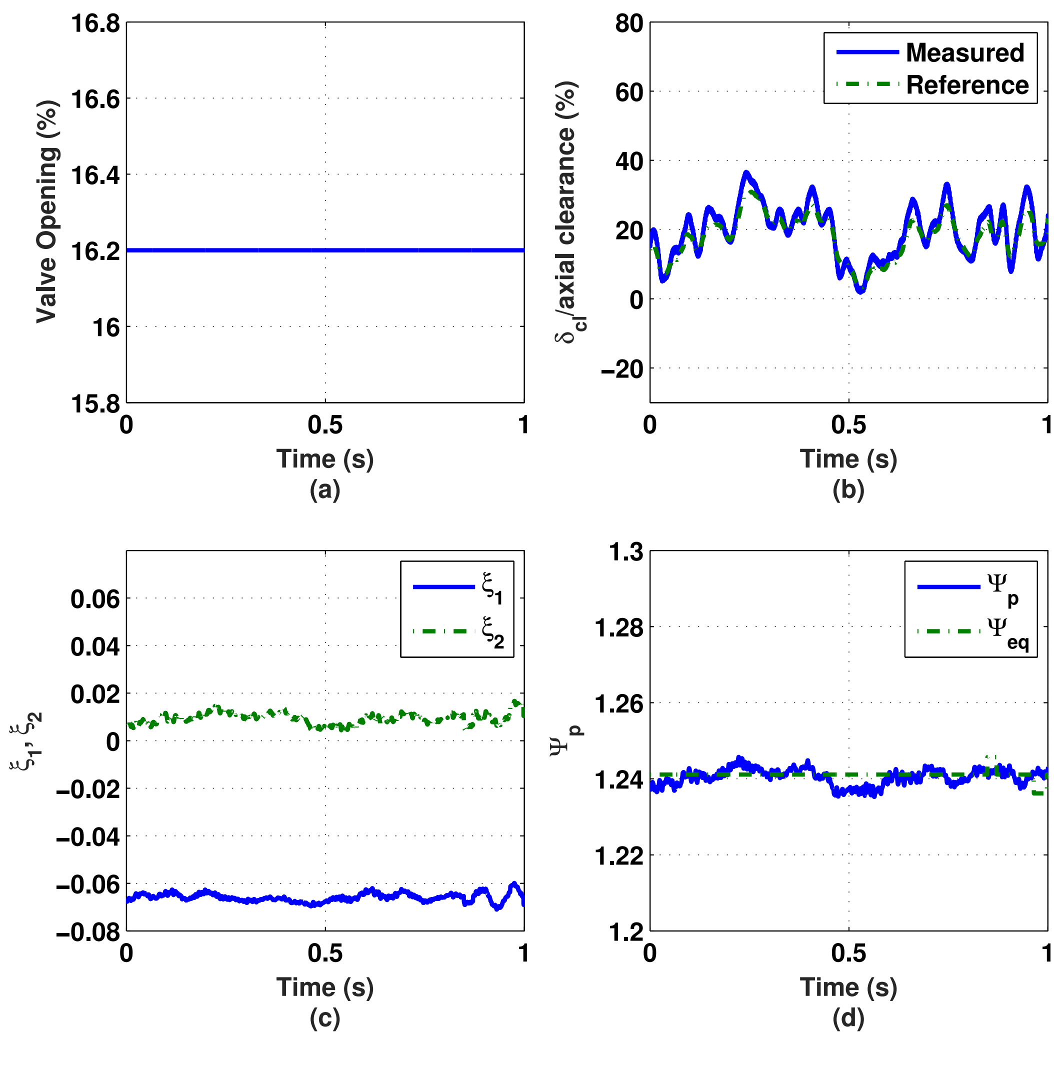

Figure 6.20: Experimental results of the compression system under the H_∞ surge controller at 16.2% throttle valve opening

Simulation results show that the IOPID controller can stabilize the compression system beyond the surge limit, but not as much as the FOPID and H_∞ surge controllers can. These simulation results are then validated by experimental testing on the compressor test rig. The experimental results show that the IOPID surge controller can extend the surge limit in terms of the mass flow range from the uncontrolled case by 11.96%. For the case of the FOPID and the H_∞ surge controllers, the surge limit is extended by 22.26% and 22.92%, respectively.

Chapter 7

Conclusions

This dissertation demonstrates the design, analysis, and implementation of the fractional order PID controller (FOPID) for the control of vibration and surge in a centrifugal compressor by active magnetic bearings (AMB). This is the first time that the FOPID controller is designed for and implemented on a compressor equipped with magnetic bearings. The effectiveness of the FOPID controller is investigated in two aspects.

The first aspect is on the FOPID controller design for the rotor suspension in both radial and axial directions. For the rotor lateral dynamics, the control objectives include the peak of the sensitivity function, the rotor vibration caused by the unbalanced forces, and the transient response performance. The design starts with the determination of whether to use a centralized or decentralized control structure. The simulation results reveal that the centralized control structure provides better performance. Afterward, three tuning methods namely, the Genetic Algorithm (GA) method, the Differential Evolution (DE) method, and the Particle Swarm Optimization (PSO) method, are investigated for their effectiveness for the FOPID controller design. The results show that the DE method achieves the best performance. For comparison, the IOPID controller is designed based on the centralized structure and tuned also by the DE optimization method. Moreover, the LQG controller designed and implemented in [73] is also compared with the designed FOPID controller. The experimental results for rotor vibration with the rotor spinning at speeds ranging from 500 rpm to 16,500 rpm show that the FOPID results in the smallest rotor vibration and the IOPID results in the largest vibration peak, while the rotor vibration under the LQG controller falls in between the results under the FOPID and the IOPID controllers. In addition, in terms of the peak value of the sensitivity function, the FOPID controller results in the smallest and it falls into Zone A specified by the ISO standard, while LQG controller also achieve the Zone A specification with a slightly larger peak value of the sensitivity function than the FOPID controller. On the other hand, the IOPID controller can achieve only Zone B specification. For the rotor axial dynamics, the FOPID controller is designed based on the objectives specified by the weighting functions given in the previous work [73]. Three different tuning methods are investigated. The results show that the DE method achieves the best performance as in the previous design. For comparison, the IOPID controller is designed based on the same objectives and optimization algorithm used for the FOPID controller. Moreover, the H_∞ controller for the rotor axial dynamics designed and implemented in [73] is also analyzed for comparison. Finally, the experimental results show that the FOPID controller archives approximately the same value for the sensitivity function peak as achieved by the H_∞ controller, and their performance falls into Zone A specification. In contrast, the value of the sensitivity function peak of the IOPID controller exceeds the Zone A level.

The second aspect is on the FOPID controller design for the surge control in the centrifugal compressor by using magnetic bearings. The FOPID controller is designed based on the control objectives given by the weighting function adopted from [73]. Three tuning methods are investigated for their effectiveness. The result shows that DE optimization algorithm achieves the best performance among the three. Additionally, the IOPID controller is designed based on the same objectives and tuning algorithm. Simulation results show that the IOPID controller can stabilize the compression system beyond the surge limit, but not as much as in the case of the FOPID and the H_∞ surge controllers. The simulation results are validated by the experimental testing on the compressor test rig. The experimental results show that the IOPID surge controller can extend the surge limit in terms of the mass flow range from the uncontrolled case by 11.96%. For the case of the FOPID and the H_∞ surge controllers, the surge limit is extended by 22.26% and 22.92%, respectively.

Based on the simulation and experimental results presented in Chapters 5 and 6, if properly tuned, the FOPID controller designed for the rotor suspension outperforms the IOPID controller with only the variation of the integral and derivative orders. Furthermore, the FOPID controller can achieve performance similar to or even better than advanced controllers such as LQG and H_∞, while the FOPID has simpler controller structure as well as design process.

7.1 Future work

Motivated by the effectiveness of the FOPID controller presented in this dissertation, further development of this work can be summarized as follows:

1. In order to promote the use of the FOPID controllers, an online automatic tuning method for FOPID could be developed for the ease of operation.

2. To further investigate the fractional order control system, the fractional order modeling of some subsystems, such as eddy current effect in thrust bearing and the piping acoustic in the compression system, can be studied.

3. Lastly, the FOPID controller design with the consideration of uncertainties in a system, as usually considered in the advanced controller method, is also an interesting topic of future research.

Bibliography

[1] http://www.skf.com/group/industry-solutions/compressors, access on November 2014.

[2] http://petrowiki.org/Centrifugal-compressor, access on November 2014.

[3] Adolfsson, K., Enelund, M., and Olsson, P. On the fractional order model of viscoelasticity. *Mechanics of Time-dependent materials 9*, 1 (2005), 15–34.

[4] Aldair, A. A., and Wang, W. J. Design of fractional order controller based on evolutionary algorithm for a full vehicle nonlinear active suspension systems. *International Journal of Control and Automation 3*, 4 (2010), 33–46.

[5] American Petroleum Institute API. *API 617: Axial and Centrifugal Compressors and Expander-Compressors for Petroleum, Chemical and Gas Industry Services Washington, DC*, eighth ed., 2014.

[6] Arnulfi, G. L., Giannattasio, P., Micheli, D., and Pinamonti, P. An innovative device for passive control of surge in industrial compression systems. *Journal of turbomachinery 123*, 3 (2001), 473–482.

[7] Astrom, K. J., and Hagglund, T. *Advanced PID Control.* ISA, Research Triangle Park, NC, 2006.

[8] Bagley, R. L., and Calico, R. Fractional order state equations for the control of viscoelasticallydamped structures. *Journal of Guidance, Control, and Dynamics 14*, 2 (1991), 304–311.

[9] Bagley, R. L., and Torvik, P. A theoretical basis for the application of fractional calculus to viscoelasticity. *Journal of Rheology 27*, 3 (1983), 201–210.

[10] Bingul, Z., and Karahan, O. Tuning of fractional pid controllers using pso algorithm for robot trajectory control. In *Mechatronics (ICM), 2011 IEEE International Conference on* (2011), IEEE, pp. 955–960.

[11] Biswas, A., Das, S., Abraham, A., and Dasgupta, S. Design of fractional-order pid controllers with an improved differential evolution. *Engineering applications of artificial intelligence 22*, 2 (2009), 343–350.

[12] Blanchini, F., Giannattasio, P., Micheli, D., and Pinamonti, P. Experimental evaluation of a high-gain control for compressor surge suppression. *Journal of turbomachinery 124*, 1 (2002), 27–35.

[13] Bode, H. W. *Network analysis and feedback amplifier design.* Van Nostrand, 1945.

[14] Calderón, A. J., Vinagre, B. M., and Feliu, V. Fractional order control strategies for power electronic buck converters. *Signal Processing 86*, 10 (2006), 2803–2819.

[15] Cao, J.-Y., and Cao, B.-G. Design of fractional order controllers based on particle swarm optimization. In *Industrial Electronics and Applications, 2006 1ST IEEE Conference on* (2006), IEEE, pp. 1–6.

[16] Cao, J.-Y., Liang, J., and Cao, B.-G. Optimization of fractional order pid controllers based on genetic algorithms. In *Machine Learning and Cybernetics, 2005. Proceedings of 2005 International Conference on* (2005), vol. 9, IEEE, pp. 5686–5689.

[17] Caponetto, R., Fortuna, L., and Porto, D. A new tuning strategy for a non integer order pid controller. In *First IFAC workshop on fractional differentiation and its application* (2004), pp. 168–173.

[18] Chang, F.-K., and Lee, C.-H. Design of fractional pid control via hybrid of electromagnetism-like and genetic algorithms. In *Intelligent Systems Design and Applications, 2008. ISDA'08. Eighth International Conference on* (2008), vol. 2, IEEE, pp. 525–530.

[19] Chang, L. Y., and Chen, H. C. Tuning of fractional pid controllers using adaptive genetic algorithm for active magnetic bearing system. *WSEAS Transactions on systems 8*, 1 (2009), 158–167.

[20] Chang, W.-D. Two-dimensional fractional-order digital differentiator design by using differential evolution algorithm. *Digital Signal Processing 19*, 4 (2009), 660–667.

[21] Charef, A. Analogue realisation of fractional-order integrator, differentiator and fractional pi λ d μ controller. *IEE Proceedings-Control Theory and Applications 153*, 6 (2006), 714–720.

[22] Chen, Y., and Vinagre, B. M. *Fractional-order systems and controls: fundamentals and applications.* Springer, 2010.

[23] Das, S. *Functional fractional calculus.* Springer, 2011.

[24] Diethelm, K., and Freed, A. D. *On the solution of nonlinear fractional-order differential equations used in the modeling of viscoplasticity.* Springer, 1999.

[25] Dolton, M. The use of limits in applying turbochargers to engines, 2006.

[26] Eberhart, R. C., and Kennedy, J. A new optimizer using particle swarm theory. In *Proceedings of the sixth international symposium on micro machine and human science* (1995), vol. 1, New York, NY, pp. 39–43.

[27] Engheia, N. On the role of fractional calculus in electromagnetic theory. *Antennas and Propagation Magazine, IEEE 39*, 4 (1997), 35–46.

[28] Engheta, N. On fractional calculus and fractional multipoles in electromagnetism. *Antennas and Propagation, IEEE Transactions on 44*, 4 (1996), 554–566.

[29] Ferreira, N. F., and Machado, J. T. Fractional-order hybrid control of robotic manipulators. In *Proceedings of the 11th International Conference on Advanced Robotics* (2003), vol. 398, Piscataway, Japan: IEEE Press.

[30] Fittro, R. L., and Knospe, C. R. μ control of a high speed spindle thrust magnetic bearing. In *Control Applications, 1999. Proceedings of the 1999 IEEE International Conference on* (1999), vol. 1, IEEE, pp. 570–575.

[31] Fleming, P. J., and Purshouse, R. C. Evolutionary algorithms in control systems engineering: a survey. *Control engineering practice 10*, 11 (2002), 1223–1241.

[32] Folland, G. B. *Advanced calculus.* Pearson Education India, 2002.

[33] Gabano, J.-D., and Poinot, T. Fractional modelling and identification of thermal systems. *Signal Processing 91*, 3 (2011), 531–541.

[34] Grega, W., and Pilat, A. Comparison of linear control methods for an amb system. *International Journal of Applied Mathematics and Computer Science 15*, 2 (2005), 245.

[35] Greitzer, E. M. Surge and rotating stall in axial flow compressorspart i: Theoretical compression system model. *Journal of Engineering for Gas Turbines and Power 98*, 2 (1976), 190–198.

[36] Hu, Y., and Øksendal, B. Fractional white noise calculus and applications to finance. *Infinite Dimensional Analysis, Quantum Probability and Related Topics 6*, 01 (2003), 1–32.

[37] Hypiusová, M., and Osuskỳ, J. Pid controller design for magnetic levitation model. In *International Conference February* (2010), vol. 10, p. 13.

[38] INTERNATIONAL ORGANIZATION FOR STANDARDIZATION ISO. *ISO14839-1: Mechanical vibration - Vibration of rotating machinery equipped with active magnetic bearings - Part 1: Vocabulary*, 2002.

[39] INTERNATIONAL ORGANIZATION FOR STANDARDIZATION ISO. *ISO14839-2: Mechanical vibration - Vibration of rotating machinery equipped with active magnetic bearings - Part 2: Evaluation of Vibration*, 2004.

[40] INTERNATIONAL ORGANIZATION FOR STANDARDIZATION ISO. *ISO14839-3: Mechanical vibration - Vibration of rotating machinery equipped with active magnetic bearings - Part 3: Evaluation of stability margin*, 2006.

[41] JASTRZEBSKI, R. P., HYNYNEN, K. M., AND SMIRNOV, A. H control of active magnetic suspension. *Mechanical Systems and Signal Processing 24*, 4 (2010), 995–1006.

[42] KHANDANI, K., AND JALALI, A. A. Pso based optimal fractional pid controller design for an active magnetic bearing system. In *18th Annual International Conference of Mechanical Engineering* (2010).

[43] KIRK, R. Evaluation of amb turbomachinery auxiliary bearings. *Journal of vibration and acoustics 121*, 2 (1999), 156–161.

[44] KNOSPE, C. R., AND ZHU, L. Performance limitations of non-laminated magnetic suspension systems. *Control Systems Technology, IEEE Transactions on 19*, 2 (2011), 327–336.

[45] LURIE, B. Tunable tid controller. *US patent 5*, 371 (1994), 670.

[46] MAIONE, G., AND LINO, P. New tuning rules for fractional piα controllers. *Nonlinear Dynamics 49*, 1-2 (2007), 251–257.

[47] MATIGNON, D. Stability properties for generalized fractional differential systems. In *ESAIM: proceedings* (1998), vol. 5, EDP Sciences, pp. 145–158.

[48] MCMILLAN, G. *Centrifugal and Axial Compressor Control*. Momentum Press, 2010.

[49] MONJE, C. A., VINAGRE, B. M., FELIU, V., AND CHEN, Y. Tuning and auto-tuning of fractional order controllers for industry applications. *Control Engineering Practice 16*, 7 (2008), 798–812.

[50] OLDHAM, K. B. Fractional differential equations in electrochemistry. *Advances in Engineering Software 41*, 1 (2010), 9–12.

[51] OLDHAM, K. B., AND SPANIER, J. *The fractional calculus: theory and applications of differentiation and integration to arbitrary order*, vol. 111. Academic press New York, 1974.

[52] Oustaloup, A. *La commande CRONE: commande robuste d'ordre non entier*. Hermes, 1991.

[53] Oustaloup, A., Levron, F., Mathieu, B., and Nanot, F. M. Frequency-band complex noninteger differentiator: characterization and synthesis. *Circuits and Systems I: Fundamental Theory and Applications, IEEE Transactions on 47*, 1 (2000), 25–39.

[54] Oustaloup, A., Mathieu, B., and Lanusse, P. The crone control of resonant plants: application to a flexible transmission. *European Journal of Control 1*, 2 (1995), 113–121.

[55] Oustaloup, A., Melchior, P., Lanusse, P., Cois, O., and Dancla, F. The crone toolbox for matlab. In *Computer-Aided Control System Design, 2000. CACSD 2000. IEEE International Symposium on* (2000), IEEE, pp. 190–195.

[56] Pan, I., and Das, S. *Intelligent fractional order systems and control: an introduction*. Springer Publishing Company, Incorporated, 2012.

[57] Podlubny, I. *Fractional differential equations: an introduction to fractional derivatives, fractional differential equations, to methods of their solution and some of their applications*, vol. 198. Academic press, 1998.

[58] Podlubny, I., Petraš, I., Vinagre, B. M., O'leary, P., and Dorčák, L. Analogue realizations of fractional-order controllers. *Nonlinear dynamics 29*, 1-4 (2002), 281–296.

[59] Price, K., Storn, R. M., and Lampinen, J. A. *Differential evolution: a practical approach to global optimization*. Springer Science & Business Media, 2006.

[60] Ross, B. *Fractional calculus and its applications*. Springer Berlin, 1975.

[61] Sanadgol, D. *Active control of surge in centrifugal compressors using magnetic thrust bearing actuation*. PhD thesis, University of Virginia, May 2006.

[62] Scalas, E., Gorenflo, R., and Mainardi, F. Fractional calculus and continuous-time finance. *Physica A: Statistical Mechanics and its Applications 284*, 1 (2000), 376–384.

[63] Schweitzer, G., and Maslen., E. H. *Magnetic Bearings*. Springer-Verlag, 2009.

[64] Senoo, Y., and Ishida, M. Deterioration of compressor performance due to tip clearance of centrifugal impellers. *Journal of Turbomachinery 109*, 1 (1987), 55–61.

[65] Storn, R., and Price, K. *Differential evolution-a simple and efficient adaptive scheme for global optimization over continuous spaces*, vol. 3. ICSI Berkeley, 1995.

[66] Tepljakov, A., Petlenkov, E., and Belikov, J. Fomcon: a matlab toolbox for fractional-order system identification and control. *International Journal of Microelectronics and Computer Science 2*, 2 (2011), 51–62.

[67] Valério, D., and da Costa, J. S. Ninteger: a non-integer control toolbox for matlab. In *1st IFAC Workshop on Fractional Differentiation and its Applications, Bordeaux, France* (2004).

[68] Valerio, D., and da Costa, J. S. A review of tuning methods for fractional pids. In *4th IFAC Workshop on Fractional Differentiation and Its Applications, FDA* (2010), vol. 10.

[69] Valerio, D., and Da Costa, J. S. *An introduction to fractional control*, vol. 91. IET, 2013.

[70] Vinagre, B. M., Monje, C. A., Calderón, A. J., and Suárez, J. I. Fractional pid controllers for industry application. a brief introduction. *Journal of Vibration and Control 13*, 9-10 (2007), 1419–1429.

[71] Xue, D., and Chen, Y. Suboptimum h2 pseudo-rational approximations to fractional-order linear time invariant systems. In *Advances in Fractional Calculus*. Springer, 2007, pp. 61–75.

[72] Xue, D., Zhao, C., and Chen, Y. Q. A modified approximation method of fractional order system. In *Mechatronics and Automation, Proceedings of the 2006 IEEE International Conference on* (2006), IEEE, pp. 1043–1048.

[73] Yoon, S. Y., Lin, Z., and Allaire, P. *Control of Surge in Centrifugal Compressors by Active Magnetic Bearings*. Springer, 2012.

[74] Yoon, S. Y., Lin, Z., Dimond, T., and Allaire, P. E. Control of active magnetic bearing systems on non-static foundations. In *Control and Automation (ICCA), 2011 9th IEEE International Conference on* (2011), IEEE, pp. 556–561.

[75] Zhao, C., Xue, D., and Chen, Y. Q. A fractional order pid tuning algorithm for a class of fractional order plants. In *Mechatronics and Automation, 2005 IEEE International Conference* (2005), vol. 1, IEEE, pp. 216–221.

[76] Zhu, L., Knospe, C. R., and Maslen, E. H. Analytic model for a nonlaminated cylindrical magnetic actuator including eddy currents. *Magnetics, IEEE Transactions on 41*, 4 (2005), 1248–1258.